

¹ Study of the multi-strange resonance $\Xi(1530)^0$ production
² with ALICE at the LHC energies

³ Jihye Song

4 Contents

5	List of Figures	4
6	List of Tables	8
7	1 The physics of relativistic heavy-ion collisions	9
8	1.1 Standard model	9
9	1.2 QCD and Quark-Gluon plasma	10
10	1.3 Heavy Ion Collisions	16
11	2 Theoretical models	19
12	2.1 Statistical-Thermal model	19
13	2.1.1 Calculations	21
14	2.1.2 Results and comparison with data	23
15	2.2 EPOS, UrQMD	25
16	3 Production of hyperon resonance	27
17	3.1 Strange quark and hyperons	29
18	3.2 Resonance production	31
19	4 A Large Ion Collider Experiment at the LHC	33
20	4.1 The Large Hadron Collider	33
21	4.2 The ALICE project	36
22	4.2.1 ALICE detector	36
23	4.2.2 Data Acquisition (DAQ) and trigger system	46
24	4.2.3 ALICE offline software frame work	48
25	5 Measurement of $\Xi(1530)^0$ production in p-Pb and Pb-Pb	50
26	5.1 $\Xi(1530)^0$ -reconstruction	50
27	5.1.1 Data sample and event selection	50
28	5.1.2 Track and topological selection	54
29	5.1.3 Particle identification	57
30	5.1.4 Signal extraction	60
31	5.2 Efficiency correction	69
32	5.3 Corrected p_T -spectra	72
33	5.4 Systematic uncertainties	74
34	5.5 $\Xi(1530)^0$ transverse momentum spectra	79
35	6 Further results and discussion	82
36	6.1 Mean transverse momentum	82
37	6.2 Particle yield ratios	86

38	6.2.1 Integrated yield ratios of excited to ground-state hadrons	86
39	6.3 Integrated yield ratios to pion	89
40	References	93

41 **List of Figures**

42 1	QCD coupling constant as a function of momentum transfer. Experimental 43 data and also theoretical prediction are presented. [1]	13
44 2	Phase diagram of partonic and hadronic matter. The chemical freeze out 45 points are determined from thermal models fit to heavy ion data at SIS, AGS, 46 and SPS energies. (http://na49info.web.cern.ch/na49info/Public/Press/findings.html)	15
47 3	The time evolution of a high energy heavy ion collision. [2]	16
48 4	Hydrodynamic evolution of a heavy ion collision with and without the for- 49 mation of a QGP.	18
50 5	Grand canonical thermal fit of 0-10% central Pb-Pb collisions, with 3 models (THERMUS, GSI, SHARE).	19
52 6	Ratio of baryonic and mesonic resonances over their stable partner as a 53 function of temperature.	24
54 7	Ratio of resonances over their stable partner as a function of $\sqrt(s)$	25
55 8	The $J^P = 1/2^+$ ground state baryon octet	28
56 9	The $J^P = 3/2^+$ baryon decuplet	28
57 10	Integrated yield relative to small system (pp or p-Be) as a function of the 58 mean number of participants $\langle N_{part} \rangle$ in the rapidity range $ y < 0.5$. The 59 results from ALICE are presented as full symbols, RHIC and SPS data 60 are shown as open symbols. Boxes on the dashed line at unity represent 61 statistical and systematic uncertainties on the pp or p-Be reference.	30
62 11	Hadronic phase	31
63 12	The CERN accelerator complex [3]	34
64 13	The ALICE detector	38
65 14	Schematic view of the ITS [4]	39
66 15	Track impact parameter resolution in the transverse plane ($r\phi$) vs p_T for 67 charged particle	40
68 16	Schematic view of the TPC	41
69 17	Specific energy loss (dE/dx) in the TPC vs. particle momentum in Pb-Pb 70 collisions at $\sqrt{s_{NN}} = 2.76$ TeV. The lines show the parametrisations of the 71 expected mean energy loss.	42
72 18	Correlation between the sum and difference of signal times in V0A and V0C. 73 Three classes of events collisions at (8.3 ns, 14.3 ns), background from Beam 74 1 at (-14.3 ns, -8.3 ns), and background from Beam 2 at (14.3 ns, 8.3 ns) 75 can be clearly distinguished.	43
76 19	Distribution of the V0 amplitude (sum of V0A and V0C in top, V0A in 77 bottom). The inset shows a magnified version of the most peripheral region.	45
78 20	The overall architecture of the ALICE DAQ and the interface to the HLT 79 system.	46
80 21	Schematic view of the AliRoot framework	49

81	22	Vertex-z coordinate distribution of the accepted events in p–Pb collision(Left) and in Pb–Pb collisions(Right). The red dashed line indicates vertex cut	52
82	23	Multiplicity distribution of accepted events in p–Pb collision in percentile. The each color and labels define the four intervals in which the analysis is performed.	52
83	24	Centrality distribution of three different trigger classes.	53
84	25	Sketch of the decay modes for Ξ^{*0} and depiction of the track and topological selection criteria.	55
85	26	TPC dE/dx as function of transverse momentum for total (top) and selected first emitted π in 3σ (bottom)	57
86	27	TPC dE/dx as function of transverse momentum for total (top) and selected second emitted π in 3σ (bottom)	57
87	28	TPC dE/dx as function of transverse momentum for total (top) and selected last emitted π in 3σ (bottom)	58
88	29	TPC dE/dx as function of transverse momentum for total (top) and selected proton in 3σ (bottom)	58
89	30	TPC dE/dx as function of transverse momentum for total (top) and selected first emitted π in 3σ (bottom)	58
90	31	TPC dE/dx as function of transverse momentum for total (top) and selected second emitted π in 3σ (bottom)	59
91	32	TPC dE/dx as function of transverse momentum for total (top) and selected last emitted π in 3σ (bottom)	59
92	33	TPC dE/dx as function of transverse momentum for total (top) and selected proton in 3σ (bottom)	60
93	34	The $\Xi^{\mp}\pi^{\pm}$ invariant mass distribution (Same-event pairs) in $1.8 < p_T < 2.2 \text{ GeV}/c$ and for the multiplicity class 20-40%. The background shape, using pairs from different events (Mixed-event background), is normalised to the counts in $1.49 < M_{\Xi\pi} < 1.51 \text{ GeV}/c^2$ and $1.56 < M_{\Xi\pi} < 1.58 \text{ GeV}/c^2$	61
94	35	The $\Xi^{\mp}\pi^{\pm}$ invariant mass distribution (Same-event pairs) in $3.0 < p_T < 3.5 \text{ GeV}/c$ and for the centrality class 0-10%. The background shape, using pairs from different events (Mixed-event background), is normalised to the counts in $1.49 < M_{\Xi\pi} < 1.51 \text{ GeV}/c^2$ and $1.56 < M_{\Xi\pi} < 1.58 \text{ GeV}/c^2$	62
95	36	The invariant mass distribution after subtraction of the mixed-event background in p–Pb collisions. The solid curve represents the combined fit, while the dashed line describes the residual background.	63
96	37	The invariant mass distribution after subtraction of the mixed-event background in Pb–Pb collisions. The solid curve represents the combined fit, while the dashed line describes the residual background.	64
97	38	σ fit parameters as a function of p_T in MB in p–Pb collisions (top) and in Pb–Pb collisions (bottom).	66

121	39	$\Xi(1530)^0$ -mass obtained from fit of the Voigtian peak as a function of p_{T} in each multiplicity classes in p–Pb collisions (top) and the different centrality classes in Pb–Pb (bottom).	67
122	40	$\Xi(1530)^0$ -raw spectra obtained from fit of the Voigtian peak and a polynomial residual background for different multiplicities in p–Pb collisions (top) and Pb–Pb collisions (bottom). Only the statistical error is reported.	68
123	41	$\Xi(1530)^0$ -raw spectra obtained from fit of the Voigtian peak and a polynomial residual background for different multiplicities. Only the statistical error is reported.	69
124	42	Real corrected $\Xi(1530)^0$ spectrum (black) for the minimum bias with Levy fit (black curve). Also shown are the unweighted generated (blue) and reconstructed (red) $\Xi(1530)^0$ spectra.	70
125	43	Efficiency as a function of p_{T} in minimum bias events in p–Pb collisions.	71
126	44	Efficiency as a function of p_{T} in different centrality classes in Pb–Pb collisions	72
127	45	Corrected p_{T} -spectra of $\Xi(1530)^0$ in NSD and different multiplicity classes in p–Pb collisions.	73
128	46	Corrected p_{T} -spectra of $\Xi(1530)^0$ in different centrality classes in Pb–Pb collisions.	73
129	47	Summary of the contributions to the systematic uncertainty in minimum bias events in p–Pb collisions. The dashed black line is the sum in quadrature of all the contributions.	77
130	48	Systematic uncertainties for each multiplicity classes in p–Pb collisions.	77
131	49	Summary of the contributions to the systematic uncertainty in minimum bias events in Pb–Pb collisions. The dashed black line is the sum in quadrature of all the contributions.	78
132	50	Systematic uncertainties for each multiplicity classes.	78
133	51	Corrected yields as function of p_{T} in NSD events and multiplicity dependent event classes in p–Pb collision system. Statistical uncertainties are presented as bar and systematical uncertainties are plotted as boxes.	80
134	52	Corrected yields as function of p_{T} in different centrality classes in Pb–Pb collision system. Statistical uncertainties are presented as bar and systematical uncertainties are plotted as boxes.	81
135	53	Mean transverse momenta $\langle p_{\text{T}} \rangle$ of Λ , Ξ^- , $\Sigma^{*\pm}$, Ξ^{*0} and Ω^- in p–Pb collisions at $\sqrt{s_{\text{NN}}} = 5.02$ TeV as a function of mean charged-particle multiplicity density $\langle dN_{\text{ch}}/d\eta_{\text{lab}} \rangle$, measured in the pseudorapidity range $ \eta_{\text{lab}} < 0.5$. The results for Λ , Ξ^- and Ω^- are taken from [5, 6, 7]. Statistical and systematic uncertainties are represented as bars and boxes, respectively. The Ω^- and Ξ^- points in the 3rd and 4th lowest multiplicity bins are slightly displaced along the abscissa to avoid superposition with the $\Xi(1530)^0$ points.	83

160	54	Mass dependence of the mean transverse momenta of identified particles for the 0 – 20% V0A multiplicity class and with $-0.5 < y_{\text{CMS}} < 0$ in p– Pb collisions at $\sqrt{s_{\text{NN}}} = 5.02$ TeV [5, 7], and in minimum-bias pp collisions at $\sqrt{s} = 7$ TeV [8] with $ y_{\text{CMS}} < 0.5$. Additionally, D^0 and J/ψ results are plotted. The D^0 and J/ψ were measured in different rapidity ranges: $ y_{\text{CMS}} < 0.5$ [9] ($ y_{\text{CMS}} < 0.9$ [10]) for D^0 (J/ψ) in pp and $-0.96 < y_{\text{CMS}} <$ 0.04 [9] ($-1.37 < y_{\text{CMS}} < 0.43$ [11]) for D^0 (J/ψ) in p–Pb. Note also that the results for D^0 and J/ψ in p–Pb collisions are for the 0–100% multiplicity class.	84
161			
162	55	Ratio of $\Xi(1530)^0$ to Ξ^- measured in pp [8], p–Pb [5, 7] and Pb–Pb collisions as a function of $\langle dN_{\text{ch}}/d\eta_{\text{lab}} \rangle$ measured at midrapidity. Statistical uncer- tainties (bars) are shown as well as total systematic uncertainties (hollow boxes) and systematic uncertainties uncorrelated across multiplicity (shaded boxes). A few model predictions are also shown as lines at their appropriate abscissa.	87
163			
164	56	Ratio of $\rho/\pi(\text{Up})$, K^*/K , $\phi/K(\text{Left bottom})$ and Λ^*/Λ with system size measured at mid-rapidity. Statistical uncertainties (bars) are shown as well as total systematic uncertainties (hollow boxes) and systematic uncertainties uncorrelated across multiplicity (shaded boxes). A few model predictions are also shown as lines at their appropriate abscissa.	88
165			
166	57	Ratio of $\Xi(1530)^0$ to π^\pm , measured in pp [12] and p–Pb [8] collisions, as a function of the average charged particle density ($\langle dN_{\text{ch}}/d\eta_{\text{lab}} \rangle$) measured at mid-rapidity. Statistical uncertainties (bars) are shown as well as total systematic uncertainties (hollow boxes) and systematic uncertainties uncor- related across multiplicity (shaded boxes). A few model predictions are also shown as lines at their appropriate abscissa.	90
167			
168	58	Particle yield ratios to pions of strange and multi-strange hadrons normal- ized to the values measured in pp collisions, both in pp and in p–Pb colli- sions. The common systematic uncertainties cancel in the double-ratio. The empty boxes represent the remaining uncorrelated uncertainties. The lines represent a simultaneous fit of the results with the empirical scaling formula in Equation ???.	91
169			
170	59	p_{T} -integrated yield ratios of strange and multi-strange hadrons to $(\pi^+ + \pi^-)$ as a function of $\langle dN_{\text{ch}}/d\eta_{\text{lab}} \rangle$ measured in the rapidity interval $ \eta < 0.5$. The empty and dark-shaded boxes show the total systematic uncertainty and the contribution uncorrelated across multiplicity bins, respectively. The values are compared to calculations from MC models and to results obtained in Pb–Pb and p–Pb collisions at the LHC.	92
171			
172			
173			
174			
175			
176			
177			
178			
179			
180			
181			
182			
183			
184			
185			
186			
187			
188			
189			
190			
191			
192			
193			
194			
195			
196			
197			

¹⁹⁸ **List of Tables**

199	1	Constituents of matter in the Standard Model	9
200	2	Fundamental forces	10
201	3	Parameters used in the thermal-model calculations.	20
202	4	Properties of particles used in the ratio calculations.	22
203	5	Difference of mass (ΔM), baryon number (ΔB), strangeness (ΔS) and charge (ΔQ) of the ratios.	23
204	6	Quantum numbers and masses associated to the three lighter quarks: u, d and s	27
207	7	Lifetime of hadronic resonances	29
208	8	Number of accepted and analyzed events per multiplicity/centrality interval	54
209	9	Track selections common to all decay daughters and primary track selections applied to the charged pions from decays of Ξ^{*0}	54
211	10	Topological and track selection criteria.	55
212	11	Summary of the systematic uncertainties on the differential yield, $d^2N/(dp_T dy)$. Minimum and maximum values in all p_T intervals and multiplicity classes in p–Pb, centrality classes in Pb–Pb are shown for each source.	79

215 **1 The physics of relativistic heavy-ion collisions**

216 The main objective of relativistic heavy ion physics is to study the nuclear matter under
 217 extreme conditions which are high temperature and energy density. In these conditions,
 218 the Standard Model anticipates that the nuclear matter undergo a new phase, where the
 219 quarks and the gluons are expected to be de-confined called quark-gluon plasma (QGP)
 220 and to freely move.

221 **1.1 Standard model**

222 If one have question "what the world is made of", our current answer to the question is
 223 Standard Model (SM) families [13] reported in Table 1. The SM explains the way how
 224 those basic blocks of matter interact and how they are ruled by four fundamental forces.
 225 In this explanation, the matter consist of 12 particles, which have a spin of 1/2 (fermions)
 226 and can be categorized in accordance with way how they interact or equivalently to what
 227 charges they carry. The basic particles are six quarks (up, down, charm, strange, top and
 228 bottom) that carry fractional charge of $+\frac{2}{3}e$ or $-\frac{1}{3}e$, and six leptons (electron, electron
 229 neutrino, muon, muon neutrino, tau, tau neutrino) with integer charge.

Family	Quarks				Leptons		
	Name	Charge[e]	Mass		Name	Charge[e]	Mass
1	u	2/3	$2.2^{+0.6}_{-0.4}$ MeV/c ²		e^-	-e	0.511 MeV/c ²
	d	-1/3	$4.7^{+0.5}_{-0.4}$ MeV/c ²		ν_e	0	< 2 eV/c ²
2	c	2/3	$1.27^{+0.03}$ GeV/c ²		μ^-	-e	105.66 MeV/c ²
	s	-1/3	96^{+8}_{-4} MeV/c ²		ν_μ	-e	< 0.19 eV/c ²
3	t	2/3	173.21 ± 1.22 GeV/c ²		τ^-	-e	1.777 GeV/c ²
	b	-1/3	$4.18^{+0.04}_{-0.03}$ GeV/c ²		ν_τ	-e	< 18.2 MeV/c ²

Table 1: Constituents of matter in the Standard Model

230 The interactions between elementary particles are described by the exchange of gauge
 231 bosons(gluon, photon, Z-boson, W-boson), reported in Table 2 together with their relative
 232 coupling strengths. The leptons are governed the weak force and the electromagnetic force.
 233 Quarks have color property which is the character of charge in the strong force. The color
 234 could take one out of three possible values (conventionally red, green and blue). The color
 235 can not be appeared freely. After they are confined they come out in the form of hadron
 236 which are colorless. Further explaination on color is described in Section 1.2. Then, the
 237 hadrons are grouped into baryon and mesons. Baryons consist of three quarks, qqq or $(\bar{q}\bar{q}\bar{q})$
 238 while mesons consist of two quarks ($q\bar{q}$).

239 The models that describe these interactions are listed as follows:

240

Force	Strength	Gauge Boson(s)	Applies on
Strong force	1	8 Gluons(g)	Quarks, gluons
Electromagnetic force	$\simeq 10^{-2}$	Photon (γ)	All charged particles
Weak force	$\simeq 10^{-7}$	W^\pm, Z^0	Quarks, leptons
Gravitation	$\simeq 10^{-39}$	Gravitons	All particles

Table 2: Fundamental forces

241 **Quantum Electro-Dynamics (QED)** is a quantum field theory of the electromagnetic
 242 force and describes how light and matter interact. This is the first theory where
 243 full agreement between quantum mechanics and special relativity is achieved. It explains
 244 mathematically not only all interactions of light with matter but also those of charged
 245 particles with one another.

246 **Electroweak Theory (EW)** is the unified description of two of the four known fundamental
 247 interactions of nature: electromagnetism and the weak interaction. The first
 248 measurement of the existence of the weak bosons W^+ , W^- and Z^0 was performed in 1983,
 249 when they were produced and directly observed in $Spp\bar{S}$ collisions at CERN.

251 **Quantum Chromo-dynamics (QCD)** is the theory of the strong interaction (color
 252 force), describing the interactions between quarks and gluons which make up the hadrons.
 253 Starting from the classification of the large amount of particles discovered during the fifties,
 254 the original idea of the quark model by Gell-Mann (Nobel Prize in 1969) has been developed
 255 during the sixties until 1973, when David J. Gross, H. David Politzer and Frank Wilczek
 256 discovered the asymptotic freedom property of the strong nuclear interaction.

258 1.2 QCD and Quark-Gluon plasma

259 As the number of known particle species became large, the idea that these could be the
 260 elementary constituents of matter was replaced by the notion that these species could in
 261 fact be composite objects made up of fewer, more elementary particles, in a similar way to
 262 what had already happened to the elements of Mendeleev's Periodic Table. The original
 263 idea by Gell-Mann (1964) was that the hadrons could be obtained as combination of the
 264 fundamental representation of an $SU_f(3)$ group, where three different flavors of quark (q
 265 = u, d, s) combine to build mesons ($q\bar{q}$) and hadrons (qqq). However, when cataloging
 266 hadrons using the $SU_f(3)$ group, there are anomalous states, such as the $\Omega^-(sss)$ and the
 267 $\Delta^{++}(uuu)$, that are combinations of three quarks of the same flavor, in clear contrast
 268 with the Pauli exclusion principle for fermions. A solution was proposed in 1965 by Moo-
 269 Young Han with Yoichiro Nambu and Oscar W. Greenberg, who independently solved the
 270 problem by proposing that quarks possess an additional $SU(3)$ gauge quantum number,

271 later called color charge. This new quantum number may assume three states, represented
 272 by the three primary colors: red, green and blue (denoted symbolically by R, G and B,
 273 respectively). The introduction of this new quantum number also provides an explanation
 274 to other empirical evidence, such as the fact that no qq , $\bar{q}q$ or the single quark have never
 275 been observed directly. On the other hand, the existence of color charge gives rise to the
 276 possible existence of differently colored states for each particle. Thus, we could have many
 277 states for the proton, such as $u_R u_G d_B$, $u_R u_G d_G$, $u_B u_R d_R$, and so on. The fundamental
 278 rule that solves such contradictions is that all the particle states observed in nature are
 279 "colorless" or "white" (or, to be more precise, unchanged under $SU_c(3)$ rotations). The
 280 dynamics of the quarks and gluons are controlled by the gauge invariant QCD Lagrangian:

$$\mathcal{L}_{QCD} = \underbrace{i\delta_{ij}\bar{\Psi}_q^i\gamma^\mu\partial_\mu\Psi_q^j}_{\mathcal{L}_1} + \underbrace{g_s\bar{\Psi}_q^i\gamma^\mu t_{ij}^a A_\mu^a\Psi_q^j}_{\mathcal{L}_2} + \underbrace{m_q\bar{\Psi}_q^i\Psi_q^j}_{\mathcal{L}_3} + \underbrace{\frac{1}{4}F_{\mu\nu}^a F^{a\mu\nu}}_{\mathcal{L}_4} \quad (1)$$

281 where the coloured gluon field tensor, $F_{\mu\nu}^a$ (with color index a) and the squared gauge
 282 coupling parameter, g_s^2 (associated to the strong coupling constant α_s) are defined as:

$$F_{\mu\nu}^a = \partial_\mu A_\nu^a - \partial_\nu A_\mu^a + g_s f^{abc} A_\mu^b A_\nu^c \quad (2)$$

283 and

$$g_s^2 = 4\pi\alpha_s \quad (3)$$

284 where:

- 285 • Ψ_q^i : the quark field with flavor q and color index $i \in [1;3]$, such as $\Psi_q = (\Psi_{qR}, \Psi_{qG},$
 286 $\Psi_{qB})^T$ and A_μ^a is the gluon field with color index a (adjoint representation)
- 287 • γ^μ : Dirac matrices that express the vector nature of the strong interaction, with μ
 288 being the Lorentz vector associated index
- 289 • m_q : quark mass, a priori not equal to zero (resulting from the Higgs mechanism or
 290 equivalent)
- 291 • t_{ij}^a : generator matrices of the group $SU_c(3)$, proportional to the Gell-Mann matrices,
 292 that perform revolutions in color space, representing interaction of quarks and gluons
- 293 • f^{abc} : structure constant of QCD

294 Each of the four terms of the QCD Lagrangian expresses and aspect of the interaction,
 295 specifically:

- 296 • \mathcal{L}_1 : gives the kinetic energy of the quark field Ψ_q^i

297 • \mathcal{L}_2 : gives the interaction between quarks (fermions) and gluons (the bosons of the
298 interaction)

299 • \mathcal{L}_3 : gives the mass of the quarks

300 • \mathcal{L}_4 : gives the kinetic energy of the gluons

301 The terms of this equation, together with the fundamental parameters α_s and m_q ,
302 summarize in just one expression all the features of the strong interaction. The first three
303 terms describe the free propagation of quarks and gluons and the quark-gluon interaction.
304 The remaining two terms show the presence of three and four gluon vertices in QCD and
305 reflect the fact that gluons themselves carry color charge. This is a consequence of the non-
306 abelian⁴ character of the gauge group. This peculiarity of the QCD interaction imposes the
307 evolution of the strong coupling constant, α_s . The corresponding trend has been measured
308 experimentally, and compared in Figure 1 with predictions. A practical consequence of
309 this behavior is that the corresponding potential has a completely different shape than the
310 other fundamental interactions and can be expressed by the following equation:

$$V(r) = -4 \frac{\alpha_s}{3r} + kr \quad (4)$$

311 where r is the separation distance between the two quarks and k is a constant that is
312 approximately 1 GeV/fm.

313 Three are main properties of the QCD interaction:

314

315 **Confinement** At large distances between quarks and gluons (i.e. small values of trans-
316 ferred momentum Q in Figure 1) the coupling constant is large and the associated force
317 is strong enough to keep these elementary con- stituents (usually called partons) confined
318 in bounded states. As expressed in the Equation 4, the attractive potential increases with
319 the increasing of the relative distance between the two partons preventing the separation
320 of an individual quark or gluon. This explains the meaning of the term "confinement"
321 adopted to describe this energy regime. From the theoretical point of view, the large value
322 of α_s make impossible any perturbative approach in the solution of the Hamilton equation
323 of the system. A successful solution is to perform the study of the system on a discrete
324 space. Such techniques are known as lattice QCD and are based on numerical Monte Carlo
325 simulations. The challenge for the calculations is to reduce the lattice spacing in order to
326 approach the continuum.

327

328 **Asymptotic freedom** Reducing the distance between quarks and gluons (i.e. increas-
329 ing Q in Figure 1) the coupling constant α_s becomes smaller. As anticipated, this is a
330 unique feature among the forces and comes from the non-abelian nature of the QCD gauge
331 symmetry. Such a phenomenon is also depicted by the weakening of the anti-screening
332 effect of the surround- ing virtual gluons with decreasing distance. In this way two quarks

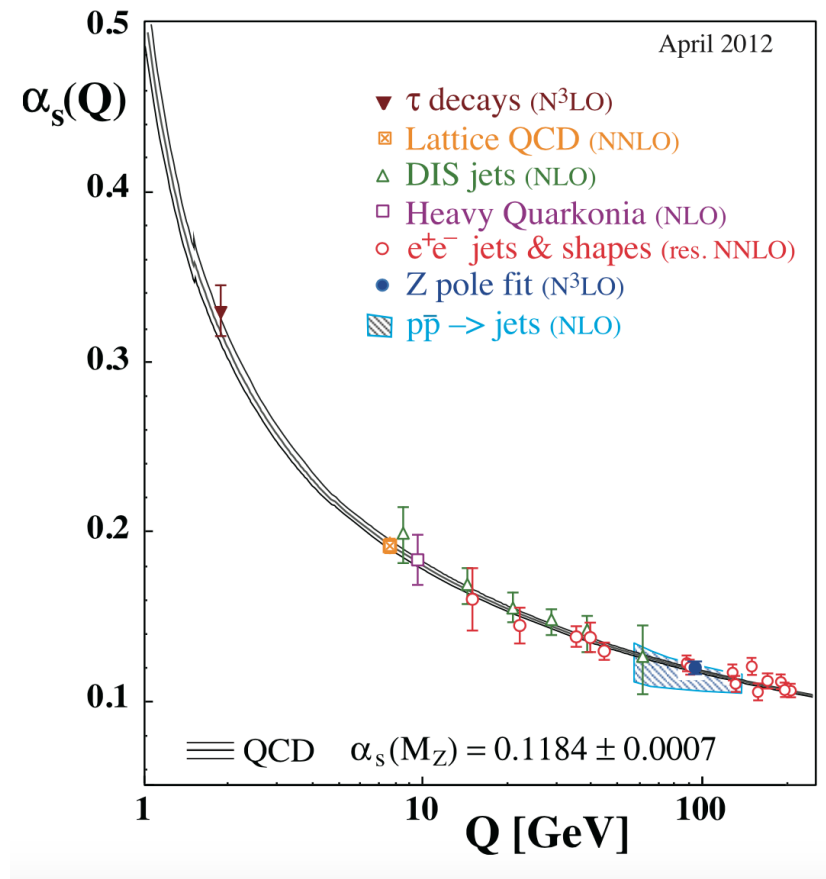


Figure 1: QCD coupling constant as a function of momentum transfer. Experimental data and also theoretical prediction are presented. [1]

333 closer and closer in space show each other a smaller and smaller color charge.

334

335 **Chiral symmetry** One further property of interest is connected to the chirality of
336 the quark. It can be verified that the QCD lagrangian for massless quarks is invariant
337 under a chiral rotation ($SU_L(N_f) \times SU_R(N_f)$), while the operator $\bar{q}q = \bar{q}_L q_R + \bar{q}_R q_L$ is
338 not invariant (in the axial part), meaning that the mesons (state $\bar{q}q$) should have the same
339 mass. Experimentally this is clearly not true, and it could be shown that the axial current
340 is conserved (PCAC and the Goldberger-Treiman relation). The solution to this puzzle
341 is that the chiral (axial-vector) symmetry is spontaneously broken; this means that the
342 symmetry of the Hamiltonian is not a symmetry of the corresponding ground state. It
343 has also been shown, by G. t'Hooft, that the confinement implies a dynamical breaking
344 of the chiral symmetry. This means that the breaking comes from the interaction between
345 the objects in the system. From this follows that the masses of the quarks are strongly
346 increased because of the interaction with the constituents of the system. This mechanism,
347 known as dynamical chiral symmetry breaking justifies the mass of the hadrons, reducing
348 the role of the Higgs mechanism in the mass explanation at least for the light hadrons.

349 The asymptotic freedom property suggests the existence of a state of matter, called
350 Quark-Gluon Plasma (QGP), in which the constituents of the hadrons are de-confined.
351 The hatched region in Figure 2 presents the expected phase boundary between partonic
352 and hadronic matter from lattice QCD calculations.

353 Two relevant thermodynamical observables of the system are plotted in the figure. One
354 is temperature T and another one is the baryonic chemical potential μ_B . The red points
355 have been measured from thermal models fit on data from different experiment [14] and
356 lie along a line that represent the limit between the two phases. As one can see in Figure
357 2, there are different ways to achieve the transition. It can be performed by changing the
358 temperature and/or the net baryonic density (μ_B).

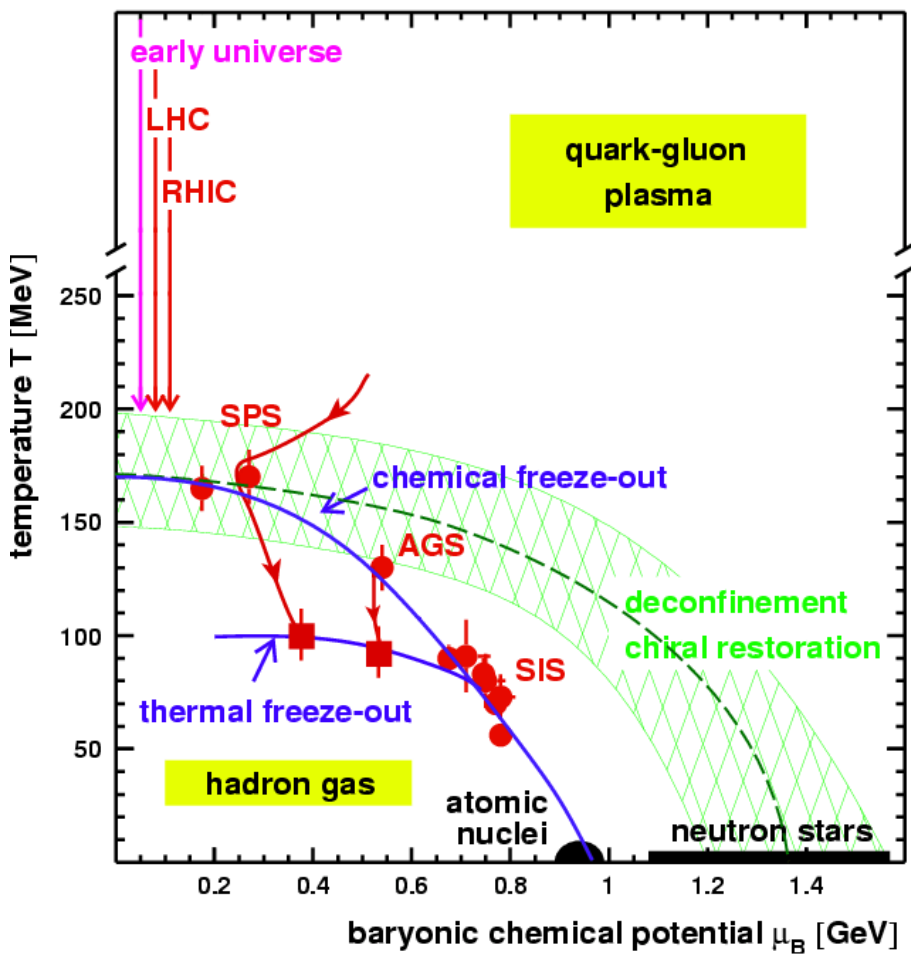


Figure 2: Phase diagram of partonic and hadronic matter. The chemical freeze out points are determined from thermal models fit to heavy ion data at SIS, AGS, and SPS energies. (<http://na49info.web.cern.ch/na49info/Public/Press/findings.html>)

359 **1.3 Heavy Ion Collisions**

360 Knowledge of the space-time evolution of the system created in high energy heavy ion
 361 collisions help to understand the dynamics of nuclear matter under extreme conditions.
 362 The Figure 3 presents the schematic of the time evolution in case of collision of two Lorentz
 363 contracted nuclei at very high energy. After the colliding, a large amount of energy can be
 364 deposited in a small area of space and in a short duration of time. The matter produced
 365 might have very high energy density and temperature so that it is sufficiently able to reach
 366 to QGP that is baryon free region.

367 Just after the colliding, the medium may not be in thermal equilibrium which can be
 368 reached after that the evolution is governed by the law of thermodynamics. As the system
 369 expands and cools, the hadronization takes place and the freeze out comes after some
 370 time. Different stages during the collisions can be studied by various observables, such as,
 371 Electromagnetic probes, Quarkonia and heavy flavour, Hard probes, Electroweak probes,
 372 global properties and Freeze-out condition as well. Most of the produced particles in the
 373 high energy heavy-ion collisions are emitted at freeze-out. In order to estimate the energy
 374 density, pressure, temperature and baryon chemical potential, the study of particle after
 375 freeze-out gives crucial information. Those quantities could be derived from measurement
 376 of multiplicity and rapidity distribution, transverse momentum (p_T) distributions.

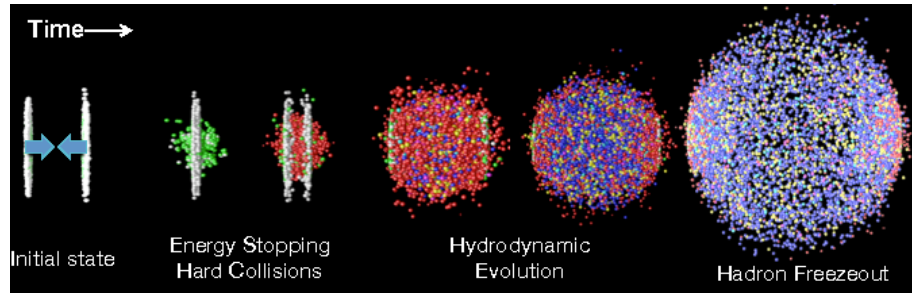


Figure 3: The time evolution of a high energy heavy ion collision. [2]

377 In the case a QGP is formed, it will eventually expand because of its internal pressure.
 378 As the system expands it also cools. The space-time evolution of the expansion can be
 379 seen in Figure 4 (right side). A and B represent the two incoming ion beams. After a pre-
 380 equilibrium phase a QGP is formed. As it expands, the system will eventually reach what
 381 is known as the critical temperature (T_c). At this point partons begin to hadronize and this
 382 will continue until the chemical freeze-out (T_{ch}) takes place, when inelastic collisions cease.
 383 At this stage the distribution of hadrons is frozen. As cooling and expansion continue the
 384 hadrons reach what is called thermal freeze out (T_{fo}). Here the elastic collisions stop and
 385 the hadrons carry fixed momenta. The QGP state can not be directly observed, because of
 386 its short lifetime. Instead, through experiment we measure the final state hadrons, which

387 have a fixed momentum after T_{fo} . The observables of interest should tell us about the
388 de-confinement and the thermodynamic properties of the matter. Moreover, experimental
389 measurements include yields and p_T spectra of various particle species, azimuthal studies
390 of high p_T particles, phase space distributions, and particle correlations.

391 A practical way to reach a critical condition in which a nuclear system should undergo
392 a phase transition to the QGP, at high temperature and/or matter density, is to collide
393 two nuclei at sufficiently high energy. Therefore, relativistic and ultra-relativistic heavy-ion
394 collisions are a unique tool to study nuclear matter under extreme conditions.

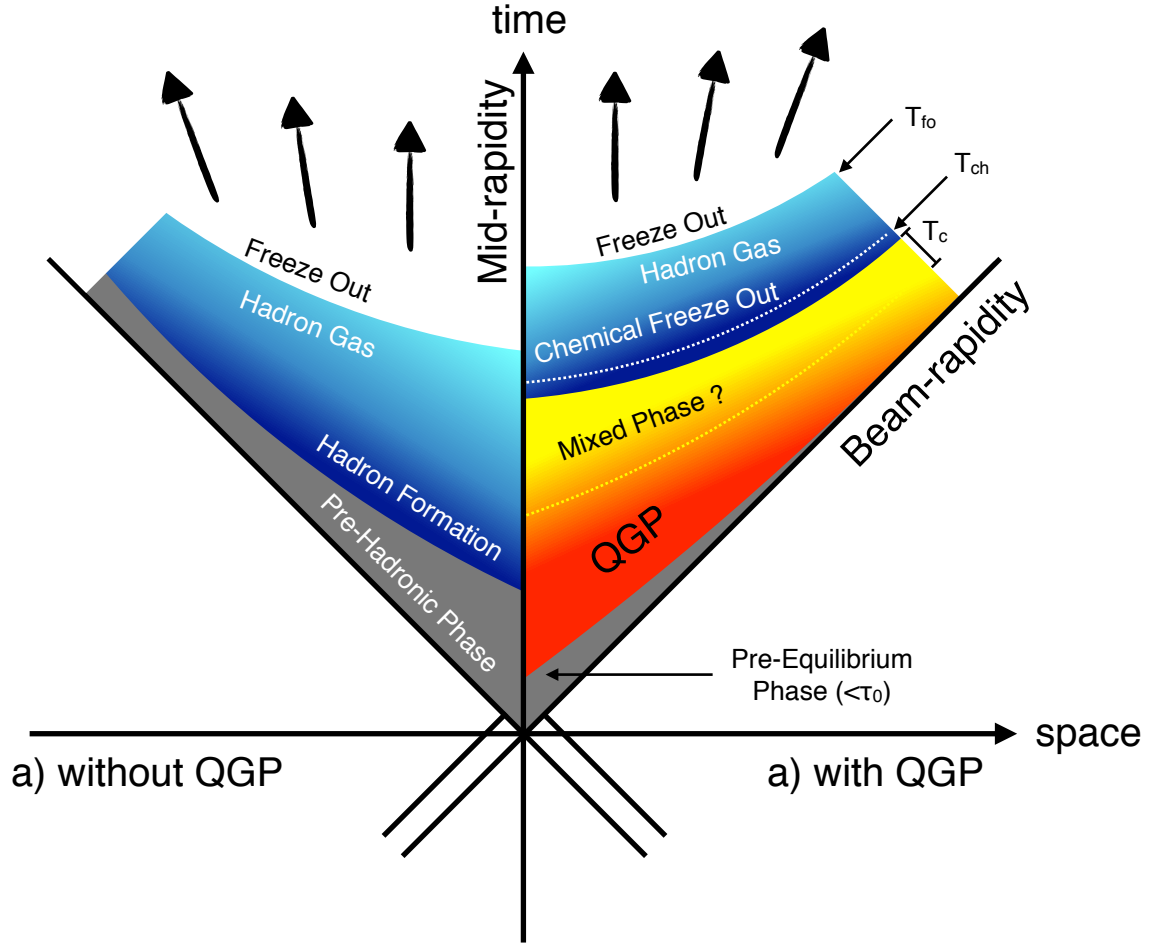


Figure 4: Hydrodynamic evolution of a heavy ion collision with and without the formation of a QGP.

395 2 Theoretical models

396 2.1 Statistical-Thermal model

397 The statistical-thermal model deal with the fireball created from high energy collisions as
 398 an ideal gas of hadrons including resonances. These hadrons are described by local thermal
 399 distributions at freeze-out with the parameters common to all particle species. The
 400 model has proved successful in applications to relativistic collisions of both heavy ions and
 401 elementary particles. The comparison between prediction and data obtained from Pb–Pb
 402 collisions are shown in Figure 5. In light of this success, THERMUS, a thermal model
 403 analysis package, has been developed for incorporation into the object-oriented ROOT
 404 framework [15].

405

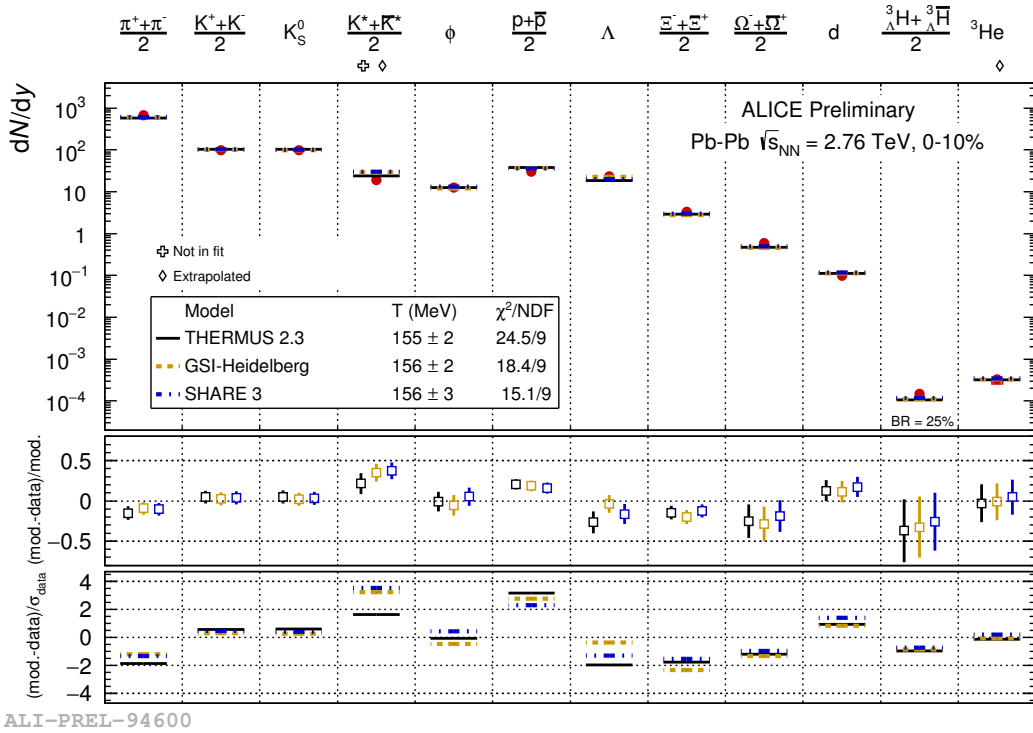


Figure 5: Grand canonical thermal fit of 0-10% central Pb-Pb collisions, with 3 models (THERMUS, GSI, SHARE).

406 There are three types of statistical-thermal models in explaining data in high energy
 407 nuclear physics and THERMUS treats the system quantum numbers B (baryon number),

408 S (strangeness) and Q (charge) within three distinct formalisms:

- 409 1. **Grand-Canonical Ensemble:** Because the hot dense matter produced in nucleus-
410 nucleus collisions is large enough, this ensemble is the most widely used in applica-
411 tions to heavy-ion collisions, in which the quantum numbers or particle numbers are
412 conserved on average through the temperature and chemical potential.
- 413 2. **Fully-Canonical Ensemble:** In which B, S and Q are exactly conserved and this
414 ensemble used in high-energy elementary collisions such as pp, p \bar{p} and e $^-$ e $^+$ collisions.
- 415 3. **Strangeness-Canonical Ensemble:** In heavy-ion collisions, the large numbers of
416 baryons and charged particles generally allows baryon number and charge to be
417 treated grand-canonically. However, in small systems or at low temperatures, a
418 canonical treatment leads to a suppression of hadrons carrying non-zero quantum
419 numbers, since these particles have to be created in pairs and the resulting low pro-
420 duction of strange particles needs a canonical treatment of strangeness. Within this
421 ensemble the strangeness in the system is fixed exactly by its initial value of S, while
422 the baryon and charge content are treated grand-canonically.

423 In order to calculate the thermal properties of a system, the partition function requires to
424 be evaluated. The form of it clearly depends on the choice of ensemble. In the present
425 analysis the strangeness-canonical ensemble used and statistical-thermal model requires six
426 parameters as input: the chemical freeze-out temperature T , baryon and charge chemical
427 potentials μ_B and μ_Q respectively, canonical or correlation radius, R_C ; the radius inside
428 which strangeness is exactly conserved and the fireball radius R . An additional strangeness
429 saturation factor γ_S has been used as indicator of a possible departure from equilibrium
430 and $\gamma_S = 1.0$ corresponds to complete strangeness equilibration.

431 The volume dependence cancels out when studying the particle ratios as well as strangeness
432 canonical equivalent to grand canonical formalism if $\Delta S = 0$ in the ratios and γ_S also can-
433 cels out. Parameters used in the analysis reported in Table 3.

Table 3: Parameters used in the thermal-model calculations.

Parameter	Value
T (MeV)	varied
μ_B (MeV)	0.1
μ_Q (MeV)	0.0
γ_S	1.0

434

435 **2.1.1 Calculations**

436 *Concept:*

437 In order to calculate the particle ratios within strangeness canonical formalism of THER-
438 MUS, temperature varied between 60 MeV to 180 MeV and particle yields extracted for
439 each temperature value and then primary particle ratios calculated for each case.

440

441 *Feed-Down Correction:*

442 Since the particle yields measured by the detectors in collision experiments include feed-
443 down from heavier hadrons and hadronic resonances, the primitive hadrons are allowed to
444 decay to particles considered stable by the experiment before model predictions are com-
445 compared with experimental data. In the analysis only Λ particles counted as stable (do not
446 allowed to decay) so there is no feed-down contribution from these particles to the other
447 ratios.

448

449 Properties of studied particles and their particle ratios listed in Table 4 and Table 5,
450 respectively.

451

452

Table 4: Properties of particles used in the ratio calculations.

Particle	Δ^{++}	Δ^{++}	p	K^{*0}	K^+	Λ^*	Λ	Σ^{*+}	Σ^+	Σ^0	Ξ^{*0}	Ξ^-
Mass (MeV/ c^2)	1232	938.27	895.92	493.67	1519.5	1115.68	1382.8	1189.37	1192.64	1531.80	1321.31	-
Width (MeV/ c^2)	120	-	50.7	-	15.6	-	37.6	-	-	9.1	-	-
$c\tau$ (fm)	1.6	-	3.9	-12.6	-	5.51	-	-	21.6	-	-	-
Ang. Momentum (J)	$3/2$	$1/2$	1	0	$3/2$	$1/2$	$3/2$	$1/2$	$1/2$	$3/2$	$1/2$	$1/2$
$^{22}_N$ Isospin (I)	$3/2$	$1/2$	$1/2$	$1/2$	0	0	1	1	1	$1/2$	$1/2$	$1/2$
Parity (P)	+1	+1	-1	0	-1	+1	+1	+1	+1	+1	+1	+1
Strangeness (S)	0	0	1	1	-1	-1	-1	-1	-1	-2	-2	-2
Baryon Number (B)	1	1	0	0	1	1	1	1	1	1	1	1
Decay Channel	$p\pi^+$	-	π^-	$\mu^+\nu_\mu$	pK^-	$p\pi^-$	$\Lambda\pi^+$	$p\pi^0$	$\Lambda\gamma$	$\Xi^-\pi^+$	$\Lambda\pi^-$	-
Branching Ratio (%)	~ 100	-	~ 66.7	~ 63.54	~ 45	~ 63.9	~ 87	~ 51.6	~ 100	~ 64	~ 99.9	-
Q-Value(MeV/ c^2)	154.16	-	262.68	-	87.55	37.84	127.55	111.53	76.96	70.92	70.66	-

Table 5: Difference of mass (ΔM), baryon number (ΔB), strangeness (ΔS) and charge (ΔQ) of the ratios.

Particle	Δ^{++}/p	K^*/K^+	Λ^*/Λ	Σ^{*+}/Λ	Σ^0/Λ	Σ^{*+}/Σ^+	Ξ^{*0}/Ξ^-
ΔM (MeV/ c^2)	293.8	402.25	403.82	267.12	76.96	193.43	210.49
ΔB	0	0	0	0	0	0	0
ΔS	0	0	0	0	0	0	0
ΔQ	+1	-1	0	+1	0	0	-1
Slope (%) per MeV	0.19	0.76	0.98	0.25	-0.08	0.37	0.42

453 **2.1.2 Results and comparison with data**

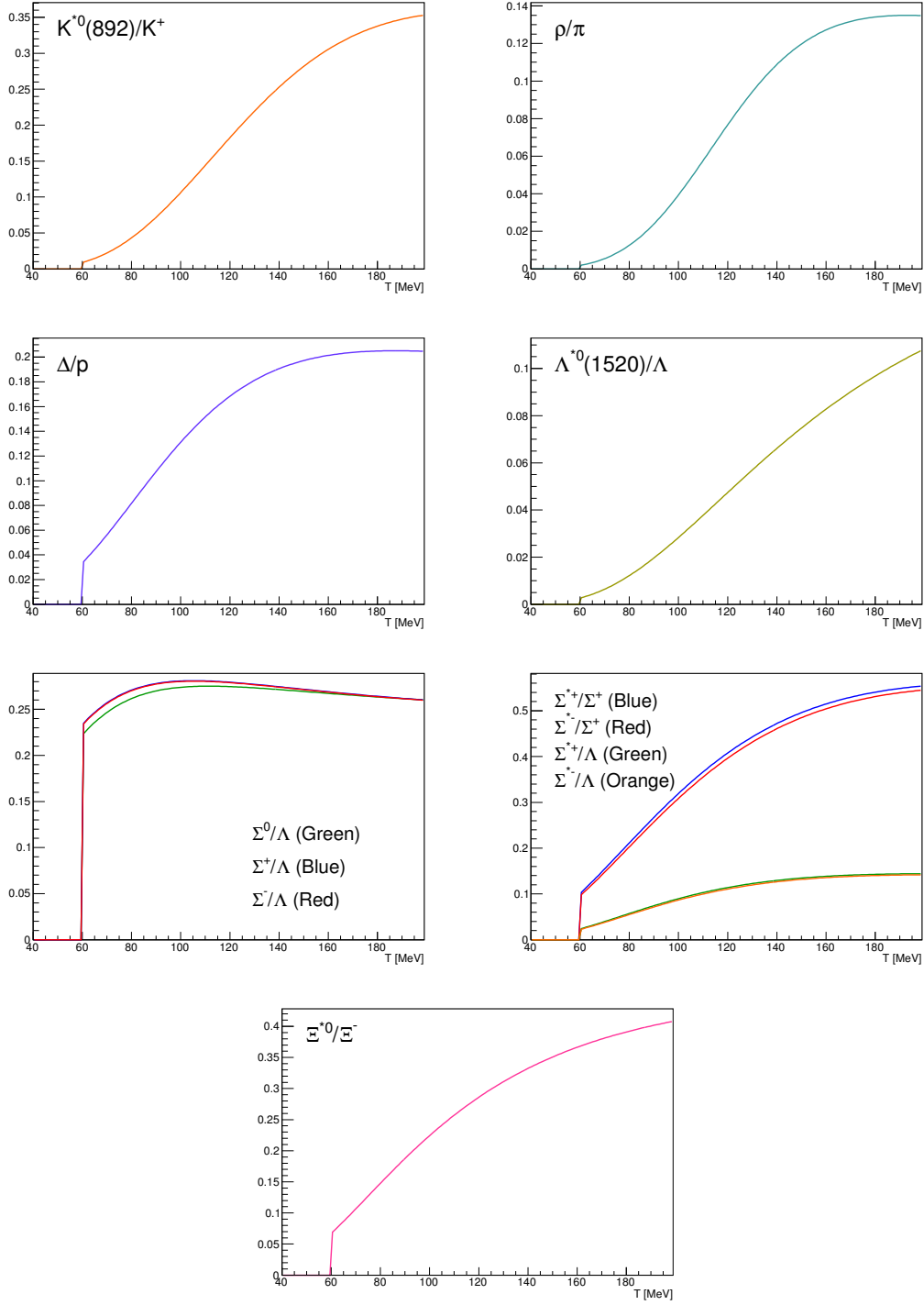


Figure 6: Ratio of baryonic and mesonic resonances over their stable partner as a function of temperature.

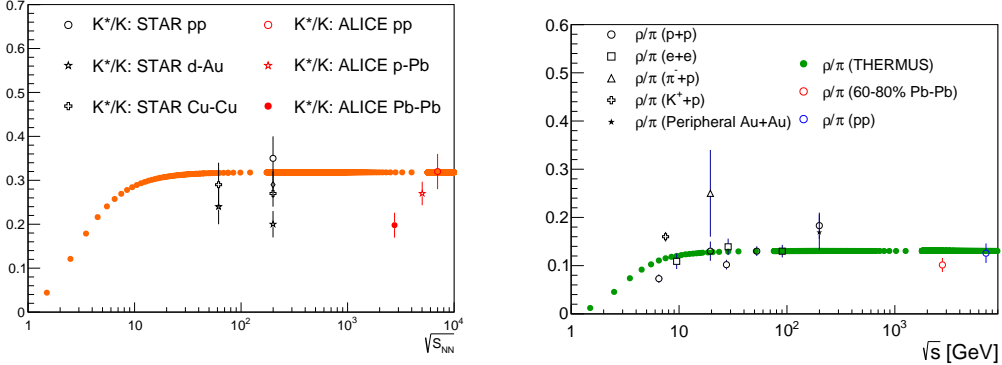


Figure 7: Ratio of resonances over their stable partner as a function of $\sqrt{(s)}$.

454 2.2 EPOS, UrQMD

455 The EPOS3 model [16, 17, 18] describes the full evolution of a heavy-ion collision. The
 456 initial stage is treated via a multiple-scattering approach based on Pomerons and strings.
 457 The reaction volume is divided into a core and a corona part [19]. The core is taken as
 458 the initial condition for the QGP evolution, for which one employ viscous hydrodynamics.
 459 The corona part is simply composed of hadrons from string decays. After hadronisation of
 460 the fluid (core part), these hadrons and as well the corona hadrons are fed into UrQMD
 461 [20, 21], which describes hadronic interactions in a microscopic approach. The chemical
 462 and kinetic freeze-outs occur within this phase. The chemical freeze-out is expected to
 463 occur shortly after the phase transition from partonic to hadronic matter and is followed
 464 by the kinetic freeze-out.

465 As explained in [16, 17, 18, 19], EPOS3 is an event generator based on 3+1D vis-
 466 cous hydrodynamical evolution starting from flux tube as an initial conditions, which are
 467 produced in the Gribov-Regge multiple scattering framework. An individual scattering is
 468 treated as a Pomeron, identified with a parton ladder, eventually showing up as flux tubes
 469 (or strings). Each parton ladder is composed of a pQCD hard process, plus initial and final
 470 state linear parton emission.

471 The final state partonic system (corresponding to a Pomeron) amounts to (usually two)
 472 color flux tubes, being mainly longitudinal, with transversely moving pieces carrying the
 473 p_T of the partons from hard scatterings. One has two flux tubes based on the cylindrical
 474 topology of the Pomerons. Each quark- antiquark pair in the parton ladder will cut a string
 475 into two; in this sense one may have more than two flux tubes. In any case, these flux
 476 tubes eventually constitute both bulk matter, also referred to as "core" (which thermalizes,
 477 flows, and finally hadronizes) and jets (also referred to as "corona"), according to some

478 criteria based on the energy of the string segments and the local string density. For the
479 core, we use a 3+1D viscous hydrodynamic approach, employing a realistic equation of
480 state, compatible with lQCD results. We employ for all calculations in this paper a value
481 of $\eta/s = 0.08$. Whenever a hadronization temperature of T_H is reached, we apply the
482 usual Cooper-Frye freeze-out procedure, to convert the fluid into particles. We use $T_H =$
483 166MeV. From this point on, we apply the hadronic cascade UrQMD [20, 21], about which
484 more details are given later. All hadrons participate in the cascade, including those from
485 the core (after freeze- out) and the corona. The corona particles, from string decay, are only
486 "visible" after a certain formation time (some constant of order one fm/c), multiplied by
487 the corresponding gamma factor), so very high p_T particles have a good chance to escape.

488 The UrQMD model is a non-equilibrium transport approach. The interactions of
489 hadrons in the current version include binary elastic and $2 \rightarrow n$ inelastic scatterings, res-
490 onance creations and decays, string excitations, particle + antiparticle annihilations as
491 well as strangeness exchange reactions. The cross sections and branching ratios for the
492 corresponding interactions are taken from experimental measurements (where available),
493 detailed balance relations and the additive quark model. The model describes the full
494 phase-space evolution of all hadrons, including resonances, in a heavy- ion collision based
495 on their hadronic interactions and their decay products. Due to the short lifetime of res-
496 onances, their decay products may interact in the hadronic phase. This is not the case
497 for weak decays, where the system has already decoupled at the time of the decay. As
498 discussed previously, the experimental reconstruction of resonances will be influenced by
499 the final state interactions of the decay products. Resonance signals have been previously
500 studied using the UrQMD model.

501 **3 Production of hyperon resonance**

502 The Quark Model, proposed independently by Murray Gell-Mann and Yuval Ne'eman in
 503 1964 [22], enables the classification of hadrons in terms of their constituent quarks. In
 504 this model, the lighter mesons and baryons are representations of an $SU_f(3)$ group, whose
 505 fundamental representation is the three dimensional vector (u, d, s). These are the three
 506 lighter quarks whose characteristics are reported in Table reftable:quark.

Light flavor	d	u	s
Baryon number (B)	+1/3	+1/3	+1/3
Electric charge (Q)	-1/3	+2/3	-1/3
Isospin (I)	-1/2	+1/2	0
Strangeness (S)	0	0	-1
mass (MeV/c^2)	$2.3^{+0.7}_{-0.5}$	$4.8^{+0.5}_{-0.3}$	95 ± 5

Table 6: Quantum numbers and masses associated to the three lighter quarks: u, d and s

507 The hadronic state are obtained from the decomposition of the following scalar prod-
 508 ucts of the fundamental representations of the group:

509 $\text{Meson } (q\bar{q}) : 3 \otimes \bar{3} = 1 \oplus 8$

510 $\text{Baryon } (qqq) : 3 \otimes 3 \otimes 3 = 10_S \oplus 8_M \oplus 8_M \oplus 1_A$

511 For the baryons without c or b quark, flavor and spin may be combined in an approxi-
 512 mate flavor-spin $SU(6)$, in which the six basic states are $d \uparrow, d \downarrow, \dots, s \downarrow$ (\uparrow, \downarrow = spin up,
 513 down). Then the baryons belong to the multiplets on the right side of

514 $6 \otimes 6 \otimes 6 = 56_S \oplus 70_M \oplus 70_M \oplus 20_A$

515 Here, the 56 representation can be decompose in an octet ($J^P = 1/2^+$) and a decuplet
 516 ($J^P = 3/2^+$), as can be seen in Figure 8 and Figure 9.

517 Among these hadrons, the special family of particles that contain at least one strange
 518 quark but not heavier quarks (like charm or bottom), are called hyperons. These are:
 519 the Λ (uds), the triplet $\Sigma^+(uus)$, $\Sigma^0(uds)$, $\Sigma^-(dds)$, the doublet $\Xi^-(dss)$, $\Xi^0(uss)$ and the
 520 $\Omega(sss)$ and the corresponding antiparticles. Ξ and Ω are the only hyperons containing more
 521 than one strange quark, hence they are called multi-strange baryons. Resonances shown
 522 in Figure reffig:decuplet having * with its name (e.g. $X^{*\pm}$) are particles which have higher
 523 mass than the corresponding ground state particle with the same quark content.

524 Different resonances having various lifetimes (Table 7) can be used as tool to explore
 525 different stages of the fireball expansion as discussed in section 1.3. In order to have

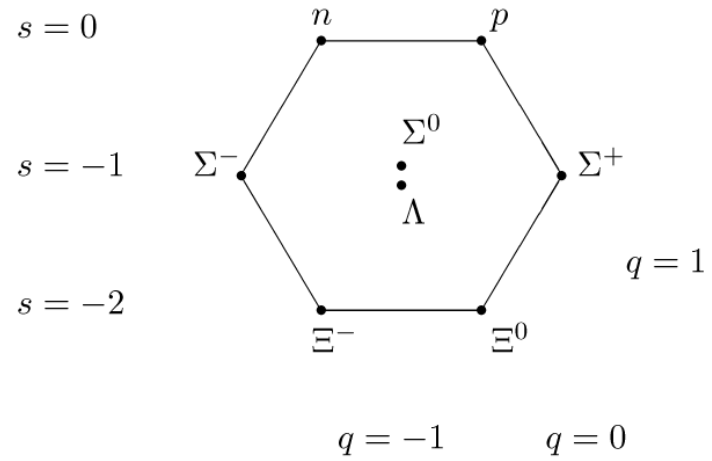


Figure 8: The $J^P = 1/2^+$ ground state baryon octet

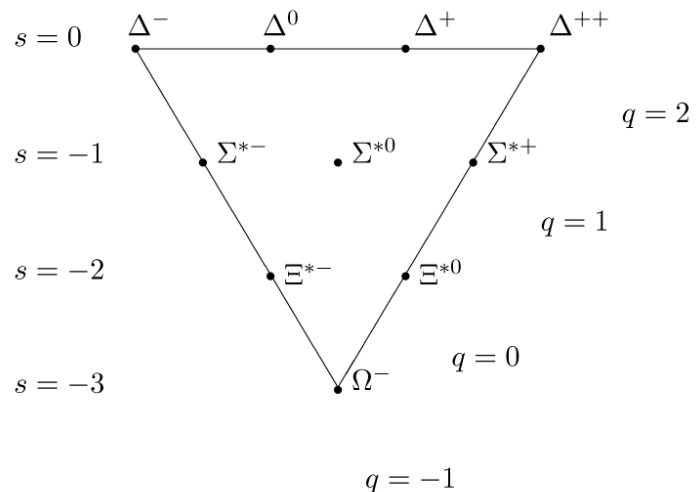


Figure 9: The $J^P = 3/2^+$ baryon decuplet

531 insight on the role of the re-scattering effect between the freeze-out phases, it is important
 532 to measure the ratio between resonances and stable hadrons and compare it with different
 533 lifetimes.

Particle	$\rho(770)$	$\Delta(1232)$	$K^*(892)$	$\Sigma(1385)$	$\Lambda(1520)$	$\Xi(1530)$	$\Phi(1020)$
Lifetime[c τ]	1.3 fm	1.7 fm	4.0 fm	5.5 fm	10.3 fm	22 fm	46 fm

Table 7: Lifetime of hadronic resonances

534 In the following, a general overview of the role of the strange quark within the QGP
 535 studies with heavy-ion collisions is given. And importance of the measurement of resonance
 536 is explained as probe of properties in the duration of hadronic phase from the chemical(T_{ch})
 537 to the kinetic freeze-out(T_{kin}).

538 3.1 Strange quark and hyperons

539 The original interest in the strangeness in the context of the QGP comes from an idea by
 540 Johann Rafelski and Berndt Müller. In 1982, they suggested a possible signature for the
 541 formation of a QGP in a heavy-ion collision [23]. The key argument, at a fixed collision
 542 energy, rests on the different production mechanism of the s quark within two different
 543 systems:

544 **1. Hadron Gas (HG)** , where the degrees of freedom are the hadronic ones, as quark and
 545 gluons are confined. The great abundance of pions in the HG suggests to consider the
 546 production of strange particles from the reaction between them. Direct production
 547 can be observed with $\pi + \pi \rightarrow \pi + \pi +$ strange hadron + antiparticle, considering
 548 the baryon and strange number conservation. This means that, in order to create the
 549 strange particle and anti-particle at once, the reaction threshold (energy needed to
 550 produce mesons or baryons) corresponds to tow times the rest mass of the hadrons.
 551 (2230 MeV for $\Lambda + \bar{\Lambda}$, 2642 MeV for $\Xi + \bar{\Xi}$. 3344 MeV for $\Omega + \bar{\Omega}$)

552 **2. QGP** , where the degrees of freedom are partonic ones, with quarks and gluons free
 553 with respect to each other. The high gluon density gives the possibility to have
 554 new production mechanisms abreast the usual quark-pair annihilation which are the
 555 gluon fusion processes. It becomes the dominant process of $s\bar{s}$ pairs creation. In
 556 these reactions the energy threshold is equal to the naked mass of the two strange
 557 quarks $\approx 2 \cdot 100$ MeV.

558 The quarks can not be seen directly due to the strong interaction which keeps them
 559 confined. Once they are free, as in a QGP, the quarks recover their bare masses. (Note
 560 that, only the part of mass of hadron comes from the mass of the constituent quarks.) It
 561 was predicted that, if the QGP is formed, an enhancement of the strange quarks should

562 occur, because the production of $s\bar{s}$ pairs becomes easier due to the lower energy needed as
 563 explained above. When the QGP cools down, these strange quarks eventually recombine
 564 into hadrons favoring also an enhancement of the number of strange hadrons. This effect is
 565 larger for hadrons with higher strangeness, with the following scaling for the number type:
 566 Ordering in QGP: $N_\Omega > N_\Xi > N_\Lambda$

567 where N_Ω , N_Ξ , N_Λ are the number of produced Ω , Ξ and Λ . A certain enhancement of
 568 strange hadrons can occur also in a hadron gas system, but the processes of hadronisation
 569 in this case are relatively easy for K and Λ . and progressively harder for hadrons with
 570 higher strangeness, hence the relation would be:

571 Ordering in HG: $N_\Omega < N_\Xi < N_\Lambda$.

572 The measurement of multi-strange hadrons in heavy-ion collisions with respect to small
 573 collisions is considered to be a signature of the formation of the QGP and it was observed
 574 at SPS, RHIC and LHC. [24]

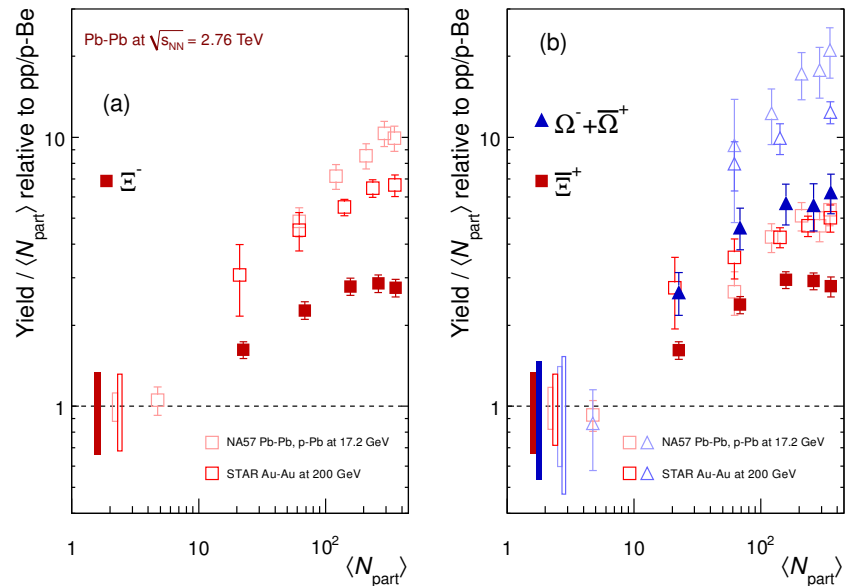


Figure 10: Integrated yield relative to small system (pp or p-Be) as a function of the mean number of participants $\langle N_{part} \rangle$ in the rapidity range $|y| < 0.5$. The results from ALICE are presented as full symbols, RHIC and SPS data are shown as open symbols. Boxes on the dashed line at unity represent statistical and systematic uncertainties on the pp or p-Be reference.

575 The measured enhancement factors of baryons with increasing strangeness content are
 576 reported in Figure 10 as a function of the mean number of participants, $\langle N_{part} \rangle$, com-
 577 pared with measurements at SPS and RHIC. As shown in the Figure 10, the enhancement

578 increases with $\langle N_{part} \rangle$ which is variable to be comparable to the centrality in Pb–Pb collisions and the effect is more pronounced for particle with larger strangeness content. If one
 579 consider the collision energy dependency, the comparison with measurement from the previous experiment shows that the relative enhancements decrease with increasing energy.
 580 An explanation of this behavior is given in terms of a statistical model, with canonical
 581 strangeness conservation.
 582

583 In a large system with a large number of produced particles, the conservation law of
 584 a quantum number, e.g., strangeness, can be implemented on the average by using the
 585 corresponding chemical potential. This is the Grand Canonical formulation that was dis-
 586 cussed in previous Section. In a small system, however, with small particles multiplicities,
 587 conservation laws must be implemented locally on an event-by-event basis.
 588

589 This is the Canonical formulation which conservation of quantum numbers is known
 590 to severely reduce the phase space available for particle production.[25]. This canonical
 591 suppression factor decreases with lower energy in the centre of mass of the collisions and
 592 could explain the larger enhancement for lower energy systems.
 593

3.2 Resonance production

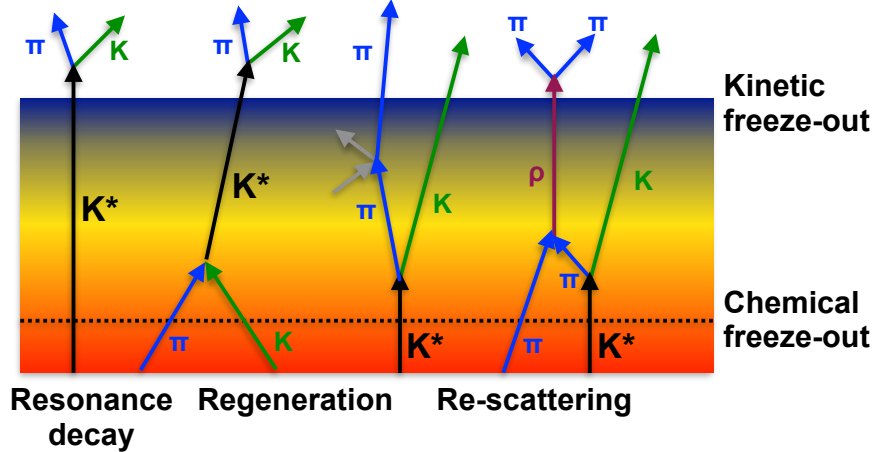


Figure 11: Hadronic phase

594 Resonances are particles with larger mass than the corresponding its ground state
 595 particle which has the same quark content. Because of the hadronic resonances decay
 596 strongly in the medium, it has short lifetime(τ) in the order of few fm/c which is comparable
 597 to the lifetime of the fireball. The natural width of resonances is given by $\Gamma = \bar{h}/\tau$, which
 598 is inversely proportion to the lifetime. In heavy-ion collisions, the hadronic resonances are
 599

599 produced in medium which is still expanding so that the particles could interact with the
600 medium and decay while traveling it. The particles can be measured only via reconstruction
601 of their decay products in a detector, since it decays very shortly after being produced.

602 The effects which can be happened in the hadronic phase is shown in Figure 11. In the
603 left on the figure, as example, there is sketch of the original resonance decay of $K^*(892)^0$
604 ($K^*(892)^0 \rightarrow \pi+K$). It is possible that resonances may be regenerated via pseudo-elastic
605 scattering of decay products ($\pi+K \rightarrow K^*(892)^0 \rightarrow \pi+K$) in the time duration between the
606 chemical (T_{ch}) and the kinetic freeze-out (T_{kin}). Conversely, in case that the decay product
607 undergo elastic scattering or pseudo-elastic scattering through a different resonance in the
608 medium, e.g. ρ in the Figure 11, the invariant mass of the daughters can not mach that of
609 the parent particle. As a results, yield after kinetic freeze out could be smaller than the
610 yields originally produced.

611 These re-scattering and regeneration depend on the lifetime of the resonances and
612 affect the their yield and momentum spectrum. The yield is increase if the regeneration
613 dominates, vice versa, it is decrease with re-scattering effect. In order to understand the
614 properties in hadronic medium, the ratios between resonances and stable hadrons have to
615 be studies and the results are compared with model predictions discussed in Section 2.

616 **4 A Large Ion Collider Experiment at the LHC**

617 ALICE (A Large Ion Collider Experiment) is one of major experiment at LHC (Large
618 Hadron Collider) in Geneva and it is dedicated experiment for the study of QCD matter
619 created in high-energy collisions [26]. It has been accumulating data during the whole first
620 phase of the LHC operation, from end of 2009 to the beginning of the technical shutdown
621 2013. During that time, the beam energy was tuned to have data in pp collisions at 0.9,
622 2.76, 7 and 8 TeV, p–Pb collisions at 5.02 TeV and Pb–Pb collisions at 2.76 TeV.

623 The section 4.1 aims to explain the LHC operation of the first phase and includes
624 each experiments builed in LHC. Next section (4.2.1) focuses on general description of
625 the ALICE detector and detailed explanation of sub-detectors used in this analysis will
626 given. And then the particle identification performance is discussed. The Data Acquisition
627 (DAQ) system and trigger system follow in Section 4.2.2. The last section account for
628 offline software frame work.

629 **4.1 The Large Hadron Collider**

630 The Large Hadron Collider (LHC) [27] at CERN is the world’s largest particle accelerator.
631 It provides maximum possible energies of 7 TeV for proton beam and 2.76 per nucleon
632 for beam of lead ions, hence, providing collisions at $\sqrt{s} = 14$ TeV and $\sqrt{s_{NN}} = 5.5$ TeV,
633 respectively. These energies are largest one ever achieved in particle collision experiment.

634 The LHC is a two ring superconducting hadron accelerator and collider built in the
635 26.7 kM tunnel. In separate parallel beam pipe, there are two counter-rotating beams and
636 the bunches of particles in each of them rotate many time up to collision energy is reached.
637 The accelerator keeps to bend the beam around the ring to maintain focused bunches and
638 enlarge them to their collision energy. In the end, the spatial dimension of the each bunches
639 turns into minimized to obtain high luminosity guarantee a high number of collisions per
640 time interval at the collisions points. In order to acheive it, combination of magnetic and
641 electric field have been performed. In spite of the high luminosity, very small portion of
642 the particles of two bunches collides in a single bunch crossing. The others are defocused
643 and continue to rotate the ring.

644 The CERN accelerator complex is shown in the Figure 12. The sequence of injection of
645 bunches into the LHC is started from acceleration in the LINAC (LINEar ACcelerator)2,
646 PS (Proton Synchrotron) booster, PS, and SPS (Super Proton Synchrotron) accelerators.
647 The way to inject of heavy-ion bunches are different. The bunches pass the LINAC3 instead
648 of LINAC2, LEIR (Low Energy Ion Ring), PS and SPS accelerators [?].

649 The first pp collisions at 900 GeV center of mass energy were delivered by the LHC on
650 September 10th 2008. Nine days later, the operations were interrupted due to a failure in
651 an electrical connection between two magnets. The machine operators spent over a year
652 repairing and consolidating the accelerator. On November, 2009 low energy proton beams
653 circulated again, and a few days later, by achieving the energy of 1.18 TeV per proton

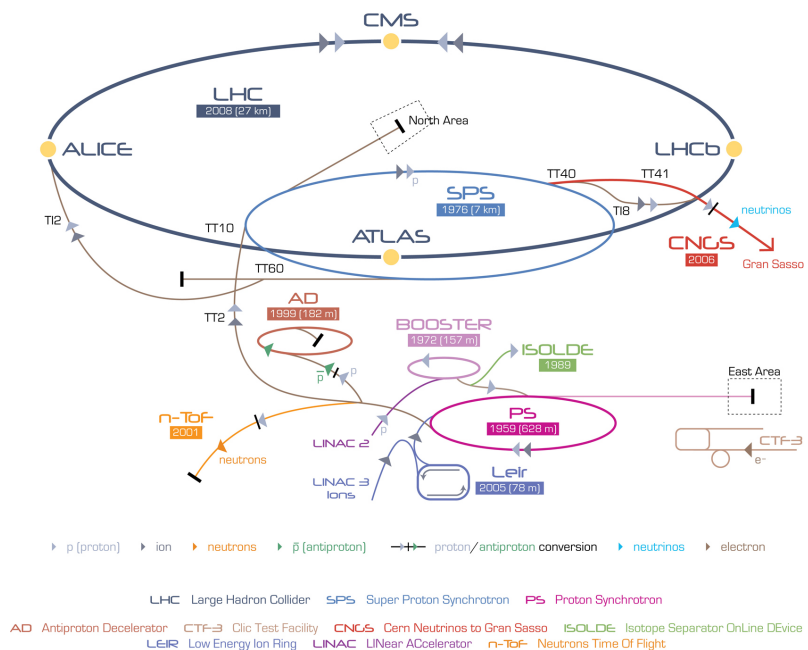


Figure 12: The CERN accelerator complex [3]

beam, LHC became the most powerful accelerator in the world. The first pp collisions at center of mass energy of 7 TeV were delivered in March 2010, and the first Pb–Pb collisions at center of mass energy of 2.76 TeV per nucleon pair in November 2010.

In 2010 the integrated luminosity delivered by the LHC was $\sim 48 \text{ pb}^{-1}$ for pp collisions at $\sqrt{s} = 7 \text{ TeV}$ ($\sim 0.5 \text{ pb}^{-1}$ in ALICE) and $\sim 10 \mu\text{b}^{-1}$ for Pb–Pb at $\sqrt{s_{\text{NN}}} = 2.76 \text{ TeV}$ ($\sim 9 \mu\text{b}^{-1}$ in ALICE) [26]. In 2011 the beam energy was the same as in 2010 both for pp and Pb–Pb. The performance of the LHC improved in terms of luminosity with $\sim 5.61 \text{ fb}^{-1}$ for pp ($\sim 4.9 \text{ pb}^{-1}$ in ALICE) and $\sim 166 \mu\text{b}^{-1}$ for Pb–Pb collisions ($\sim 146 \mu\text{b}^{-1}$ in ALICE). In 2012, the centre-of-mass energy for pp collisions was brought to 8 TeV and the integrated luminosity (up to December 2012, end of the pp program) was $\sim 23.3 \text{ fb}^{-1}$ ($\sim 10 \text{ pb}^{-1}$ in ALICE). A pilot p–Pb run operated at $\sqrt{s_{\text{NN}}} = 5.02 \text{ TeV}$ on September 2012, followed by a long p–Pb run on February 2013 with a delivered luminosity of 14 nb^{-1} . A very short pp run at $\sqrt{s} = 2.76 \text{ TeV}$ ended the Run1 of the LHC program, marking the start of the first long shutdown (LS1) until the end of 2014.

The LHC produces collisions in four so called Interaction Points (IPs) in correspondence of which are located six detectors of different dimensions and with different goals, all able to study the products of the interactions. These are:

ALICE (A Large Ion Collider Experiment-IP₂) [28] is a dedicated heavy-ion experiment designed to study strongly-interacting matter at very high energy density. It explores the phase transition to the QGP, its phase diagram, and its properties. Furthermore, ALICE will also study collisions of protons, on one hand as a baseline for heavy-ion measurements and on the other hand it contributes to measurements of identified particles by making use of its excellent particle identification capability and its acceptance at very low transverse momenta.

ATLAS (A Toroidal LHC ApparatuS-IP₁) and CMS (Compact Muon Solenoid - IP₅) [29][30] are general-purpose detectors for pp collisions that are built to cover the widest possible range of physics at the LHC. Specific topics are the search for the Higgs boson and physics beyond the Standard Model, e.g. new heavy particles postulated by supersymmetric extensions (SUSY) of the Standard Model and evidence of extra dimensions.

LHCb (The Large Hadron Collider beauty experiment-IP₈) [31] is a dedicated experiment for the study of heavy flavor physics at the LHC. In particular, the experiment focuses on the study of CP violation and rare decays of beauty and charm particles, to test the Standard Model and to search for evidence of New Physics. The LHCb physics program is complementary to the flavor physics studies conducted at the B-factories and to the direct searches for new particles performed at ATLAS and CMS.

LHCf (Large Hadron Collider forward experiment-IP₁) [32] measures forward particles created during LHC collisions to provide further understanding of high energy

695 cosmic rays. The detector is placed close to the ATLAS experiment.

696

697 **TOTEM (TOTal Elastic and diffractive cross-section Measurement-IP₅)** [33]
698 measures the total cross-section, elastic scattering, and diffractive processes. The detector
699 is located close to the CMS experiment.

700

701 4.2 The ALICE project

702 The ALICE experiment at the LHC [34] has as main goal the study of nuclear matter
703 under extreme conditions of temperature and energy density such as those reached in ultra-
704 relativistic heavy-ion collisions. The aim is to verify the QCD prediction of the existence of
705 a phase transition from the common hadronic matter to the Quark-Gluon Plasma. Since
706 ALICE is the only LHC experiment specifically designed for Pb–Pb collisions, it has to
707 be able to cope with the large multiplicities associated with these collision systems and at
708 the same time has to cover as many QGP-related observables as possible. ALICE is also
709 interested in the study of pp interactions, as these are crucial for a comparison with Pb–Pb
710 collisions, to tune Monte Carlo models and per se, like the other LHC experiments. With
711 respect to these experiments, ALICE is endowed with an excellent Particle IDentification
712 (PID) performance, obtained combining different PID techniques from different detectors
713 that are optimized in different momentum (p) regions.

714 4.2.1 ALICE detector

715 ALICE is a complex of 14 detector subsystems (Figure 13) that can be classified in three
716 groups:

717

718 **Central detectors** are housed in a solenoid magnet which provides the experiment
719 with a 0.5 T magnetic field and covers the pseudo-rapidity interval $-0.9 < \eta < 0.9$ (corre-
720 sponding to a polar acceptance $\pi/4 < \theta < 3\pi/4$). The azimuthal acceptance is 2π . They
721 are mainly dedicated to vertex reconstruction, tracking, particle identification and momen-
722 tum measurement. Starting from the interaction region and going outward, we find the
723 following detectors:

- 724 • Inner Tracking System (ITS)
- 725 • Time Projection Chamber (TPC)
- 726 • Transition Radiation Detector (TRD)
- 727 • Time Of Flight (TOF)

728 In the mid-rapidity region there are also three detectors with limited azimuthal accep-
729 tance:

- High Momentum Particle Identification Detector (HMPID)
- PHOton Spectrometer (POHS)
- ElectroMagnetic CALorimeter (EMCAL)

Muon spectrometer is placed in the forward pseudo-rapidity region ($-4.0 < \eta < -2.5$) and consists of a dipole magnet and tracking and trigger chambers. It is optimized to reconstruct heavy quark resonances (such as J/Ψ through their $\mu^+\mu^-$ decay channel) and single muons.

Forward detectors are placed in the high pseudo-rapidity region (small angles with respect to the beam pipe). They are small and specialized detector systems used for triggering or to measure global event characteristics. They are:

- Time Zero (T0) to measure the event time with precision of the order of tens of picoseconds, as needed by TOF
- VZERO (V0) to reject the beam-gas background and to trigger minimum bias events
- Forward Multiplicity Detector (FMD) to provide multiplicity information over a large fraction of the solid angle ($-3.4 < \eta < -1.7$ and $1.7 < \eta < 5$)
- Photon Multiplicity Detector (PMD) to measure the multiplicity and the spatial distribution of photons on an event-by-event basis in the $2.3 < \eta < 3.7$ region
- Zero Degree Calorimeter (ZDC) to measure and trigger on the impact parameter. The ZDC consists of two calorimeters, one for neutrons (ZDC:ZN) and one for protons (ZDC:ZP), and includes also an electromagnetic calorimeter (ZEM)

The ALICE global coordinate system [35] is a right-handed orthogonal Cartesian system with the origin X, Y, Z = 0 at the centre of the detector. The three Cartesian axes are defined as follows: the X axis pointing towards the centre of the LHC, the Y axis pointing upward and the Z axis parallel to the local mean beam line pointing in the direction opposite to the muon spectrometer. The azimuthal angle increases counter-clockwise from the positive X axis ($\Phi = 0$) to the positive Y axis ($\Phi = \pi/2$) with the observer standing at positive Z and looking at negative Z; the polar angle increases from the positive Z axis ($\theta = 0$) to the X-Y plane ($\theta = \pi/2$) and to the negative Z axis ($\theta = \pi$).

In the following Sections more specific descriptions of the detectors used in the identification of the $\Xi(1530)^0$ baryons and in the determination of the characteristics of typical collisions will be given.

ITS

The ITS [34] (Figure 14) is the barrel detector closest to the beam pipe. Its main goals are:

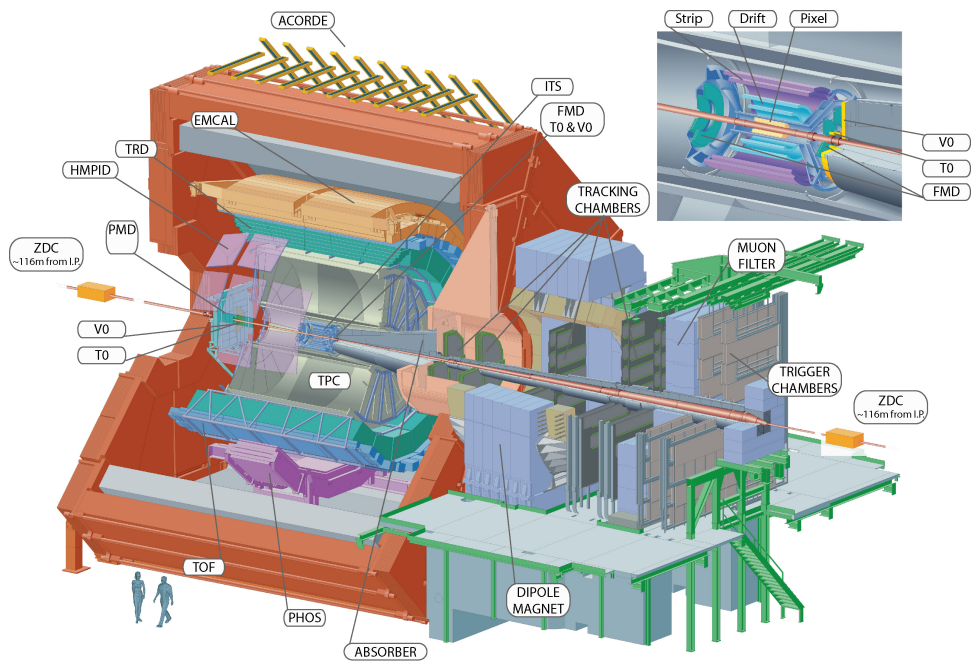


Figure 13: The ALICE detector

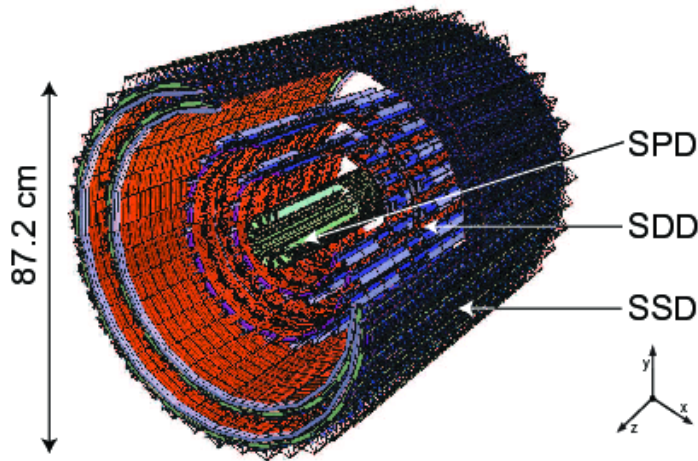


Figure 14: Schematic view of the ITS [4]

- 766 • to contribute with the TPC to the global tracking of ALICE by improving the angle
767 and momentum resolution
- 768 • to reconstruct the position of the primary interaction vertex
- 769 • to reconstruct secondary vertices from decays of heavy-flavor and strange particle
770 decays;
- 771 • to track and identify particles with momentum below $100 \text{ MeV}/c^2$
- 772 • to improve the momentum, impact parameter and angle resolution for the measure-
773 ment of high p_T particles performed with the TPC
- 774 • to reconstruct particles traversing dead regions of the TPC

775 The ITS surrounds the beam pipe (which is a $800 \mu\text{m}$ thick cylinder with an outer
776 diameter of 2.9 cm) and consists of six cylindrical layers of silicon detectors located at radii
777 between 4 cm and 43 cm . Due to the high track density, the two innermost layers are
778 Silicon Pixel Detectors (SPD) which guarantee a high granularity. They are followed by
779 two layers of Silicon Drift Detectors (SDD), while the two outmost layers are double-sided
780 Silicon micro-Strip Detectors (SSD).

781 Since the momentum and impact parameter resolutions for low momentum particles
782 are dominated by multiple scattering effects, the amount of material in the active volume
783 has been minimized as much as possible. The granularity of the detector was optimized to

784 keep the occupancy low in all the layers. With the technology chosen, the ITS detectors
 785 reach a spatial resolution of the order of a few tens of μm resulting in a resolution on the
 786 impact-parameter δ better than $70 \mu\text{m}$ in the r plane for $p_T > 1 \text{ GeV}/c$ and thus well suited
 787 for the reconstruction of heavy-flavor decays (see Figure 15).

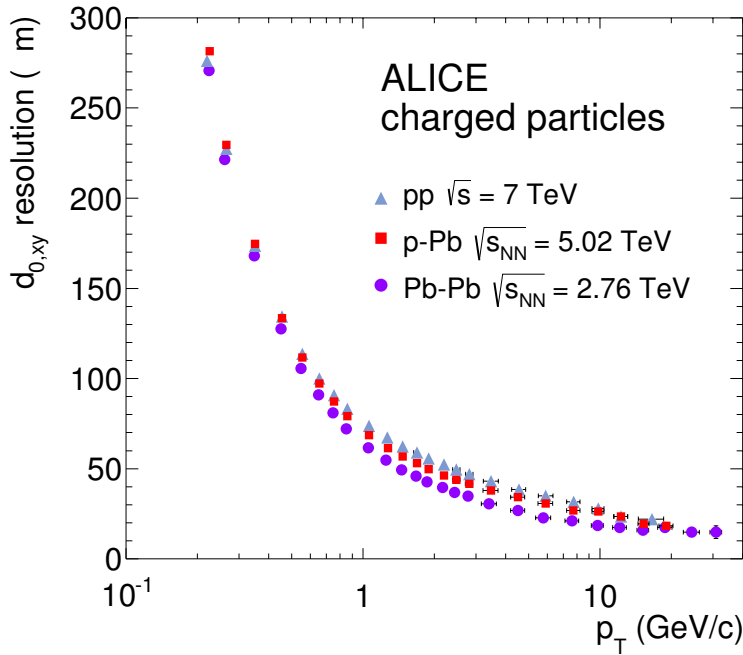


Figure 15: Track impact parameter resolution in the transverse plane ($r\phi$) vs p_T for charged particle

TPC

788 The TPC [36] (Figure 16) is the main tracking detector of the central barrel, optimized
 789 to provide, together with the other central barrel detectors, charged-particle momentum
 790 measurements with good two-track separation, particle identification and vertex determina-
 791 tion. The TPC was designed for an excellent tracking performance in the high multiplicity
 792 environment of Pb-Pb collisions. For this reason, it was chosen to be a drift chamber,
 793 cylindrical in shape, 5 m long, with the inner radius ($r_{in} \sim 85 \text{ cm}$) determined by the
 794 maximum acceptable track density, and the external one ($r_{ext} \sim 250 \text{ cm}$) by the minimum
 795 track length for which dE/dx resolution is $< 10\%$. The TPC volume is filled with 90 m^3 of
 796 Ne/CO₂/N₂ (90/10/5). The readout planes are divided in 18 sectors in which multi-wire
 797 proportional chambers (with cathode pad readout) are housed. Because of its good dE/dx
 798 resolution, the TPC can identify particles with $p_T < 1 \text{ GeV}/c$ on a track-by-track basis.
 799

800 Charged particles traveling through the TPC ionize the detector's gas; the measure-

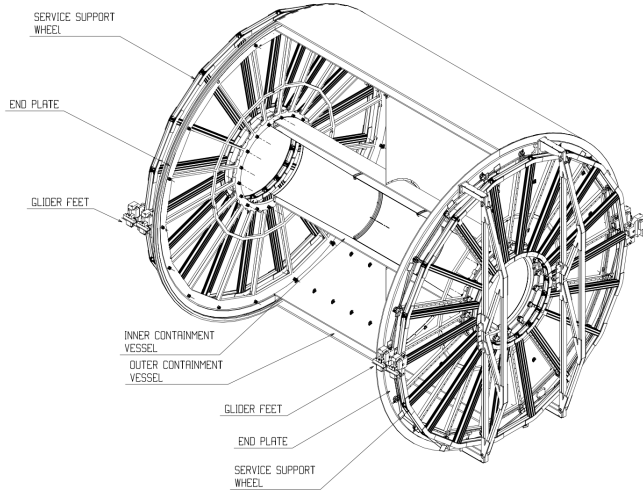


Figure 16: Schematic view of the TPC

801 ment of this loss of energy is what we need to identify a particle. The physics observable
 802 in this case is the energy loss per unit length, within the matter crossed by the charged
 803 particle, which we call specific energy loss, also denoted by dE/dx . This is described by
 804 the Bethe–Bloch equation, 5, that highlights the key of the identification technique: this
 805 observable depends only on the charge and on velocity (β) of the particle, which, in turn,
 806 depends only on the momentum and the mass of the ionizing particle. Since momentum is
 807 already known due to track curvature and charge is unitary for most measured tracks, mea-
 808 suring the dE/dx allows us to indirectly determine mass and thus determine the particle
 809 species. The Bethe-Bloch equation gives the mean specific energy loss:

$$-\langle \frac{dE}{dx} \rangle = k_1 \cdot z^2 \frac{Z}{A} \cdot \frac{1}{\beta^2} [\frac{1}{2} \ln(k_2 \cdot m_e c^2 \cdot \beta^2 \gamma^2) - \beta^2 + k_3] \quad (5)$$

810 where $\beta\gamma = p/Mc$ and: Z: atomic number of the ionized gas (in this case Ne/CO₂/N₂)
 811 A: mass number of the ionized gas (g/mol)
 812 m_e : electron mass
 813 z: electric charge of the ionizing particle in unit of electron charge e
 814 M: ionizing particle mass
 815 p: ionizing particle momentum
 816 β : ionizing particle velocity normalized to the light velocity c
 817 $\gamma = 1/\sqrt{1 - \beta^2}$, Lorentz factor
 818 k_1 , k_2 , k_3 : constants depending on the ionized medium
 819

820 For a given ionizing particle mass hypothesis, a given momentum and a given length
 821 of the trajectory in the ionizing medium, the total charge deposited along the trajectory
 822 is subject to statistical fluctuations. This random variable follows a Landau distribution,
 823 that give us the opportunity to measure the mean value $h dE/dx$. The long tail of the
 824 Landau distribution is usually truncated at 50%-70% of the collected signal.

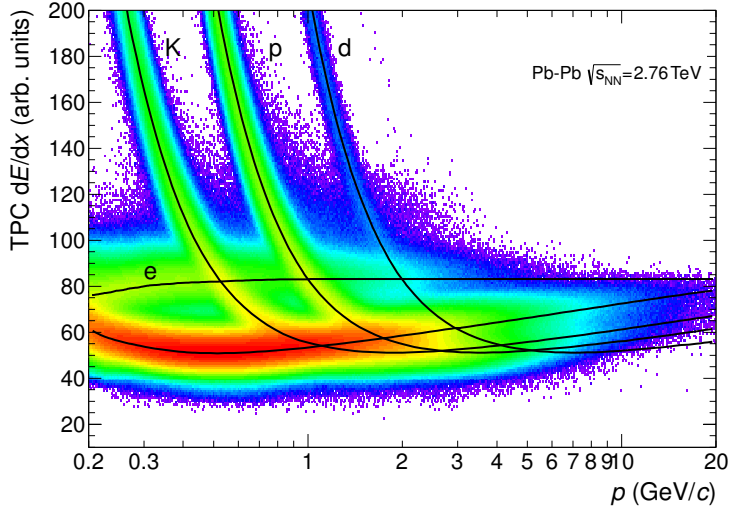


Figure 17: Specific energy loss (dE/dx) in the TPC vs. particle momentum in Pb–Pb collisions at $\sqrt{s_{NN}} = 2.76 \text{ TeV}$. The lines show the parametrisations of the expected mean energy loss.

825 The specific energy loss in the TPC as a function of momentum is shown in Figure
 826 17. The different bands characteristic for e^\pm , π^\pm , K^\pm , p^\pm are clearly visible. These
 827 are the evidence of the statistical distribution of the measured energy loss around the
 828 expected mean value. The expected value correspond to the prediction by a Bethe–Bloch
 829 experimental parametrization (superimposed as black lines in the Figure). For a track
 830 within the TPC the relevant quantity to be considered for PID is the difference between
 831 the measured specific energy loss and the corresponding predicted value, by the Bethe–
 832 Bloch parametrization for a given measured momentum. If normalized to the resolution
 833 of the dE/dx measurement in the TPC, this difference could be expressed in number of
 834 σ (see Equation 6). In this way it is possible to estimate more quantitatively the goodness
 835 of a mass hypothesis. This also gives us the possibility to choose the strictness we want to
 836 adopt in the identification of a particle (n_σ , $n = 2, 3, 4$):

$$n_\sigma = \frac{(dE/dx)_{measured} - (dE/dx)_{Bethe-Bloch}}{\sigma_{TPC}} \quad (6)$$

V0

The VZERO detector [37] consists of two segmented arrays of plastic scintillator counters, called VZERO-A and VZERO-C, placed around the beam-pipe on either side of the IP: one at $Z = 340$ cm, covering the pseudo-rapidity range [2.8; 5.1], and the other at $Z = -90$ cm (in front of the absorber), covering the pseudo-rapidity range [-3.7; -1.7]. They consist of 32 counters distributed in four rings, each divided in eight 45 sectors. Each counter is made of scintillator material embedded with WaveLength Shifting fibers. Clear fibers collect and transport the signal to photomultipliers 3 - 5 m far from the detector, inside the L3 magnet. The counters have a time resolution better than 1 ns. Their response is recorded in a time window of 25 ns around the nominal beam crossing time. The VZERO has an important role in rejecting background from beam-gas collisions (see, Figure 18) exploiting the relative time-of-flight measurement between the two arrays: when the beam-gas collision takes place outside the region between the two arrays, particles arrive 6 ns before or after the time of a beam-beam collision.

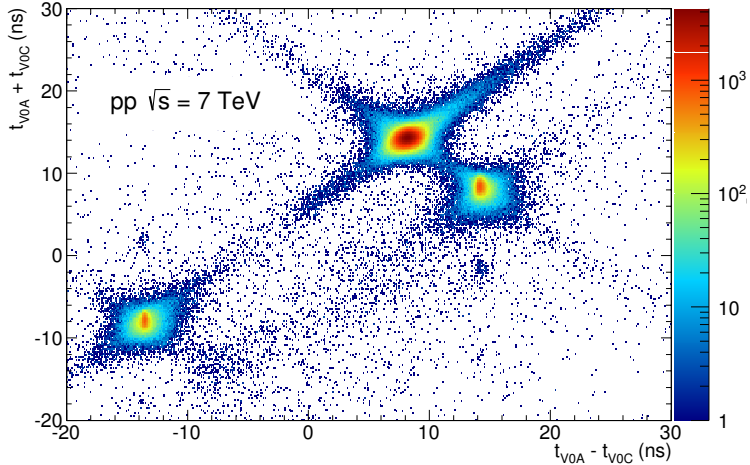


Figure 18: Correlation between the sum and difference of signal times in V0A and V0C. Three classes of events collisions at (8.3 ns, 14.3 ns), background from Beam 1 at (-14.3 ns, -8.3 ns), and background from Beam 2 at (14.3 ns, 8.3 ns) can be clearly distinguished.

The VZERO is a trigger detector that will provide a minimum-bias trigger for all colliding systems to the central barrel detectors and three centrality triggers in p-Pb and Pb-Pb collisions (multiplicity, central and semi-central).

The first parameter to be determined in A-A(p-A) collisions is the centrality(multiplicity). This is defined according to the value of the impact parameter, b , and provides a geometrical scale of the overlapping region between the colliding nuclei: a collision will be defined

from central to peripheral, as the impact parameter increases. The centrality of a collision is not directly available and must be deduced from a combination of experimentally measured quantities and Monte Carlo simulations. There are a number of observables that can be measured and used as centrality estimators. The charged-particle multiplicity N_{ch} and the transverse energy E_T measured around mid-rapidity are measurable quantities related to the energy deposited in the interaction region (these are therefore related to N_{part}). These variables increase significantly increasing the centrality of the collisions. Another measurable quantity to estimate the centrality is the zero-degree energy $EZDC$, namely the energy carried by spectator nucleons $N_{spec} = 2A - N_{part} = EZDC/E_A$, where E_A is the beam energy per nucleon. Typically a measured distribution of one of the previous observables is mapped to the corresponding distribution obtained from phenomenological Glauber calculations. The Glauber model [38, 39] uses a semi-classical approach: the $A?A$ collision is assumed to be an incoherent superposition of N elementary nucleon- nucleon collisions. The main parameters of the model are the inelastic nucleon- nucleon collision cross-section σ_n and the nuclear density distribution $\rho(r)$. In practice, the simulated distribution well reproduce the measured distribution or the latter is fitted with an analytical function. The experimental distribution can then be divided in classes with sharp cuts on the measured observable ($EZDC$, E_T or N_{ch}). These "centrality" classes will correspond to well defined percentage of the integral of the distribution. A given centrality class in the measured distribution, corresponds to the same class in the simulated distribution, where the main geometrical variables (N_{part} , N_{coll} and T_{AA}) can be determined. The number of classes that can be defined depends on the resolution achievable on the selection variable. In the analysis described in this thesis the centrality(multiplicity) estimation is based on the measurement of the multiplicities from the VZERO scintillators [40][41]. This is the method that achieve the best centrality resolution: it ranges from 0.5% in central to 2% in peripheral collisions. Other methods, as the ones based on the $EZDC$ measurement or based on the estimate of the number of tracks in the SPD or TPC, are used to asses a systematic uncertainty on the centrality determination. The distribution of the VZERO amplitudes is shown in Figure 19 where the centrality(multiplicity) percentiles are also indicated.

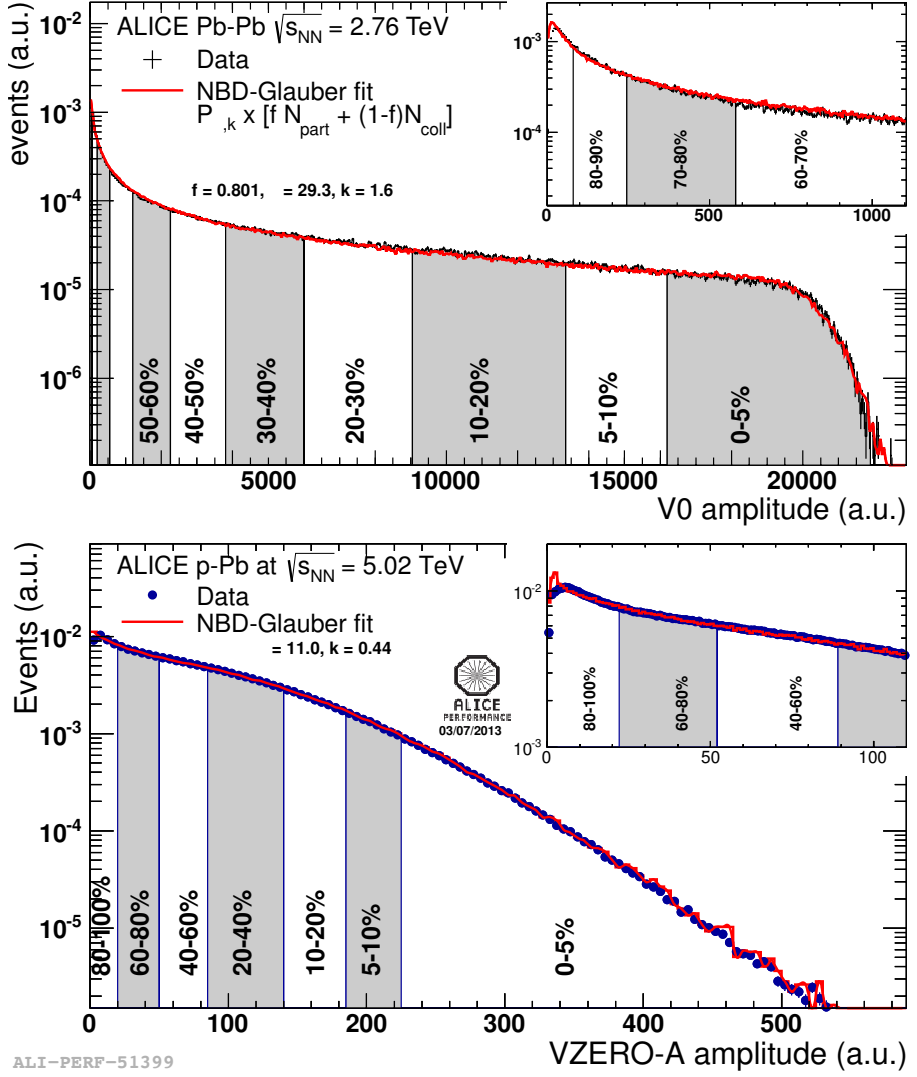


Figure 19: Distribution of the V0 amplitude (sum of V0A and V0C in top, V0A in bottom). The inset shows a magnified version of the most peripheral region.

887 **4.2.2 Data Acquisition (DAQ) and trigger system**

888 The architecture of data acquisition is shown in Figure 20. The tasks of the ALICE DAQ
 889 system are the assembly of event informations from individual detectors into complete
 890 events (event building) as well as buffering and export of assembled events to permanent
 891 storage. The DAQ is designed to process a data rate up to 1.25 GB/s in heavy-ion runs.
 892 Event building is done in two steps. Data from the detectors is received by Detector Data
 893 Links (DDLs) on Local Data Concentrators (LDCs). The LDCs assemble the data into
 894 sub-events that are then shipped to Global Data Collectors (GDCs). A GDC re- ceives all
 895 sub-events from a given event and assembles them into a complete event. These events are
 896 subsequently stored on a system called Transient Data Storage (TDS).

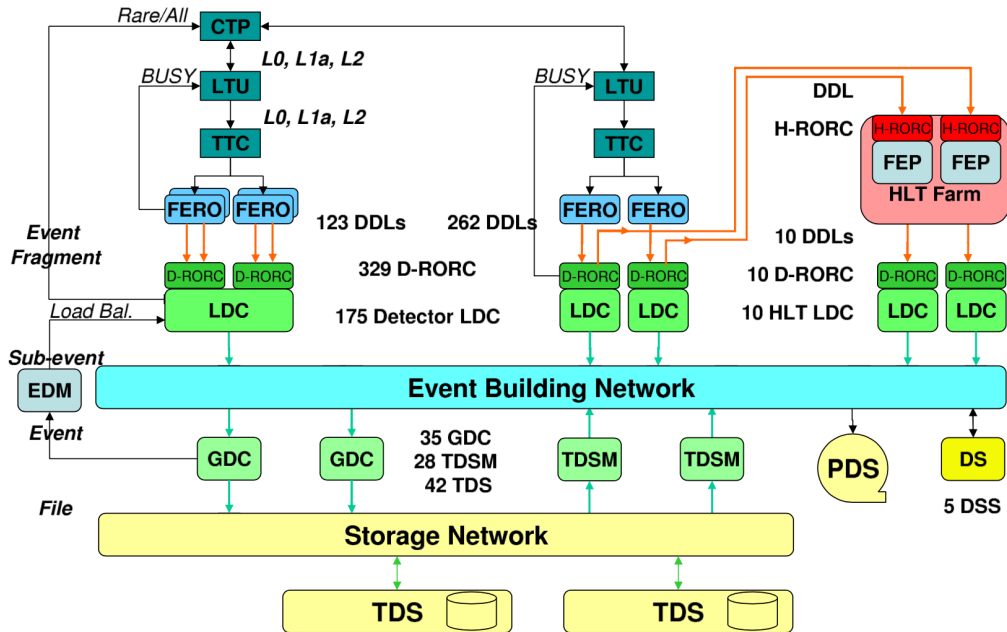


Figure 20: The overall architecture of the ALICE DAQ and the interface to the HLT system.

897 ALICE can simultaneously take data in several partitions, where a set of detec-
 898 tors can store their outputs. Since a partition is a group of commonly controlled detectors, a
 899 given detector can only be active in one partition at a time. The ac-
 900 tive detectors in a given partition may be assigned to data taking groups called clusters, for which triggers

901 can be defined. Therefore, upon a trigger only a sub-set of the whole partition may
902 be read out. Furthermore, a triggering detector does not have to be necessarily part of
903 the partition. ALICE has a two-layer trigger architecture [42]. The low-level trigger is a
904 hardware trigger called Central Trigger Processor (CTP). The High-Level Trigger (HLT)
905 is implemented as a pure software trigger. The CTP combines inputs from different trigger
906 sources, namely the various detectors. These inputs are single signals, like a hit in the
907 detector, or, can be the result of fast calculation performed directly in the detectors. The
908 HLT allows the implementation of sophisticated logic for the triggering. In contrast to the
909 CTP which governs the readout of the detectors, the HLT receives a copy of the data read
910 out from the detectors and processes them. The hardware trigger combines the trigger
911 signals of the various detectors to decide if an event is accepted, that means it is read out
912 and written to disk. Several trigger levels reduce the event rate depending on the input
913 signals. The first level, called L0, is delivered after 1.2 ?s, while the second, called L1,
914 after 6.5 ?s. The final trigger, L2, is delivered after 100 ?s, upon completion of the drift
915 time in the TPC. Only after an L2 trigger the event is finally stored. The rates of different
916 trigger classes are very different. By definition minimum-bias triggers have the highest
917 rate; other triggers that look for rare signals are characterized by much lower rates. In
918 order to cope with different scenarios, downscaling factors can be applied to the trigger
919 classes individually, i.e. only every nth event fulfilling the trigger condition is read out. The
920 total recording rate is limited by the maximum bandwidth of data that can be recorded
921 to disk and tape. The ALICE software trigger, called HLT, is a farm of multiprocessor
922 computers. The aim is to have about 1000 PCs processing the data in parallel allowing
923 an online analysis of the events. A trigger decision comes from the analysis of a more
924 comprehensive set of information than what happens for the hardware trigger, giving the
925 possibility to apply more sophisticated triggers. Examples include triggers on high energy
926 jets or on muon pairs. Furthermore, the HLT can significantly reduce the event size by
927 selecting regions of interest (partial readout of detectors) and by further compression of the
928 data. The HLT receives a copy of the raw data and performs per detector reconstruction,
929 partly aided by hardware coprocessors. Subsequently, the trigger decision is based on the
930 global reconstructed event. In the same step a region of interest can be selected. In the
931 last optional step, if the trigger decision is positive, the data are compressed. The trigger
932 decision, partial readout information, compressed data, and the re-construction output
933 is sent to LDCs and subsequently processed by the DAQ. In terms of the overall DAQ
934 architecture, data sent by HLT is treated like stemming from a detector.

935 **4.2.3 ALICE offline software frame work**

936 The required computing resources for the reconstruction and analysis of the raw data as
937 well as the production of simulated events needed for the understanding of the data exceed
938 the computing power of single institutes and even centers like CERN. Therefore, institutes
939 that are part of the Collaboration also provide storage and computing resources. Distribu-
940 tion of the data for reconstruction and analysis cannot be performed manually and this
941 led to the need for an automated system. The concept of a decentralized computing model
942 called Grid [43] was identified as a solution.

943

944 *The AliEn Framework*

945 The Grid paradigm implies the unification of resources of distributed computing center,
946 in particular computing power and storage, to provide them to users all over the World.
947 It allows computing center to offer their resources to a wider community and the local re-
948 sources to be shared by an entire collaboration. Software that implements the Grid concept
949 is called Grid middleware. ALICE has developed a Grid middleware called AliEn [44] since
950 2001. An ALICE user employs AliEn to connect to the ALICE Grid which is composed
951 of a combination of general services that are provided by many Grid middleware solutions
952 and ALICE-specific services provided by AliEn. Parts of the ALICE Grid are: i) a global
953 file catalog that is a directory of files in storage elements distributed over the Globe, ii)
954 the automatic matching of jobs for execution to a suitable location in one of the connected
955 sites, iii) a shell-like user interface and iv) API9 services for the ROOT framework [45].

956

957 *AliRoot Framework*

958 AliRoot [34] is the offline framework for simulation, alignment, calibration, reconstruction,
959 visualization, quality assurance, and analysis of experimental and simulated data. It is
960 based on the ROOT framework. Most of the code is written in C++ with some parts in
961 Fortran that are wrapped inside C++ code. Re-usability and modularity are the basic
962 features of the AliRoot framework. Modularity allows parts of the code to be replaced,
963 with minimum or no impact on the rest (for example changing the event generator, the
964 transport Monte Carlo or the reconstruction algorithms). This is achieved implementing
965 abstract interfaces. In addition codes for each detector subsystem are independent modules
966 with their specific code for simulation and reconstruction and the code can be developed
967 concurrently with minimum interference. Re-usability is meant to maintain a maximum
968 amount of backward compatibility as the system evolves.

969 The central module of the AliRoot framework is STEER (Figure 21) which provides
970 several common functions such as: steering of program execution for simulation, reconstruc-
971 tion and analysis; general run management, creation and destruction of data structures,
972 initialization and termination of program phases; base classes for simulation, event genera-
973 tion, reconstruction, detectors elements. For event simulation the framework provides the
974 following functionality:

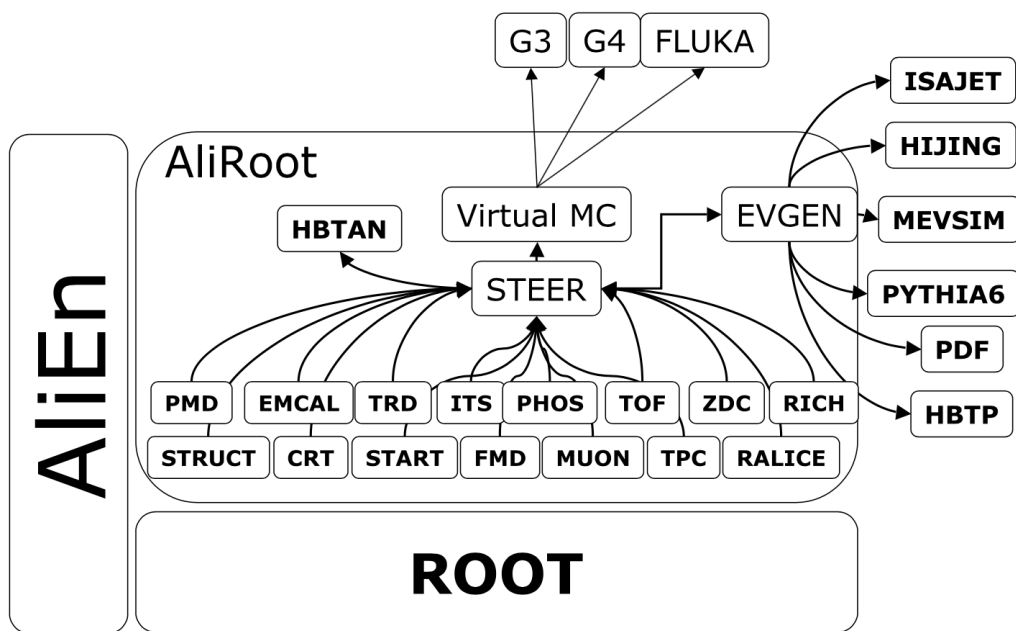


Figure 21: Schematic view of the AliRoot framework

975 **5 Measurement of $\Xi(1530)^0$ production in p–Pb and Pb–Pb**

976 The measurement of resonance production in p–Pb collisions helps to disentangle cold
977 nuclear matter effects from genuine hot medium effects and contribute to the study of
978 the system size dependence of re-scattering in the hadronic phase. And the measurement
979 in ultra-relativistic heavy-ion collisions such as Pb–Pb collisions, provide information on
980 the properties of hadronic medium and different stage of its evolution. In order to study
981 the particle production mechanism in the hadronic phase between the chemical and ki-
982 netic freeze-out, the $\Xi(1530)^0$ resonance production at mid-rapidity ($-0.5 < y_{\text{CMS}} < 0$) is
983 measured in p–Pb collisions $\sqrt{s_{\text{NN}}} = 5.02$ TeV and in Pb–Pb collisions with $|y| < 0.5$ at
984 $\sqrt{s_{\text{NN}}} = 2.76$ TeV with the ALICE experiment, via the reconstruction of its hadronic decay
985 into $\Xi\pi$.

986 **5.1 $\Xi(1530)^0$ -reconstruction**

987 The Ξ^{*0} production in p–Pb and Pb–Pb collisions at mid-rapidity has been studied in dif-
988 ferent multiplicity classes, from very central to peripheral collisions. The analysis strategy
989 is based on the invariant mass study of the reconstructed pairs (referred to as the candi-
990 dates) whose provenance could be the decay of a Ξ^{*0} baryon into charged particles. The
991 decay products (also called daughters in the text) are identified as oppositely charged Ξ and
992 π among the tracks reconstructed in the central barrel. The event selection, track selec-
993 tion and the particle identification strategy is described. The raw signal yield is extracted
994 by fitting the background-subtracted invariant mass distribution in several transverse mo-
995 mentum intervals. In order to extract the p_{T} -dependent cross section, these yields are
996 corrected for efficiency. The p_{T} -dependent correction due to the detector acceptance and
997 reconstruction efficiency, $(\text{Acc} \times \epsilon_{\text{rec}})(p_{\text{T}})$, is computed from a Monte Carlo simulation.
998 The absolute normalisation is then performed, by dividing for the number of the events in
999 each multiplicity and centrality classes.

1000 **5.1.1 Data sample and event selection**

1001 A description of the ALICE detector and of its performance during the LHC Run 1 (2010–
1002 2013) can be found in [34, 26]. The data sample in the analysis from Pb–Pb collisions with
1003 energy of $\sqrt{s_{\text{NN}}} = 2.76$ obtained during 2011 and the sample of p–Pb run at $\sqrt{s_{\text{NN}}} = 5.02$
1004 TeV was recorded in 2013.

1005 Due to the asymmetric energies of the proton (4 TeV) and lead ion (1.57 A TeV) beams,
1006 the centre-of-mass system in the nucleon-nucleon frame is shifted in rapidity by $\Delta y_{\text{NN}} =$
1007 0.465 towards the direction of the proton beam with respect to the laboratory frame of
1008 the ALICE detector [6]. For the analysed p–Pb data set, the direction of the proton beam
1009 was towards the ALICE muon spectrometer, the so-called “C” side, standing for negative
1010 rapidities; conversely, the Pb beam circulated towards positive rapidities, labelled as “A”

1011 side in the following. The analysis in this paper was carried out at midrapidity, in the
1012 rapidity window $-0.5 < y_{\text{CMS}} < 0$.

1013 The minimum-bias trigger during the p–Pb run was configured to select events by
1014 requiring a logical OR of signals in V0A and V0C [26], two arrays of 32 scintillator detectors
1015 covering the full azimuthal angle in the pseudo-rapidity regions $2.8 < \eta_{\text{lab}} < 5.1$ and
1016 $-3.7 < \eta_{\text{lab}} < -1.7$, respectively [46]. In the data analysis it was required to have a
1017 coincidence of signals in both V0A and V0C in order to reduce the contamination from
1018 single-diffractive and electromagnetic interactions. Out of this sample in p–Pb collision
1019 events about 109.3 million events, 93.9 million events satisfy the following selection criteria
1020 and have been actually used for the analysis.

1021 The Pb–Pb collisions data sample was selected by online centrality trigger requiring a
1022 signal in the forward V0 detectors[41] to record enhanced data in central collision. The
1023 data consists of 24.8 million events in most central collisions (0-10%), 21.8 million events in
1024 semi-central collisions (10-50%) and 3.5 million events with minimum-bas trigger (0-90%).
1025 Among 49.6 million events in total, 43.0 million events have been analyzed as passed the
1026 criteria below.

- 1027 • Events with z-coordinate of primary vertex (V_z) falling within ± 10 cm from the
1028 interaction point
- 1029 • Rejection of pile-up event
- 1030 • Requiring primary tracks to have at least one hit in one of the two innermost layers
1031 of the ITS (silicon pixel detector, SPD)
- 1032 • p–Pb: multiplicity ranges in percentile (V0A): 0-20%, 20-40%, 40-60%, 60-100% and
1033 MB(0-100%)
- 1034 • Pb–Pb: centrallity classes (V0A and V0C): 0-10%, 10-40%, 40-80% and MB (0-80%)

1035 The distribution of the vertex z position of the accepted events in p–Pb collision is
1036 reported on left panel in Figure 22 and corresponding figure but obtained from Pb–Pb
1037 collisions is shown on right panel in Figure. 22. Events with $|V_z| < 10$ cm have been used
1038 to ensure a uniform acceptance in the central pseudo-rapidity region, $|\eta| < 0.8$, where the
1039 analysis is performed. This cut reduces the total number of events to 97.5 million events,
1040 that is the $\sim 89.2\%$ of the initial sample in p–Pb collisions and 43.04 million events which
1041 is $\sim 86.8\%$ of the initial sample in Pb–Pb collisions are survived.

1042 Fig. 23 shows the multiplicity distribution of the accepted events in p–Pb collision
1043 divided in bins of percentile. The each color on the histogram indicate the multiplicity
1044 ranges used in this analysis. Corresponding events for each multiplicity range are in Table
1045 8.

1046 The distribution of centrality in each trigger used to select the events in Pb–Pb collision
1047 is shown in Fig. 24 and the reason why the centrality has step structure is that there are

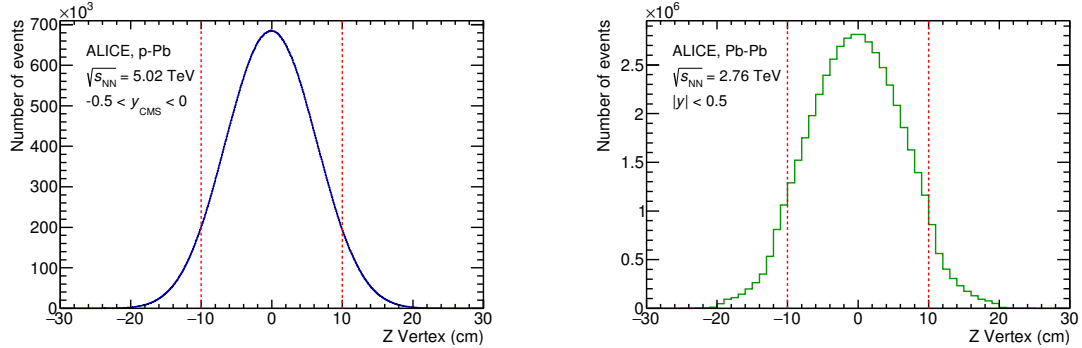


Figure 22: Vertex-z coordinate distribution of the accepted events in p–Pb collision(Left) and in Pb–Pb collisions(Right). The red dashed line indicates vertex cut

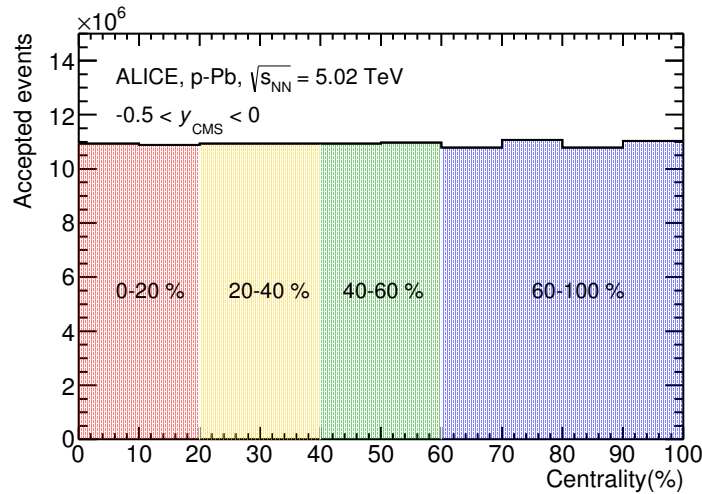


Figure 23: Multiplicity distribution of accepted events in p–Pb collision in percentile. The each color and labels define the four intervals in which the analysis is performed.

1048 three different trigger classes classified by the amplitude threshold on VZERO detector.
 1049 Because the distribution of events as function of centrality is not a flat, this may lead to
 1050 additional bias, in particular when one needs to combine the results from different triggers.
 1051 For example, events from 40-80% centrality bin have bias with high statistics in 40-60%. In
 1052 order to avoid this effect, we have applied a flattening procedure to have flat distribution
 1053 of events as function of centrality. A brief explanation of the method is below :

- 1054 1. Histograms are obtained for the effective mass distribution in 1% centrality bins and
 1055 for the centrality distribution

 1056 2. The effective mass distributions are scaled in each 1% centrality bin by a factor:
 1057 Factor = N_{event} in 20-40% / 20 / N_{event} in current 1% bin

 1058 3. Each bin in the centrality distribution is scaled using the factor described above

 1059 4. Histograms are added for centrality bins of interest: 0-10%, 10-40%, 40-80%, 0-80%

1060 The resulting number of events in each centrality classes is summarized in Table 8.

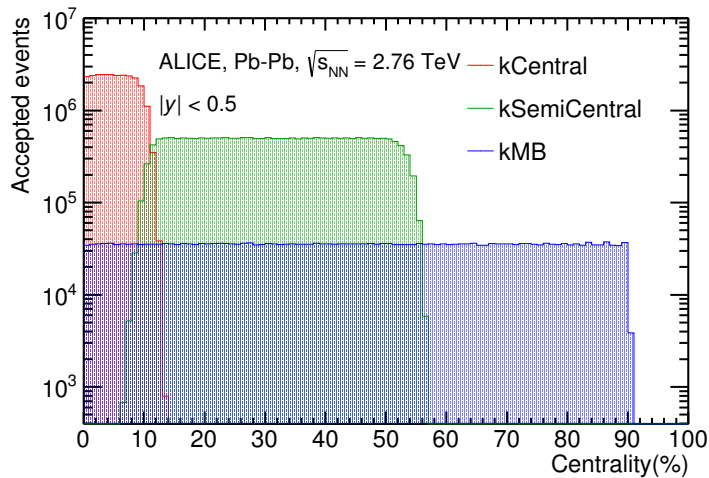


Figure 24: Centrality distribution of three different trigger classes.

p-Pb	0-20%	21.82×10^6
	20-40%	21.86×10^6
	40-60%	21.91×10^6
	60-100%	43.68×10^6
Pb-Pb	0-10%	5.58×10^6
	10-40%	16.73×10^6
	40-80%	22.31×10^6

Table 8: Number of accepted and analyzed events per multiplicity/centrality interval

5.1.2 Track and topological selection

In comparison with the Ξ^{*0} analysis carried out in pp collisions at $\sqrt{s} = 7$ TeV [8], track and topological selections were revised and adapted to the p-Pb dataset. Pions from strong decays of Ξ^{*0} were selected according to the criteria for primary tracks. As summarized in Table 9, all charged tracks were selected with $p_T > 0.15$ GeV/c and $|\eta_{\text{lab}}| < 0.8$, as described in Ref. [26]. The primary tracks were chosen with the Distance of Closest Approach (DCA) to PV of less than 2 cm along the longitudinal direction (DCA_z) and lower than $7\sigma_r$ in the transverse plane (DCA_r), where σ_r is the resolution of DCA_r . The σ_r is strongly p_T -dependent and lower than 100 μm for $p_T > 0.5$ GeV/c [26]. To ensure a good track reconstruction quality, candidate tracks were required to have at least one hit in one of the two innermost layers (SPD) of the ITS and to have at least 70 reconstructed points in the Time Projection Chamber (TPC), out of a maximum of 159. The Particle IDentification (PID) criteria for all decay daughters are based on the requirement that the specific energy loss (dE/dx) is measured in the TPC within three standard deviations (σ_{TPC}) from the expected value (dE/dx_{exp}), computed using a Bethe-Bloch parametrization [26].

Common track selections	$ \eta_{\text{lab}} $	< 0.8
	p_T	> 0.15 GeV/c
	PID $ (\text{d}E/\text{d}x) - (\text{d}E/\text{d}x)_{\text{exp}} $	$< 3 \sigma_{\text{TPC}}$
Primary track selections	DCA_z to PV	< 2 cm
	DCA_r to PV	$< 7\sigma_r$ - $10\sigma_r$ (p_T)
	number of SPD points	≥ 1
	number of TPC points	> 70
	χ^2 per cluster	< 4

Table 9: Track selections common to all decay daughters and primary track selections applied to the charged pions from decays of Ξ^{*0} .

Since pions and protons from weak decay of Λ ($c\tau = 7.89$ cm [1]) and pions from weak decay of Ξ^- ($c\tau = 4.91$ cm [1]) are produced away from the PV, specific topological and

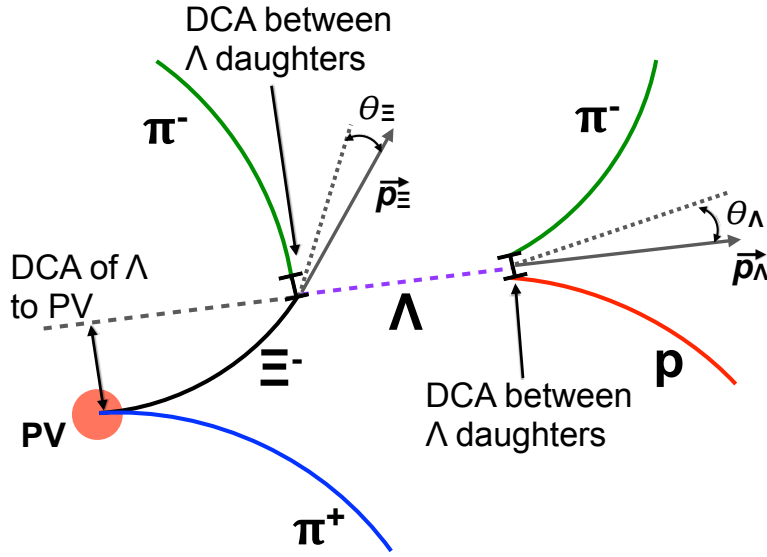


Figure 25: Sketch of the decay modes for Ξ^{*0} and depiction of the track and topological selection criteria.

1078 track selection criteria, as summarized in Table 10, were applied [7, 8, 47].

Topological cuts	p-Pb	Pb-Pb
DCA _r of Λ decay products to PV	> 0.06 cm	> 0.11 cm
DCA between Λ decay products	< 1.4 cm	< 0.95 cm
DCA of Λ to PV	> 0.015 cm	> 0.06
$\cos\theta_\Lambda$	> 0.875	> 0.998
$r(\Lambda)$	$0.2 < r(\Lambda) < 100$ cm	$0.2 < r(\Lambda) < 100$ cm
$ M_{p\pi} - m_\Lambda $	< 7 MeV/ c^2	< 7 MeV/ c^2
DCA _r of pion (from Ξ^-) to PV	> 0.015 cm	> 0.035 cm
DCA between Ξ^- decay products	< 1.9 cm	< 0.275
$\cos\theta_\Xi$	> 0.981	> 0.9992
$r(\Xi^-)$	$0.2 < r(\Xi^-) < 100$ cm	$0.2 < r(\Xi^-) < 100$ cm
$ M_{\Lambda\pi} - m_\Xi $	< 7 MeV/ c^2	< 7 MeV/ c^2

Table 10: Topological and track selection criteria.

1079 In the analysis of Ξ^{*0} , Λ and π from Ξ^- were selected with a DCA of less than 1.9 cm
1080 and with a DCA_r to the PV greater than 0.015 cm. The Λ daughter particles (π and p)

1081 were required to have a DCA_r to the PV greater than 0.06 cm, while the DCA between the
1082 two particles was required to be less than 1.4 cm. Cuts on the invariant mass, the cosine of
1083 the pointing angle ($\theta_\Lambda, \theta_\Xi$) and the radius of the fiducial volume ($r(\Lambda), r(\Xi)$) in Table 10
1084 were applied to optimize the balance of purity and efficiency of each particle sample.

1085 **5.1.3 Particle identification**

1086 PID selection criteria are applied for

- 1087 1. π^\pm (last emitted π) and proton from Λ
1088 2. π^\pm (second emitted π) from Ξ^\pm
1089 3. π^\pm (first emitted π) from $\Xi(1530)^0$

1090 by using TPC. On TPC dE/dx versus momentum distribution, 3σ cuts are applied to TPC
1091 for selecting each of the particles. The TPC dE/dx selection allows to have better signal
1092 with $\sim 20\%$ increase of significance.

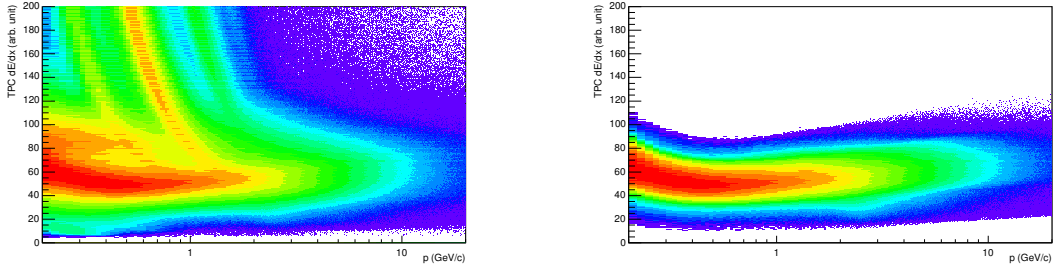


Figure 26: TPC dE/dx as function of transverse momentum for total (top) and selected first emitted π in 3σ (bottom)

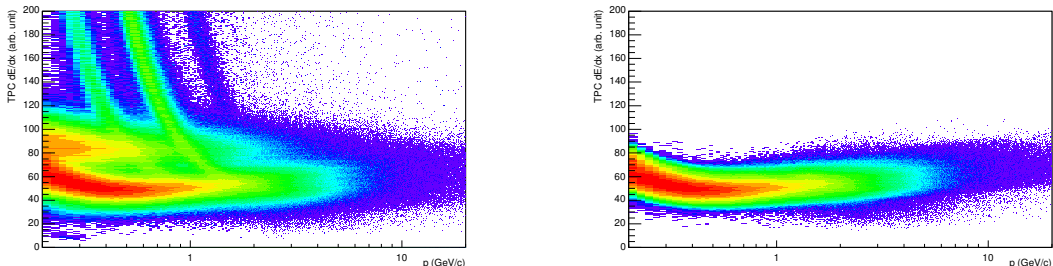


Figure 27: TPC dE/dx as function of transverse momentum for total (top) and selected second emitted π in 3σ (bottom)

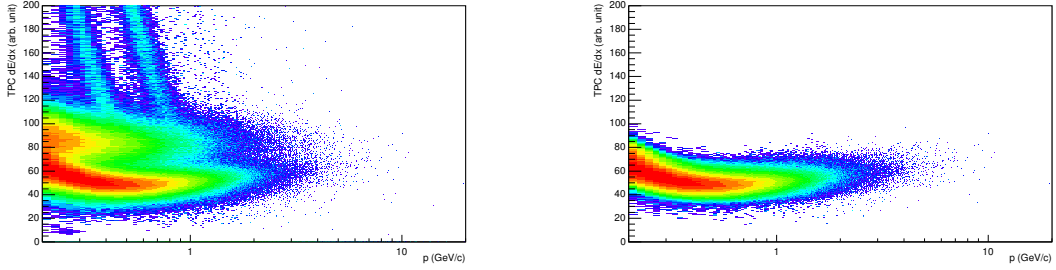


Figure 28: TPC dE/dx as function of transverse momentum for total (top) and selected last emitted π in 3σ (bottom)

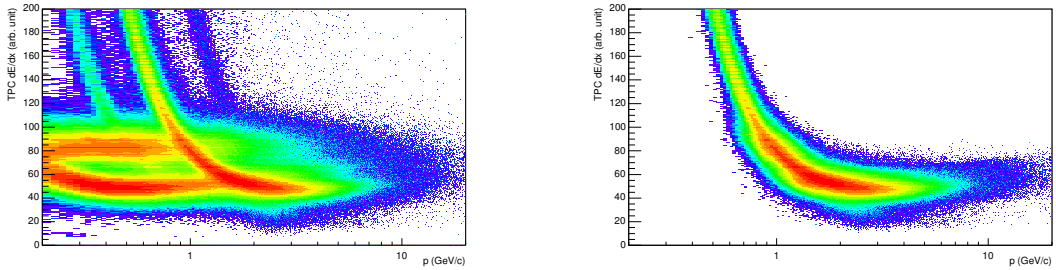


Figure 29: TPC dE/dx as function of transverse momentum for total (top) and selected proton in 3σ (bottom)

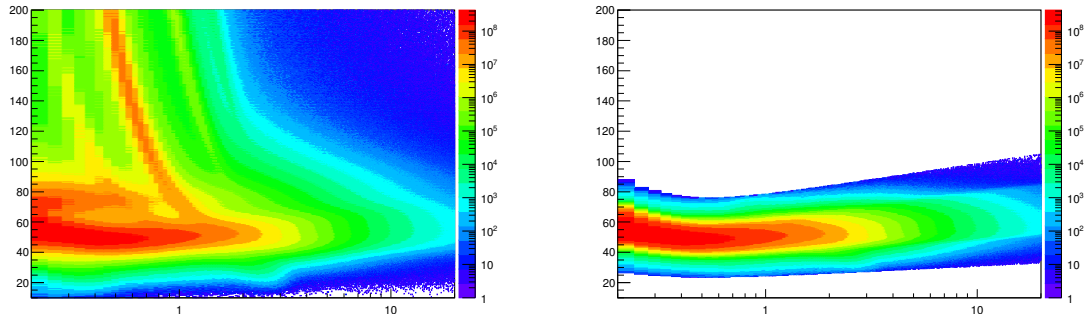


Figure 30: TPC dE/dx as function of transverse momentum for total (top) and selected first emitted π in 3σ (bottom)

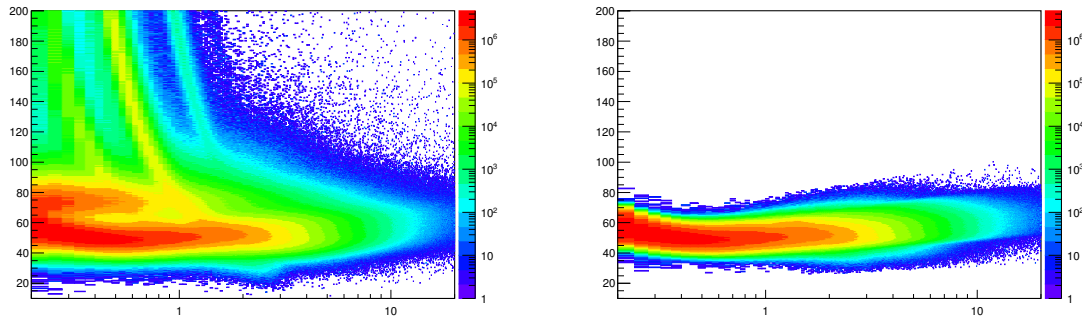


Figure 31: TPC dE/dx as function of transverse momentum for total (top) and selected second emitted π in 3σ (bottom)

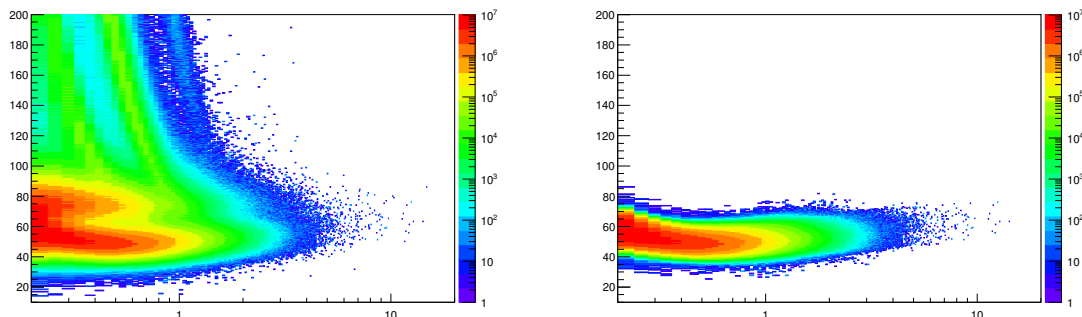


Figure 32: TPC dE/dx as function of transverse momentum for total (top) and selected last emitted π in 3σ (bottom)

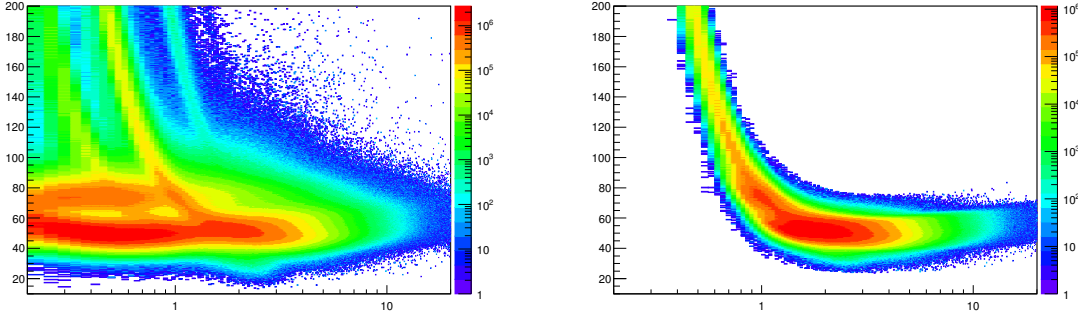


Figure 33: TPC dE/dx as function of transverse momentum for total (top) and selected proton in 3σ (bottom)

1093 5.1.4 Signal extraction

1094 The Ξ^{*0} signals were reconstructed by invariant-mass analysis of candidates for the decay
 1095 products in each transverse momentum interval of the resonance particle, and for each
 1096 multiplicity class. The $\Xi^-\pi^+(\Xi^+\pi^-)$ invariant mass distribution is reported in Figure 5.1.4
 1097 for semi-central events (20-40%) in p–Pb collisions and Figure 5.1.4 for central events(0-
 1098 10%) in Pb–Pb collisions.

1099 Since the resonance decay products originate from a position which is indistinguishable
 1100 from the PV, a significant combinatorial background is present. In order to extract
 1101 $\Xi(1530)^0$ signal it is necessary to remove or, at least reduce, the combinatorial background.
 1102 For this analysis, this has been done with the event mixing (EM) technique, by combining
 1103 uncorrelated decay products 20 different events in p–Pb (5 different events in Pb–Pb). The
 1104 events for the mixing have been selected by applying the similarity criteria to minimise
 1105 distortions due to different acceptances and to ensure a similar event structure, only tracks
 1106 from events with similar vertex positions z ($|\Delta z| < 1$ cm) and track multiplicities n ($|\Delta n| <$
 1107 10) were taken.

1108 The mixed-event background distributions were normalised to two fixed regions,
 1109 $1.49 < M_{\Xi\pi} < 1.51 \text{ GeV}/c^2$ and $1.56 < M_{\Xi\pi} < 1.58 \text{ GeV}/c^2$, around the Ξ^{*0} mass
 1110 peak (Figure 5.1.4 and 5.1.4). These regions were used for all p_T intervals and multiplicity
 1111 classes, because the background shape is reasonably well reproduced in these regions and
 1112 the invariant-mass resolution of the reconstructed peaks appears stable, independently of
 1113 p_T . The uncertainty on the normalisation was estimated by varying the normalisation
 1114 regions and is included in the quoted systematic uncertainty for the signal extraction (Section 5.4).

1116 After the background subtraction, the resulting distribution is shown in Figure 5.1.4
 1117 and 5.1.4. In order to obtain raw yields, a combined fit of a first-order polynomial for

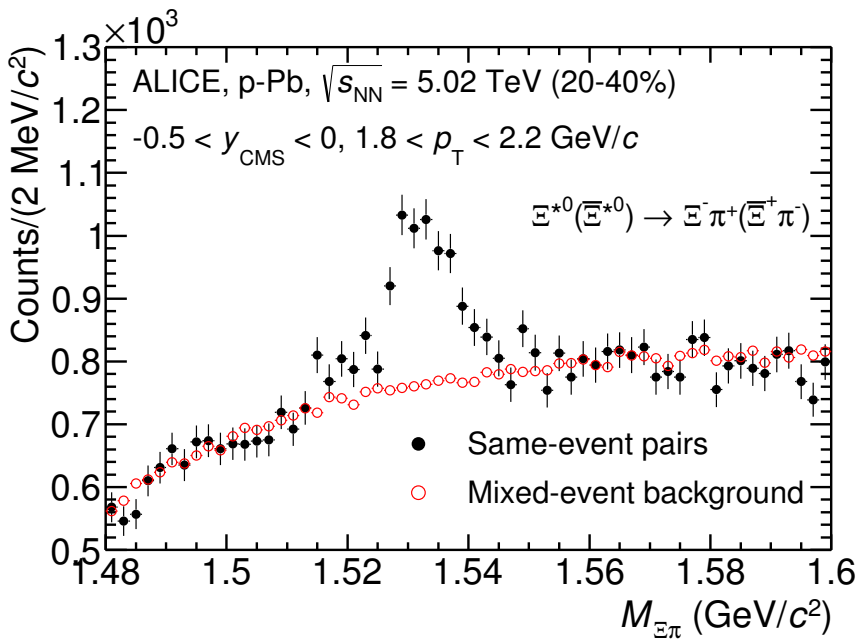


Figure 34: The $\Xi^\pm\pi^\pm$ invariant mass distribution (Same-event pairs) in $1.8 < p_T < 2.2 \text{ GeV}/c$ and for the multiplicity class 20-40%. The background shape, using pairs from different events (Mixed-event background), is normalised to the counts in $1.49 < M_{\Xi\pi} < 1.51 \text{ GeV}/c^2$ and $1.56 < M_{\Xi\pi} < 1.58 \text{ GeV}/c^2$.

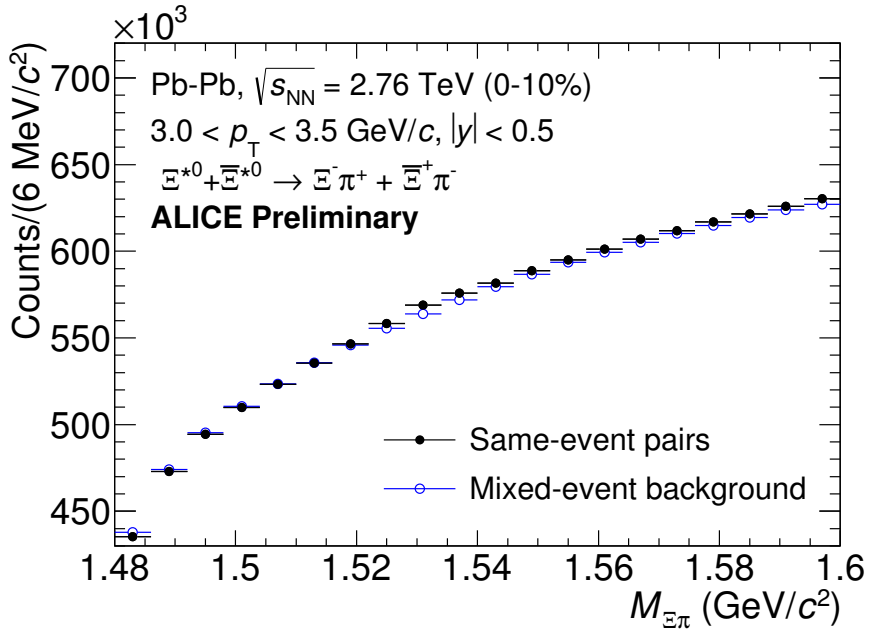


Figure 35: The $\Xi^\pm\pi^\pm$ invariant mass distribution (Same-event pairs) in $3.0 < p_T < 3.5$ GeV/c and for the centrality class 0-10%. The background shape, using pairs from different events (Mixed-event background), is normalised to the counts in $1.49 < M_{\Xi\pi} < 1.51$ GeV/c² and $1.56 < M_{\Xi\pi} < 1.58$ GeV/c².

the residual background and a Voigtian function (a convolution of a Breit-Wigner and a Gaussian function accounting for the detector resolution) for the signal was used. The mathematical form of fit function used in analysis is:

$$f(M_{\Xi\pi}) = \frac{Y}{2\pi} \frac{\Gamma_0}{(M_{\Xi\pi} - M_0)^2 + \frac{\Gamma_0^2}{4}} \frac{e^{-(M_{\Xi\pi} - M_0)/2\sigma^2}}{\sigma\sqrt{2\pi}} + bg(M_{\Xi\pi}) \quad (7)$$

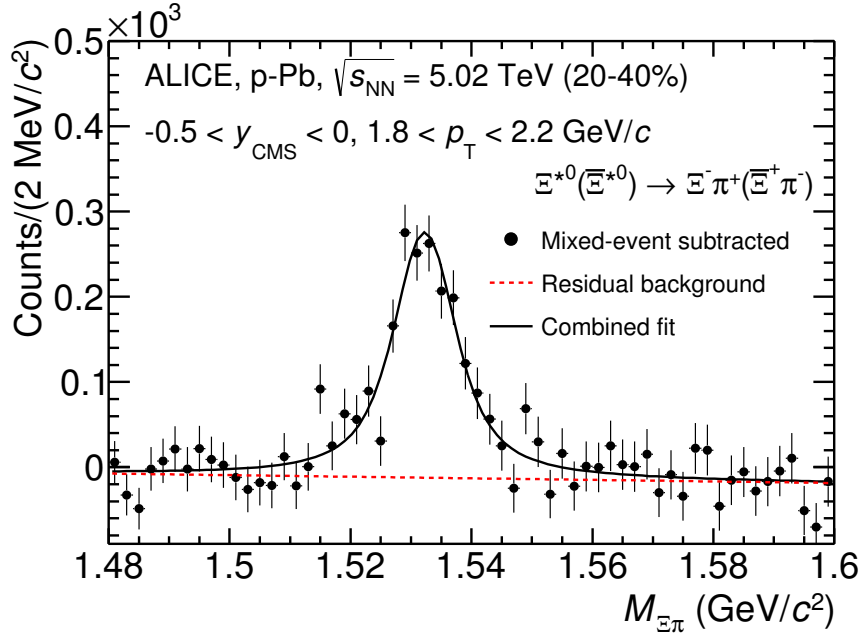


Figure 36: The invariant mass distribution after subtraction of the mixed-event background in p–Pb collisions. The solid curve represents the combined fit, while the dashed line describes the residual background.

The mass parameter of the Voigtian fit (M_0) is left free within the fit range ($1.48 \text{ GeV}/c^2$ and $1.59 \text{ GeV}/c^2$). The overall invariant mass width of the Voigtian function is governed by 2 parameters: σ and Γ_0 . The σ describes the broadening of the peak due to finite detector resolution while Γ describes the intrinsic width of the resonance itself. The Γ_0 is fixed to the PDG value of $9.1 \text{ MeV}/c$ for the $\Xi(1530)^0$. Because of lack of statistics, the σ can be over estimated. Therefore the σ parameter is fixed to value derived from σ in MB events which has largest statistics. The σ as function of p_T distribution in MB events is shown in Figure. 38 and we also report invariant mass of $\Xi(1530)^0$ as function of p_T in Figure. 39. The $\Xi(1530)^0$ raw yields have been extracted from the fit for the 4 multiplicity

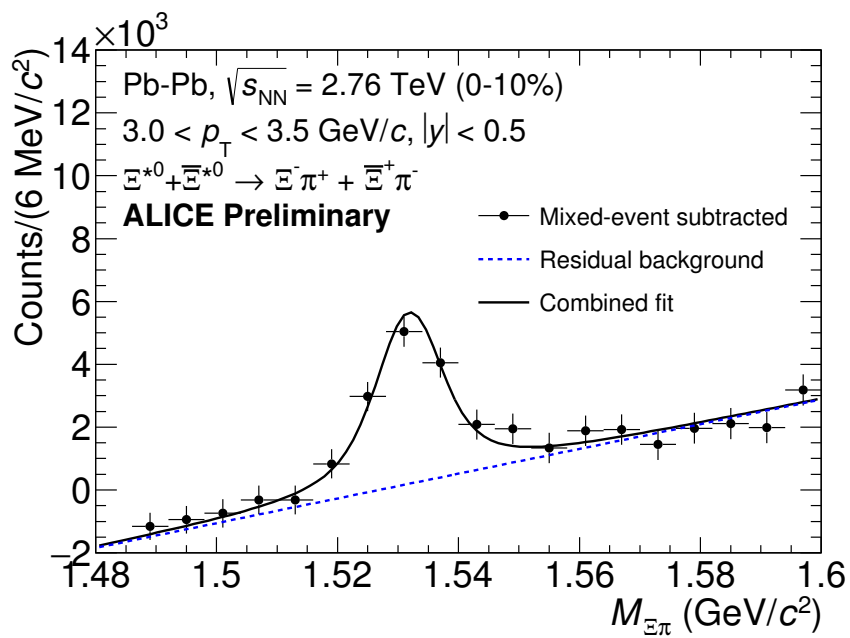


Figure 37: The invariant mass distribution after subtraction of the mixed-event background in Pb–Pb collisions. The solid curve represents the combined fit, while the dashed line describes the residual background.

₁₁₃₀ bins (+ NSD events) in p–Pb and 4 centrality bins in Pb–Pb collisions and the yields as
₁₁₃₁ function of p_T are shown in Figure 40.

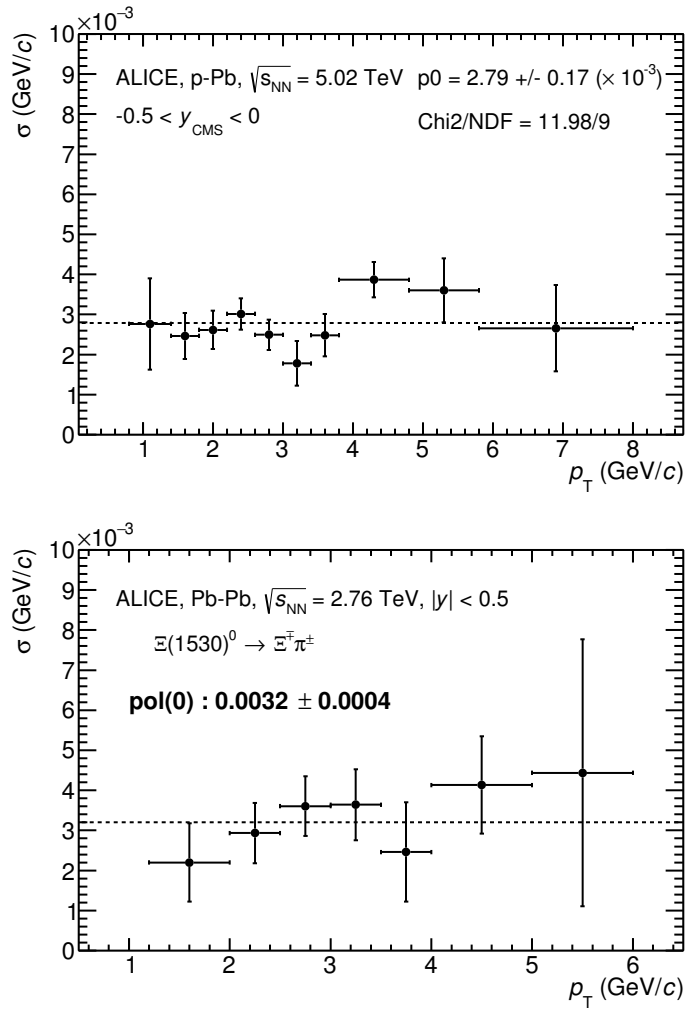


Figure 38: σ fit parameters as a function of p_T in MB in p–Pb collisions (top) and in Pb–Pb collisions (bottom).

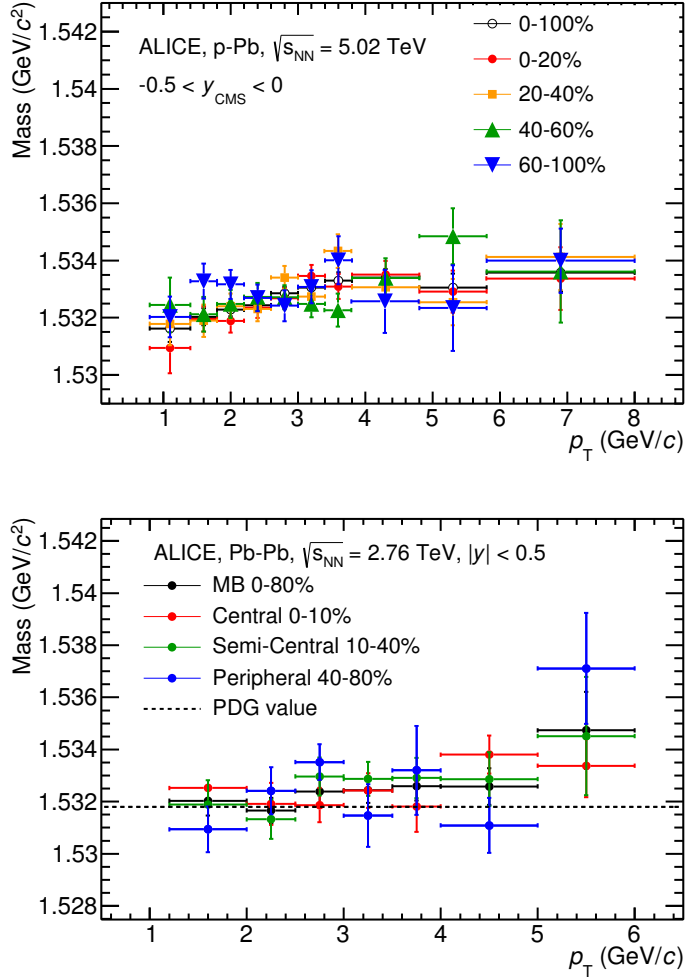


Figure 39: $\Xi(1530)^0$ -mass obtained from fit of the Voigtian peak as a function of p_T in each multiplicity classes in p-Pb collisions (top) and the different centrality classes in Pb-Pb (bottom).

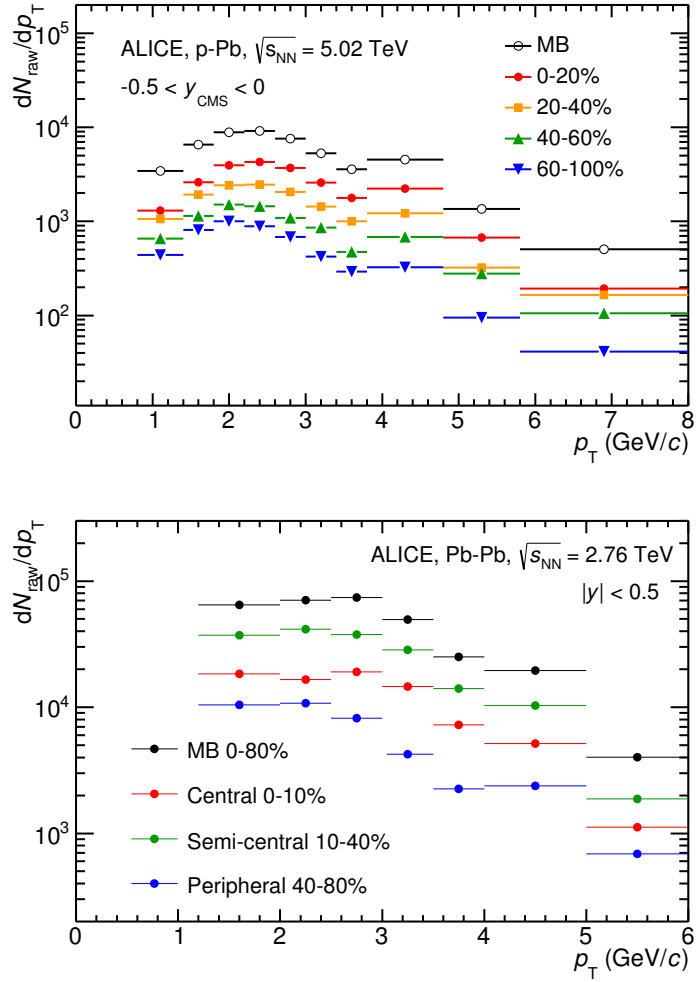


Figure 40: $\Xi(1530)^0$ -raw spectra obtained from fit of the Voigtian peak and a polynomial residual background for different multiplicities in p-Pb collisions (top) and Pb-Pb collisions (bottom). Only the statistical error is reported.

1132 **5.2 Efficiency correction**

1133 The raw yields were corrected for the geometrical acceptance and the reconstruction effi-
 1134 ciency ($A \times \epsilon$) of the detector (Figure. 41). By using the DPMJET 3.05 event generator [48]
 1135 and the GEANT 3.21 package [49], a sample of about 100 million p–Pb events was sim-
 1136 ulated and reconstructed in order to compute the corrections. The distributions of $A \times \epsilon$
 1137 were obtained from the ratio between the number of reconstructed Ξ^{*0} and the number of
 1138 generated particle in the same p_T and rapidity interval. Since the correction factors for
 1139 different multiplicity classes are in agreement with those from MB events within statistical
 1140 uncertainty, the latter were used for all multiplicity classes.

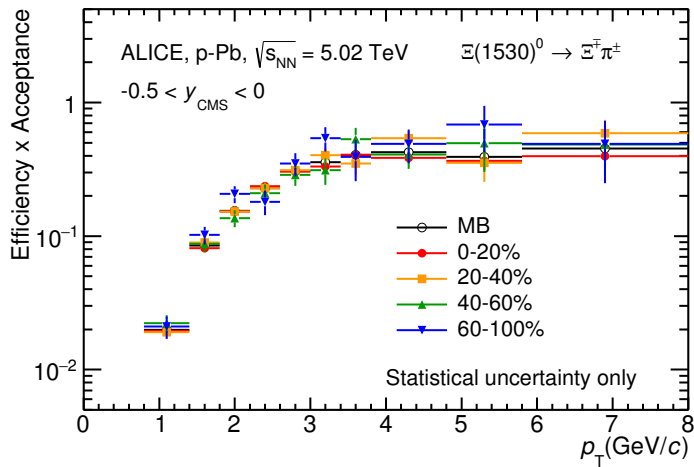


Figure 41: $\Xi(1530)^0$ -raw spectra obtained from fit of the Voigtian peak and a polynomial residual background for different multiplicities. Only the statistical error is reported.

1141 Because the generated $\Xi(1530)^0$ spectra have different shapes than the measured $\Xi(1530)^0$
 1142 spectra, it is necessary to weight the generated and reconstructed $\Xi(1530)^0$ spectra in these
 1143 simulations. Fig. 42 shows the generated and reconstructed $\Xi(1530)^0$ spectra plotted with
 1144 the (corrected) measured $\Xi(1530)^0$ spectrum for MB events and the Levy fit of that mea-
 1145 sured spectrum. The generated and measured $\Xi(1530)^0$ spectra have different behaviours
 1146 for the range $0.5 < p_T < 1$ GeV/ c . The generated $\Xi(1530)^0$ spectrum decreases with
 1147 increasing p_T over this range, while the fit of the measured $\Xi(1530)^0$ spectrum reaches a
 1148 local maximum in this range. The correction ϵ is observed to change rapidly over this
 1149 p_T range. It is therefore necessary to weight the generated spectrum so that it has the
 1150 shape of the measured $\Xi(1530)^0$ spectrum (and to apply corresponding weights to the re-
 1151 constructed $\Xi(1530)^0$ spectrum). An iterative procedure is performed to determine the
 1152 correct weighting (and therefore the correct ϵ).

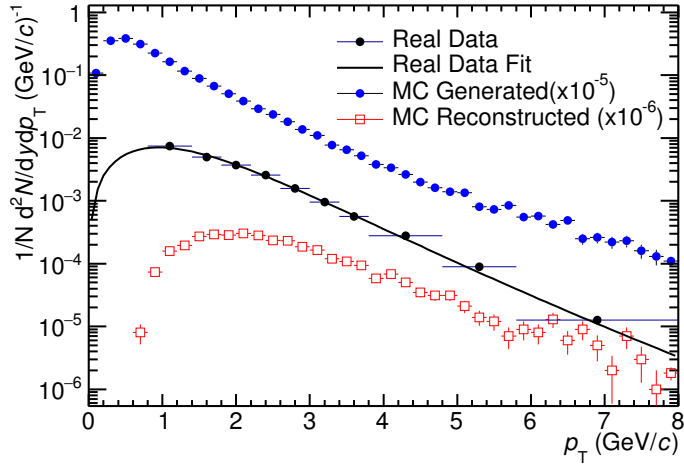


Figure 42: Real corrected $\Xi(1530)^0$ spectrum (black) for the minimum bias with Levy fit (black curve). Also shown are the unweighted generated (blue) and reconstructed (red) $\Xi(1530)^0$ spectra.

- 1153 1. The unweighted ϵ is calculated.
- 1154 2. This ϵ is used to correct the measured xis spectrum.
- 1155 3. The corrected $\Xi(1530)^0$ spectrum is fit.
- 1156 4. This fit is used to weight the simulated xis spectra. A p_T dependent weight is applied
1157 to the generated xis spectrum so that it follows the fit. The same weight is applied
1158 to the reconstructed xis spectrum.
- 1159 5. The (weighted) ϵ is calculated.
- 1160 6. Steps 2-5 are repeated (with the weighted ϵ from step 5 used as the input for step 2)
1161 until the ϵ values are observed to change by < 0.1% (relative) between iterations. It
1162 is observed that four iterations are sufficient for this procedure to converge.

1163 Finally, the re-weighted efficiency is obtained and the distribution as function of p_T is
1164 shown in Figure 43.

1165 In order to obtain the correction factor dedicated in Pb-Pb collisions, MC events are
1166 generated using Heavy Ion Jet Interaction Generator (HIJING). The generated events are
1167 passed through a GEANT3 model of the ALICE experiment with a realistic description of
1168 the detector response. Because we have observed centrality dependent efficiency, the cen-
1169 trality dependent efficiencies have been applied to get corrected raw yield. The reweighting

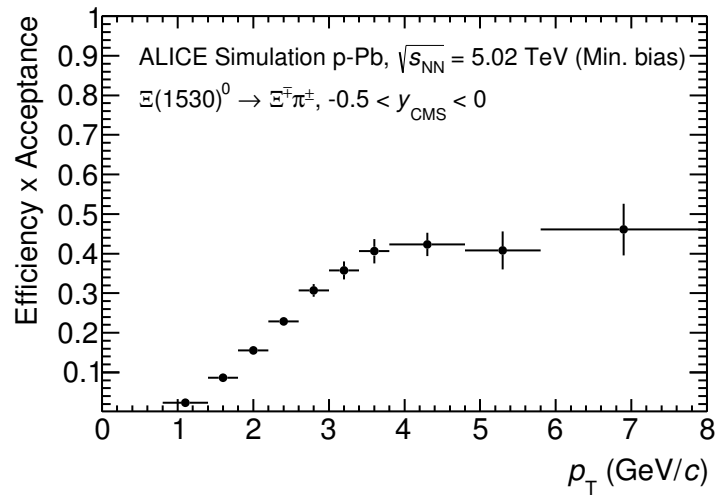


Figure 43: Efficiency as a function of p_T in minimum bias events in p–Pb collisions.

1170 approach which was used to correct the efficiency in p–Pb is also applied to the efficiency
 1171 obtained in Pb–Pb.

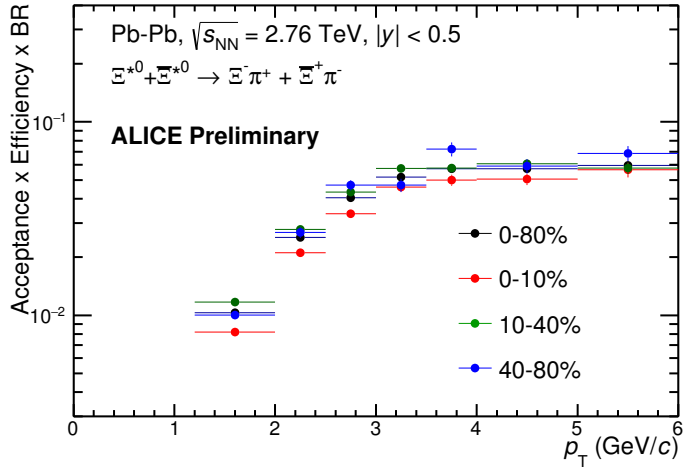


Figure 44: Efficiency as a function of p_T in different centrality classes in Pb–Pb collisions

1172 5.3 Corrected p_T -spectra

1173 The p_T spectrum is by the number of produced particles of a given type in the desired
 1174 interval of phase-space divided by the number of inelastic collisions. The spectrum is
 1175 calculated as:

$$\frac{1}{N} \times \frac{d^2N}{dydp_T} = \frac{1}{N_{E,PhysSel}} \times \frac{N_{raw}}{dp_T dy} \epsilon \frac{N_{total}^{MC}}{N_{post-PVcut}^{MC}}, \quad (8)$$

1176 where N_E represent the number inelastic collisions, the $\frac{dN}{dydp_T}$ is the yield per range of
 1177 rapidity y , per range in p_T . On the right hand side $N_{E,PhysSel}$ is the number of events
 1178 counted by the physics selection trigger. N_{raw} is the raw extracted number of particle in the
 1179 rapidity and p_T bin of width $\Delta y = 0.5$ in p–Pb ($\Delta y = 1.0$ in Pb–Pb) and Δp_T , respectively.
 1180 ϵ is the reconstruction efficiency estimated from Monte Carlo simulations. $\frac{N_{total}^{MC}}{N_{post-PVcut}^{MC}}$ is the
 1181 ratio of the total number of particle from MC divided by the number of particle from MC
 1182 after the Primary-Vertex cut is imposed. It takes into account the fraction of particle lost
 1183 after imposing the PV cut. We notice that for minimum-bias results in p–Pb, we adopted
 1184 a normalisation such that to provide result from non-single diffractive(NSD) cross-section.
 1185 The normalisation factor is 0.964 [6]. The obtained spectrum at MB and the spectrums
 1186 from different multiplicity classes in p–Pb are shown in Figure 45 and different centrality
 1187 classes in Pb–Pb are shown in Figure 46.

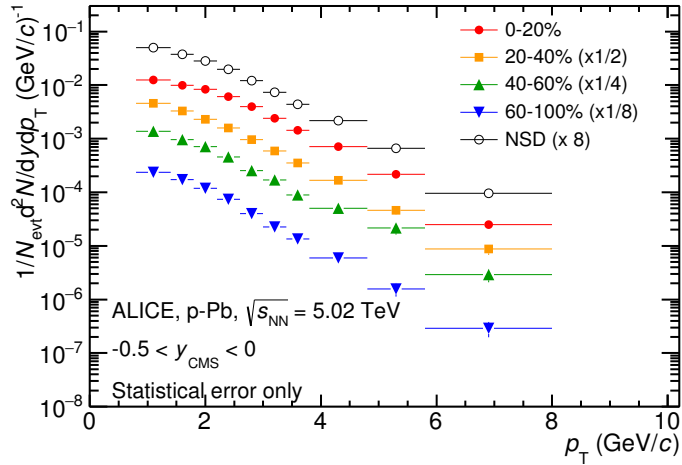


Figure 45: Corrected p_T -spectra of $\Xi(1530)^0$ in NSD and different multiplicity classes in p-Pb collisions.

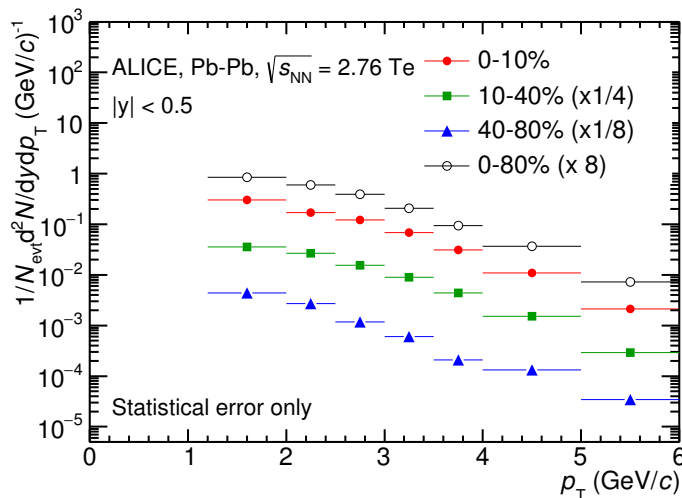


Figure 46: Corrected p_T -spectra of $\Xi(1530)^0$ in different centrality classes in Pb-Pb collisions.

1188 **5.4 Systematic uncertainties**

1189 The systematic uncertainties are calculated in seven principle groups. The procedure to ob-
1190 tain the systematic uncertainties is performed many times by varying the possible permuta-
1191 tion of the analysis parameter. The general strategy for evaluating systematic uncertainties
1192 is described as following:

- 1193 1. Choose one set of parameters for the analysis as default
- 1194 2. Observe the deviation of yield when one parameter is changed
- 1195 3. The systematic uncertainty is calculated for a given source as the RMS deviation of
1196 the available sources.
- 1197 4. The total systematic uncertainty, taking into account all the different sources, is the
1198 sum in quadrature of each source.

1199 To study the systematic effect we repeat the measurement by varying one parameter at
1200 a time. A Barlow [50] check has been performed for each measurement to verify whether it
1201 is due to a systematic effect or a statistical fluctuation. Let each measurement be indicated
1202 by $(y_i \pm \sigma_i)$ and the central value (default measurement) by $(y_c \pm \sigma_c)$, one can define $\Delta\sigma_i$
1203 (Eq. 9).

$$\Delta\sigma_i = \sqrt{(|\sigma_i^2 - \sigma_c^2|)} \quad (9)$$

1204 Then we calculate $n_i = \Delta y_i / \Delta\sigma_i$, where $\Delta y_i = |y_c - y_i|$. If $n_i \leq 1.0$ then the effects
1205 are due to the statistical fluctuation and if $n_i > 1.0$ we apply consistency check. Since
1206 the alternate and default measurements are not statistically independent, an alternate
1207 measurement which is statistically consistent with the default measurement should not be
1208 used in calculating a systematic uncertainty. The difference between the two measurements
1209 is $\Delta = y_c - y_i$. The difference in quadrature of the uncertainties is calculated by Eq. 9. It
1210 could be possible to check if $\Delta < \sigma$ and exclude such cases from the systematic uncertainties.
1211 However, there can be statistical fluctuations for which $\Delta > \sigma$. If the variations between the
1212 default and alternate measurements are purely statistical, the distribution of Δ/σ should
1213 be a Gaussian with a mean value that is consistent with zero and a deviation σ consistent
1214 with unity. In this analysis, if the mean value is less than 0.1 and σ is less than 1, the
1215 variation passes the consistency check.

1216 Only the measurements which passed the Barlow check ($n_i > 1$) are used to determine
1217 the systematic uncertainty. For measurements $N > 2$, the systematic uncertainty has been
1218 determined as the RMS (eqn. 10) of the available measurements. If $N=2$, the absolute
1219 difference is assigned as systematic uncertainty.

$$\delta y_{syst.} = \sqrt{\frac{1}{N} \sum_i (y_i - \bar{y})^2} \quad (10)$$

1220 Here N is the total number of available measurements including y_c and \bar{y} is the average
1221 of value of the measurements. The measurement did not pass Barlow check, zero systematic
1222 uncertainty has been assigned to the value.

1223 By suing the way as explained above, all the main contributions to the systematic un-
1224 certainty of particle spectra have been studied. In particular those that comes from signal
1225 extraction, topological and kinematical selection cuts, track quality selection and $n\sigma$ TPC
1226 PID variation. the meaning of each source of systematic uncertainty studied is described
1227 in the following:

1228

1229 **Signal extraction**

1230 We have extracted the signal with varying the yield calculating method which contains
1231 the method of signal extraction by integrating the Voigtian fit function and bin counting.
1232 We also have varied the normalisation range which is related to the invariant mass region
1233 where the mixed events distribution is scaled to subtract the combinatorial background
1234 and different background estimator such as Like-Sign distribution and polynomial fit was
1235 taken account into the systematic source of signal extraction. The systematic uncertainty
1236 from signal extraction is sum in quadrature of three sources.

1237

1238 **Topological selection**

1239 To evaluate the stability of the chosen set of values for the topological cuts, loose and tight
1240 cuts have beed defined in order to vary by $\pm 10\%$ respectively. The parameters are changed
1241 once at a time. Total systematic uncertainty from topological selection is calculated by
1242 summation in quadrature of nine sources.

1243

1244 **TPC $N_{cluster}$ selection**

1245 The selection performed for the daughter tracks of the cascade is that $N_{cluster}$ is larger
1246 than 70 and the value has been varied to 60 and 80 in order to estimate the systematic
1247 uncertainty due to this selection.

1248

1249 **TPC dE/dx selection**

1250 In order to evaluate any potential effect due to the TPC dE/dx selection (U_{PID}), the N_σ
1251 selection was varied with $N = 2.5$ and 3.5 .

1252

1253 **p_T shape correction**

1254 As described in Section 5.2, due to the different shape of the measured and generated
1255 $\Xi(1530)^0$ spectra, we have applied reweighing procedure to the generated spectra to have
1256 same shape and this correction is added into contributor of systematic uncertainty as
1257 p_T shape correction.

1258

1259 **Mass window range selection**

1260 In order to select Ξ^\pm which is daughter particle of $\Xi(1530)^0$, we apply the mass window

1261 ± 7 MeV/c² around $\Xi(1530)^0$ mass on $\Lambda\pi$ invariant mass distribution. The boundaries has
1262 been varied to ± 6 MeV/c² and ± 8 MeV/c² to estimate systematic uncertainty.

1263

1264 **Vertex range selection**

1265 The distribution of vertex-z is shown in Fig.22. The cut on |Vz| was varied from the nominal
1266 ± 10 cm to ± 9 cm, ± 11 cm.

1267

1268 **Material Budget and hadronic cross section**

1269 A possible source of uncertainty comes from the description of the material, active (detecting area)
1270 or dead (structure and cable), that the particles cross during their travel in
1271 the MC with respect to the real material present in the detector. Such description could
1272 affect the reconstruction efficiency in different aspects (e.g. multiple scattering, energy
1273 loss). The value estimated by Ξ analysis [24] has been used in this study which gives 4%
1274 systematic uncertainty. In case of systematic uncertainty from hadronic cross section, we
1275 have inherited the value studied in previous measurement[51] which amount is 1%.

1276

1277 **Tracking efficiency**

1278 Systematic uncertainties from tracking efficiency from ITS + TPC combined track were
1279 assigned as 3% in p–Pb and 4% in Pb–Pb collision system.[51]
1280 (<https://twiki.cern.ch/twiki/bin/view/ALICE/TrackingEfficiencyCharged>)

1281

1282 Finally, total systematic uncertainty is sum in quadrature of sources listed above. Figure
1283 47 and Figure 48 show the total systematic uncertainty in minimum bias event and
1284 different multiplicity classes in p–Pb collisions, respectively. Again, Figure 49 and Figure
1285 50 present the total systematic uncertainty in minimum bias event and different centrality
1286 classes in Pb–Pb collisions.

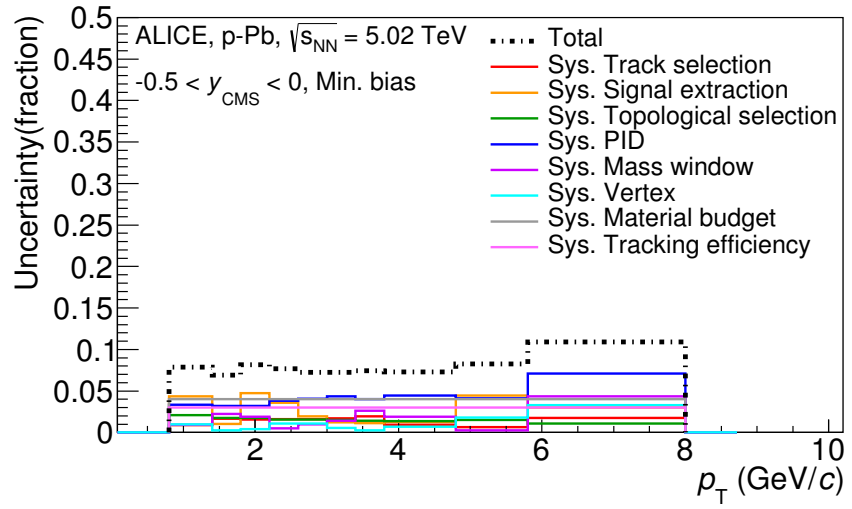


Figure 47: Summary of the contributions to the systematic uncertainty in minimum bias events in p–Pb collisions. The dashed black line is the sum in quadrature of all the contributions.

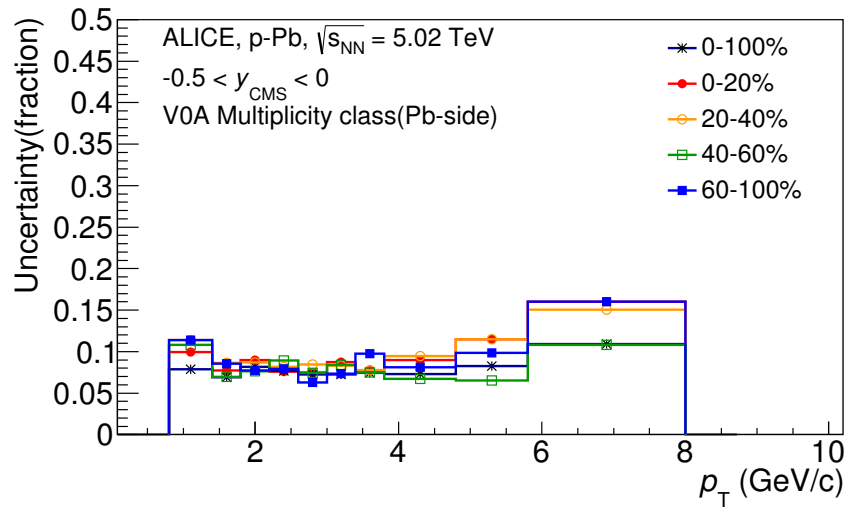


Figure 48: Systematic uncertainties for each multiplicity classes in p–Pb collisions.

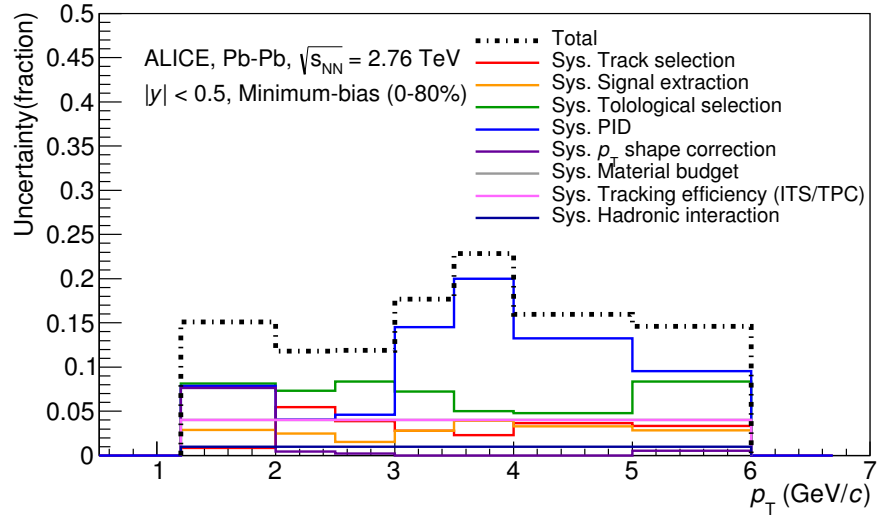


Figure 49: Summary of the contributions to the systematic uncertainty in minimum bias events in Pb–Pb collisions. The dashed black line is the sum in quadrature of all the contributions.

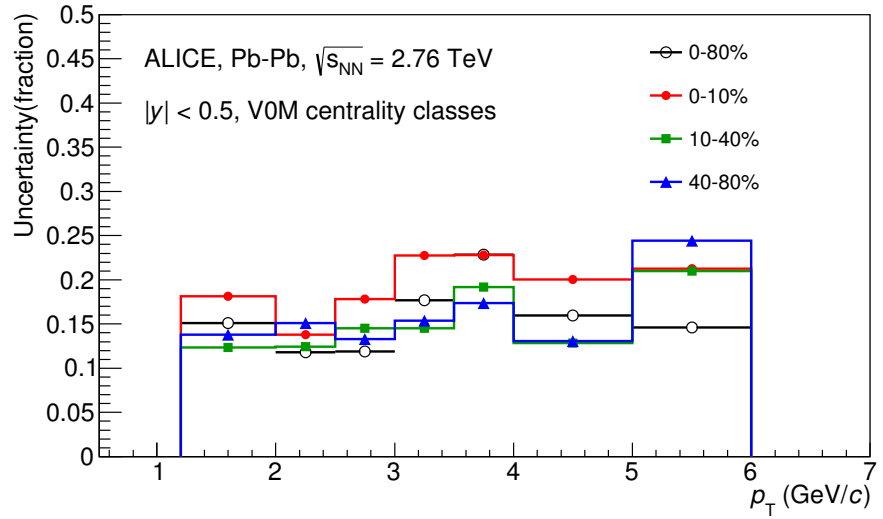


Figure 50: Systematic uncertainties for each multiplicity classes.

Source of uncertainty	p-Pb	Pb-Pb
<i>p</i> _T -dependent		
Tracking efficiency	3%	4%
Tracks selection	1-2%	1-5%
Topological selection	1-2%	5-8%
PID	3-7%	4-20%
Signal extraction	1-5%	1-4%
<i>p</i> _T shape correction	-	0-8%
Mass window (Ξ^\pm)	4%	-
Vertex selection	3%	-
<i>p</i> _T -independent		
Hadronic interaction	-	1%
Material budget	4%	4%
Branching ratio	0.3%	0.3%
Total	8-12%	9-25 %

Table 11: Summary of the systematic uncertainties on the differential yield, $d^2N/(dp_T dy)$. Minimum and maximum values in all p_T intervals and multiplicity classes in p–Pb, centrality classes in Pb–Pb are shown for each source.

1287 **5.5 $\Xi(1530)^0$ transverse momentum spectra**

1288 The raw yield shown in Figure 45 and 46 have been corrected for efficiency as described
 1289 in section 5.2. The measured spectra for $(\Xi(1530)^0 + \bar{\Xi}(1530)^0)/2$ are reported in Figure
 1290 51 for p–Pb collisions and Figure 52 for Pb–Pb collisions. The statistical and systematic
 1291 uncertainties are reported respectively as the error bars and the boxes on the plot. The
 1292 corrected yields for p–Pb collisions are measured with $0.8 < p_T < 8.0$ GeV/c while the
 1293 yields for Pb–Pb collisions are obtained with $1.2 < p_T < 6.0$ GeV/c due to difficulty of
 1294 signal extraction in low and high p_T region.

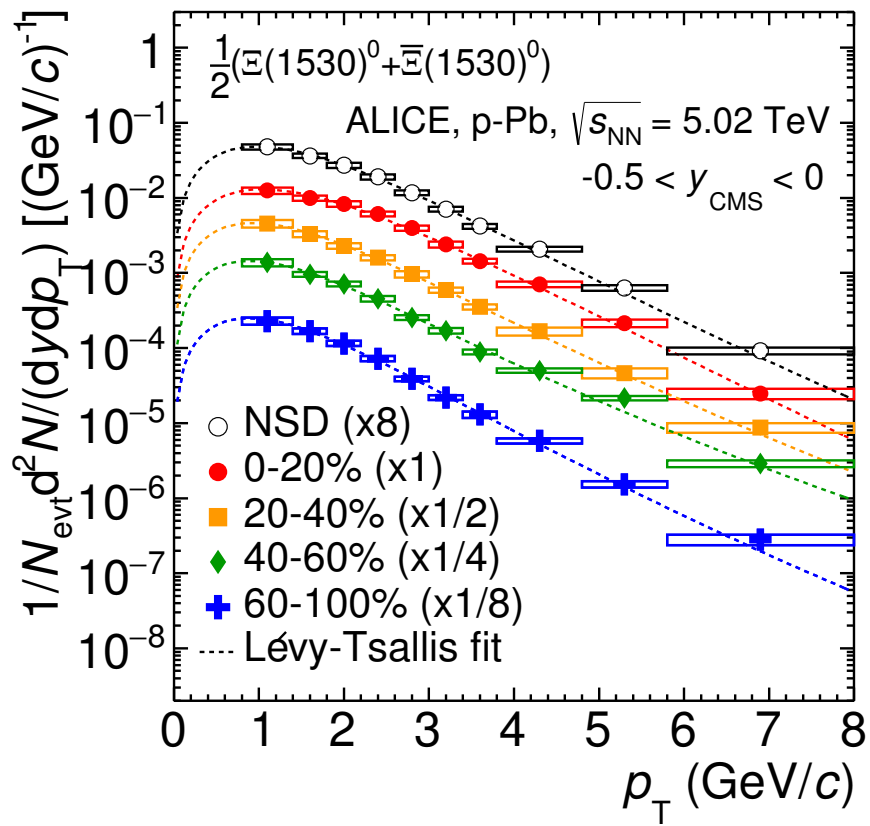


Figure 51: Corrected yields as function of p_T in NSD events and multiplicity dependent event classes in p-Pb collision system. Statistical uncertainties are presented as bar and systematical uncertainties are plotted as boxes.

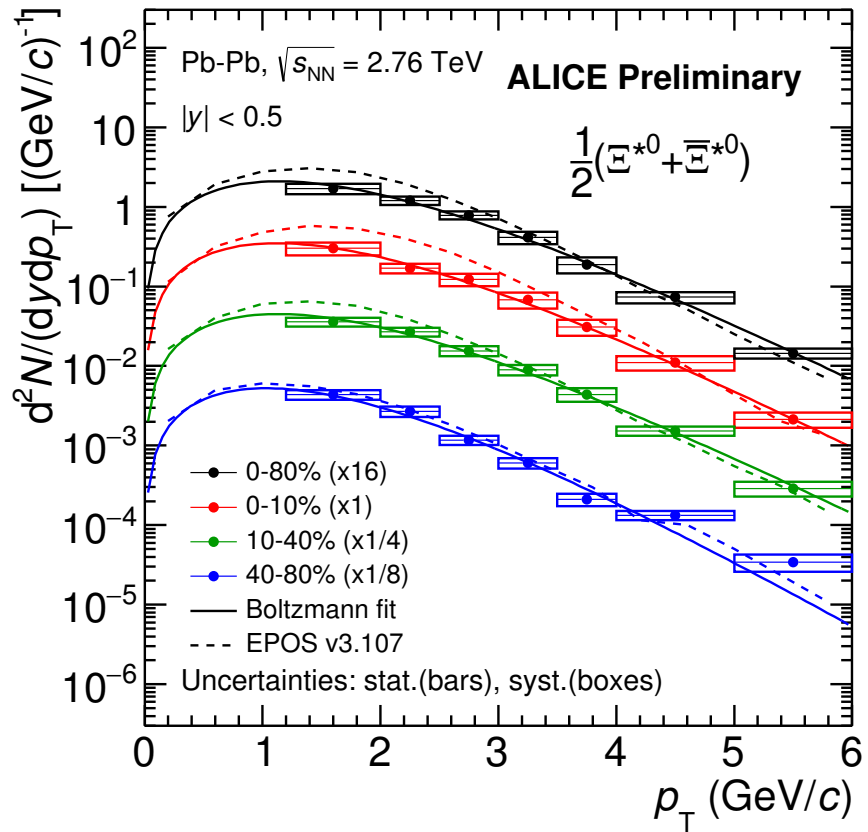


Figure 52: Corrected yields as function of p_T in different centrality classes in Pb–Pb collision system. Statistical uncertainties are presented as bar and systematical uncertainties are plotted as boxes.

1295 6 Further results and discussion

1296 The transverse momentum distributions of double-strange hyperon resonances, $\Xi(1530)^0$
1297 , produced in p–Pb collisions at $\sqrt{s_{\text{NN}}}= 5.02$ TeV and Pb–Pb collisions at $\sqrt{s_{\text{NN}}}= 2.76$
1298 TeV were measured in the mid-rapidity range and they have been already presented in
1299 Chapter 5. From the measurement, the $\langle p_{\text{T}} \rangle$ and integrated particle yield ratios with
1300 system size have been obtained. In the present Chapter these results are compared with
1301 model predictions and discussed in connection with the following topics:

- 1302 • Mean transverse momentum studies
1303 • Study of particle production mechanism in hadronic phase
1304 • Study of strangeness enhancement

1305 Most of the theoretical aspects related to these topics and, in particular, the description
1306 of the models already have been addressed in Chapter 2.

1307 6.1 Mean transverse momentum

1308 Figure 53 shows the mean transverse momentum $\langle p_{\text{T}} \rangle$ as a function of mean charged-
1309 particle multiplicity density $\langle dN_{\text{ch}}/d\eta_{\text{lab}} \rangle$ at midrapidity. The results for $\Xi(1530)^0$ are
1310 compared with those for other hyperons observed in p–Pb collisions at $\sqrt{s_{\text{NN}}}= 5.02$ TeV [5,
1311 7].

1312 Increasing trends from low to high multiplicities are observed for all hyperons. The
1313 mean transverse momenta increase by 20% as the mean charged-particle multiplicity in-
1314 creases from 7.1 to 35.6. This result is similar to the one obtained for the other hyperons.
1315 Furthermore, a similar increase has been observed also for K^{\pm} , K_S^0 , $K^*(892)^0$ and ϕ [6],
1316 whereas protons are subject to a larger ($\sim 33\%$) increase in the given multiplicity range,
1317 as discussed also in Ref. [5].

1318 In all multiplicity classes, the $\langle p_{\text{T}} \rangle$ follows an approximate mass ordering:

- 1319 • $\langle p_{\text{T}} \rangle_{\Lambda} < \langle p_{\text{T}} \rangle_{\Xi^-} \simeq \langle p_{\text{T}} \rangle_{\Sigma^{*\pm}} < \langle p_{\text{T}} \rangle_{\Xi^{*0}} < \langle p_{\text{T}} \rangle_{\Omega^-}$

1320 The $\langle p_{\text{T}} \rangle$ of $\Sigma^{*\pm}$ looks systematically lower than the $\langle p_{\text{T}} \rangle$ of Ξ^- , despite the larger mass
1321 of $\Sigma^{*\pm}$. The uncertainties, however, are too large to draw any conclusion on possible hints
1322 of violation of the mass hierarchy. This hierarchy of mass-ordering, also including D^0 and
1323 J/ψ in the comparison, is displayed in Figure 54. Note, however, that the D^0 and J/ψ
1324 were measured in different rapidity ranges: $|y_{\text{CMS}}| < 0.5$ [9] ($|y_{\text{CMS}}| < 0.9$ [10]) for D^0
1325 (J/ψ) in pp and $-0.96 < y_{\text{CMS}} < 0.04$ [9] ($-1.37 < y_{\text{CMS}} < 0.43$ [11]) for D^0 (J/ψ) in
1326 p–Pb, and the results for D^0 and J/ψ in p–Pb collisions are for the 0–100% multiplicity
1327 class. This mass dependence is observed in both p–Pb and pp collisions. It was observed
1328 also by the STAR collaboration [52] in MB pp, MB d–Au and central Au–Au collisions.

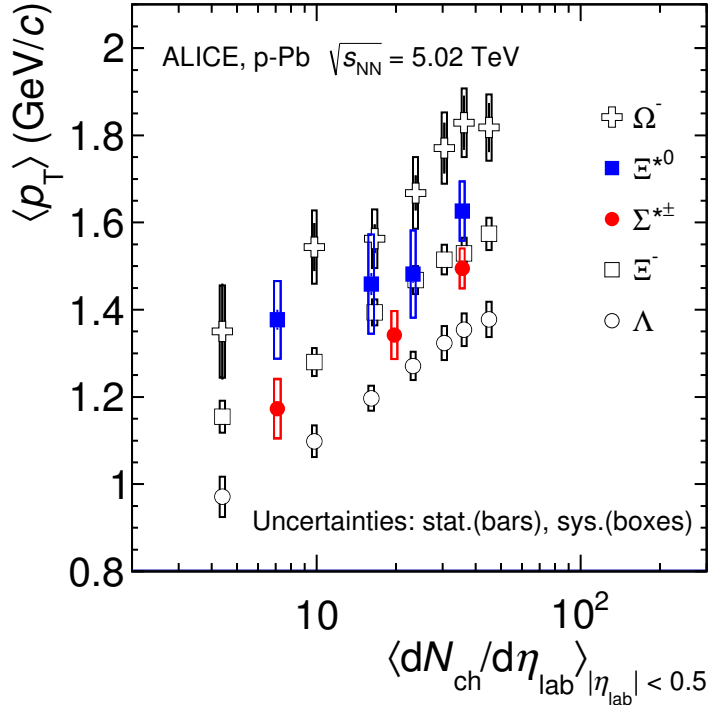


Figure 53: Mean transverse momenta $\langle p_T \rangle$ of Λ , Ξ^- , $\Sigma^{*\pm}$, Ξ^{*0} and Ω^- in p–Pb collisions at $\sqrt{s_{NN}}=5.02$ TeV as a function of mean charged-particle multiplicity density $\langle dN_{ch}/d\eta_{lab} \rangle$, measured in the pseudorapidity range $|\eta_{lab}| < 0.5$. The results for Λ , Ξ^- and Ω^- are taken from [5, 6, 7]. Statistical and systematic uncertainties are represented as bars and boxes, respectively. The Ω^- and Ξ^- points in the 3rd and 4th lowest multiplicity bins are slightly displaced along the abscissa to avoid superposition with the $\Xi(1530)^0$ points.

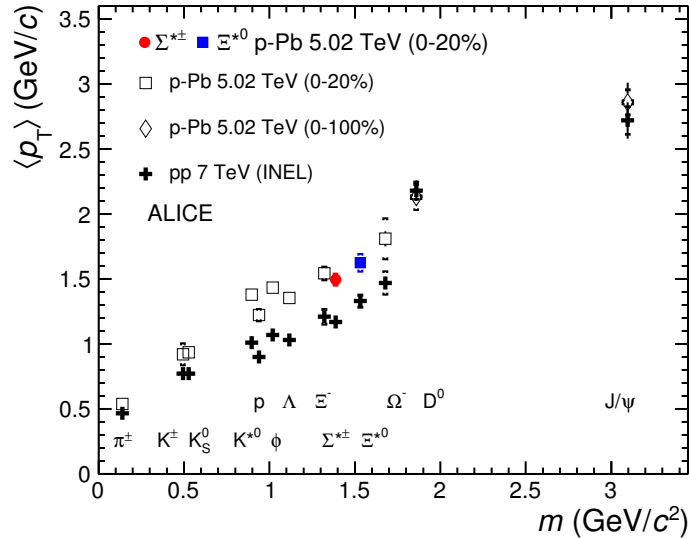


Figure 54: Mass dependence of the mean transverse momenta of identified particles for the 0 – 20% V0A multiplicity class and with $-0.5 < |y_{\text{CMS}}| < 0$ in p–Pb collisions at $\sqrt{s_{\text{NN}}} = 5.02$ TeV [5, 7], and in minimum-bias pp collisions at $\sqrt{s} = 7$ TeV [8] with $|y_{\text{CMS}}| < 0.5$. Additionally, D^0 and J/ψ results are plotted. The D^0 and J/ψ were measured in different rapidity ranges: $|y_{\text{CMS}}| < 0.5$ [9] ($|y_{\text{CMS}}| < 0.9$ [10]) for D^0 (J/ψ) in pp and $-0.96 < y_{\text{CMS}} < 0.04$ [9] ($-1.37 < y_{\text{CMS}} < 0.43$ [11]) for D^0 (J/ψ) in p–Pb. Note also that the results for D^0 and J/ψ in p–Pb collisions are for the 0–100% multiplicity class.

1329 Furthermore, for the light-flavour hadrons, the mean transverse momenta in p–Pb col-
1330 lisions are observed to be consistently higher than those in pp collisions at 7 TeV. The
1331 situation for the charm hadrons is different, where $\langle p_T \rangle$ appears compatible between both
1332 colliding systems. The discrepancy is likely due to different production mechanisms for
1333 heavy and light flavours and to a harder fragmentation of charm quarks. Specifically, the
1334 fact that $\langle p_T \rangle$ remains similar in pp and in p–Pb is consistent with an $R_{p\text{Pb}}$ ratio com-
1335 patible with unity at all p_T [9] for D^0 , and/or with the effects of shadowing in p–Pb which
1336 reduces the production at low p_T and thus increasing the overall $\langle p_T \rangle$ for J/ψ [11]; the
1337 small p_T hardening expected in pp when going from 5.02 to 7TeV is apparently not enough
1338 to counter-balance the situation.

1339 Because of small decrease of the $\langle p_T \rangle$ for proton and Λ relative to those for K^{*0} and
1340 ϕ , two different trends for mesons and baryons have been suggested [53]. Even including
1341 D^0 and J/ψ , as shown in Figure 54, a different trend for mesons and baryons cannot be
1342 convincingly established.

1343 **6.2 Particle yield ratios**

1344 **6.2.1 Integrated yield ratios of excited to ground-state hadrons**

1345 The integrated yield ratios of excited to ground-state hyperons [54, 5, 8, 7] with the same
1346 strangeness content, for different collision systems and energies, are shown in Figure 55
1347 as a function of system size. The ratio of $\Xi(1530)^0$ to Ξ is flat across the system and
1348 it complements the information derived from other resonance measurement for different
1349 lifetime which are shown in Figure 56.

1350 The short-lived resonances(ρ , K^* and Λ^*) which exhibit suppression from peripheral to
1351 central lead-lead collisions and with respect to thermal model in central lead-lead collisions.
1352 Currently favored explanation of is dominance of elastic re-scattering of decay daughters
1353 over regeneration in the hadronic phase.

1354 The constant behavior of the yield ratios of excited to ground-state hyperons with same
1355 strangeness content ($\Xi(1530)^0$ and Φ) indicates that neither regeneration nor re-scattering
1356 dominates with increasing collision system size because of its longer-lifetime.

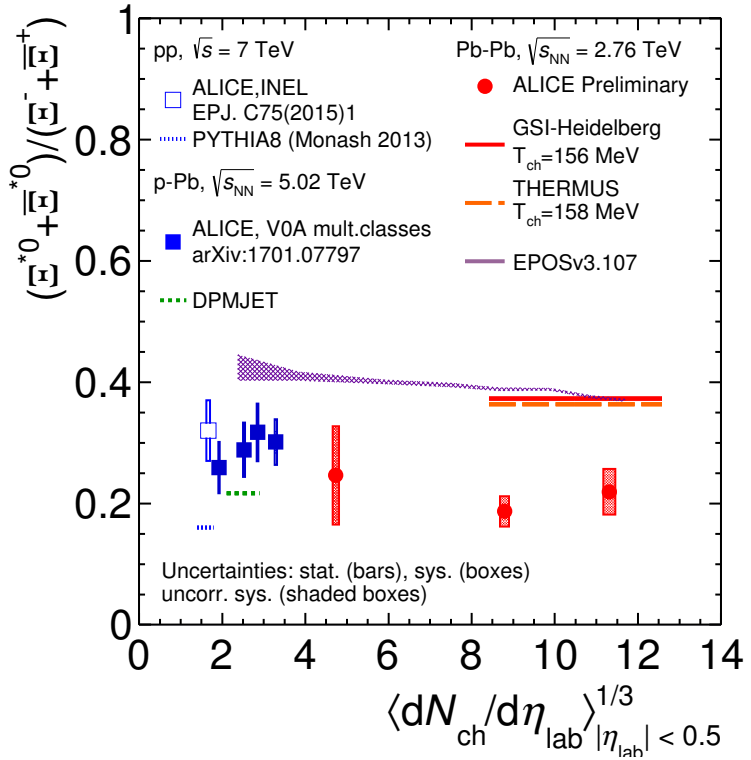


Figure 55: Ratio of $\Xi(1530)^0$ to Ξ^- measured in pp [8], p–Pb [5, 7] and Pb–Pb collisions as a function of $\langle dN_{ch}/d\eta_{lab} \rangle$ measured at midrapidity. Statistical uncertainties (bars) are shown as well as total systematic uncertainties (hollow boxes) and systematic uncertainties uncorrelated across multiplicity (shaded boxes). A few model predictions are also shown as lines at their appropriate abscissa.

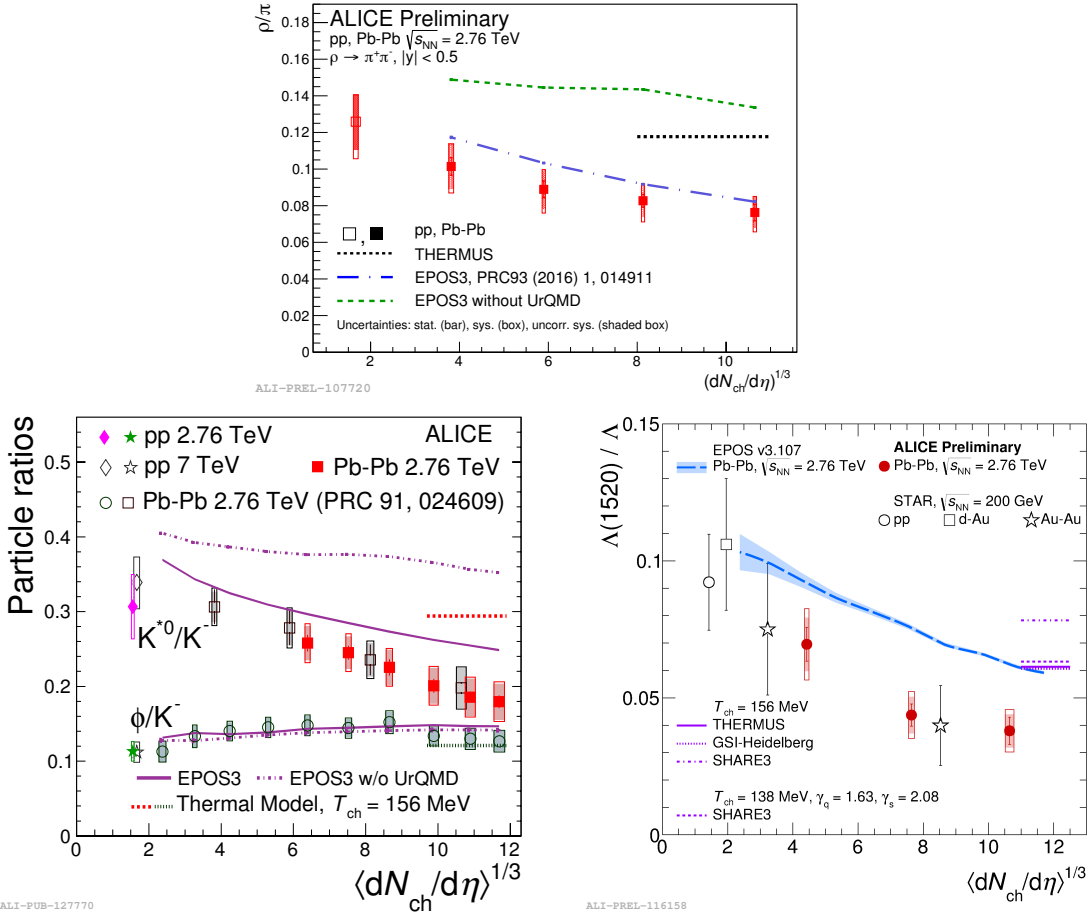


Figure 56: Ratio of ρ/π (Up), K^*/K , ϕ/K (Left bottom) and Λ^*/Λ with system size measured at mid-rapidity. Statistical uncertainties (bars) are shown as well as total systematic uncertainties (hollow boxes) and systematic uncertainties uncorrelated across multiplicity (shaded boxes). A few model predictions are also shown as lines at their appropriate abscissa.

1357 **6.3 Integrated yield ratios to pion**

1358 The integrated yield ratios of excited hyperons to pions are shown in Figure 57 to study
1359 the evolution of relative strangeness production yields with increasing collision system
1360 size. The ratio of $\Xi(1530)^0$ to Ξ is observed to be increase from pp to p–Pb collisions
1361 system and then, decrease from peripheral to central Pb–Pb collision. The QCD-inspired
1362 predictions like PYTHIA for pp [55] and DPMJET for p–Pb [48] clearly underestimate
1363 the observed yield ratios, while the statistical one seems to be comparable with results
1364 from high multiplicity in p–Pb but the ratio in Pb–Pb is below with respect to the model.
1365 The results in pp and p–Pb collisions are consistent with previous observation of ground-
1366 state hyperons to pion ratios. The Figure 58 presents particle yield ratios to pions of
1367 strange and multi-strange hadrons normalized to the values measured in pp collisions. As
1368 shown in the Figure 58, the $\Xi(1530)^0$ to pion ratios follow the trend of $\Xi \pi$ as function of
1369 $\langle dN_{ch}/d\eta_{lab} \rangle$ and indicate that the strangeness enhancement observed in p–Pb collisions
1370 depends predominantly on the strangeness content, rather than on the hyperon mass.

1371 The Figure 59 also shows the hyperon-to-pion ratios and compared with model predic-
1372 tions. The

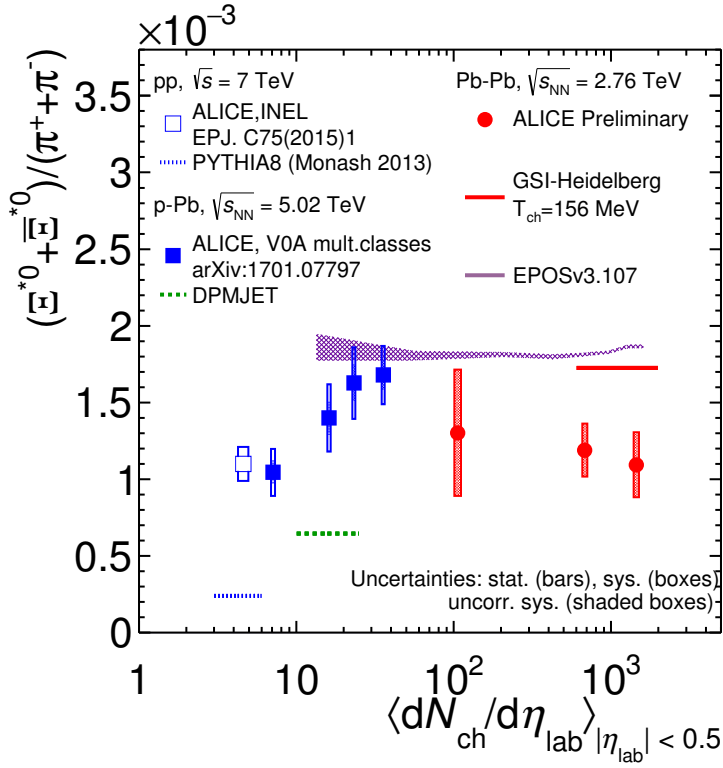


Figure 57: Ratio of $\Xi(1530)^0$ to π^\pm , measured in pp [12] and p–Pb [8] collisions, as a function of the average charged particle density ($\langle dN_{ch}/d\eta_{lab} \rangle$) measured at mid-rapidity. Statistical uncertainties (bars) are shown as well as total systematic uncertainties (hollow boxes) and systematic uncertainties uncorrelated across multiplicity (shaded boxes). A few model predictions are also shown as lines at their appropriate abscissa.

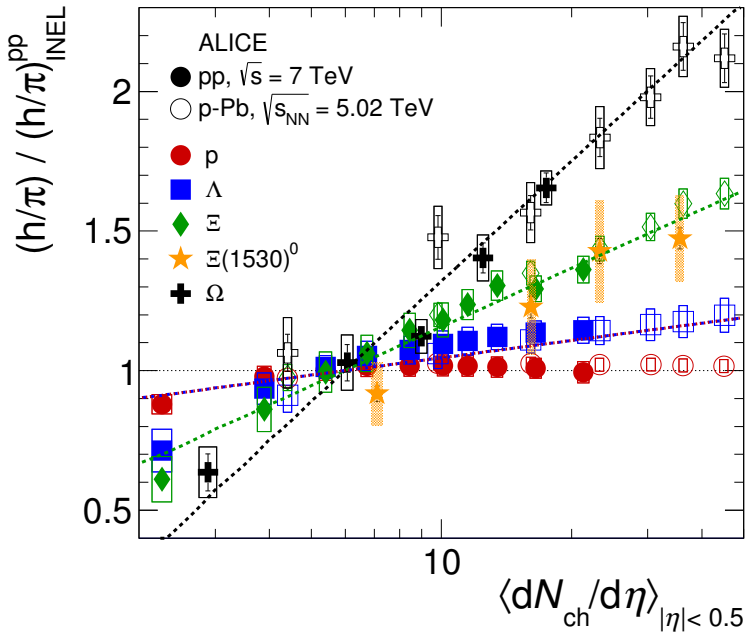


Figure 58: Particle yield ratios to pions of strange and multi-strange hadrons normalized to the values measured in pp collisions, both in pp and in p–Pb collisions. The common systematic uncertainties cancel in the double-ratio. The empty boxes represent the remaining uncorrelated uncertainties. The lines represent a simultaneous fit of the results with the empirical scaling formula in Equation ??.

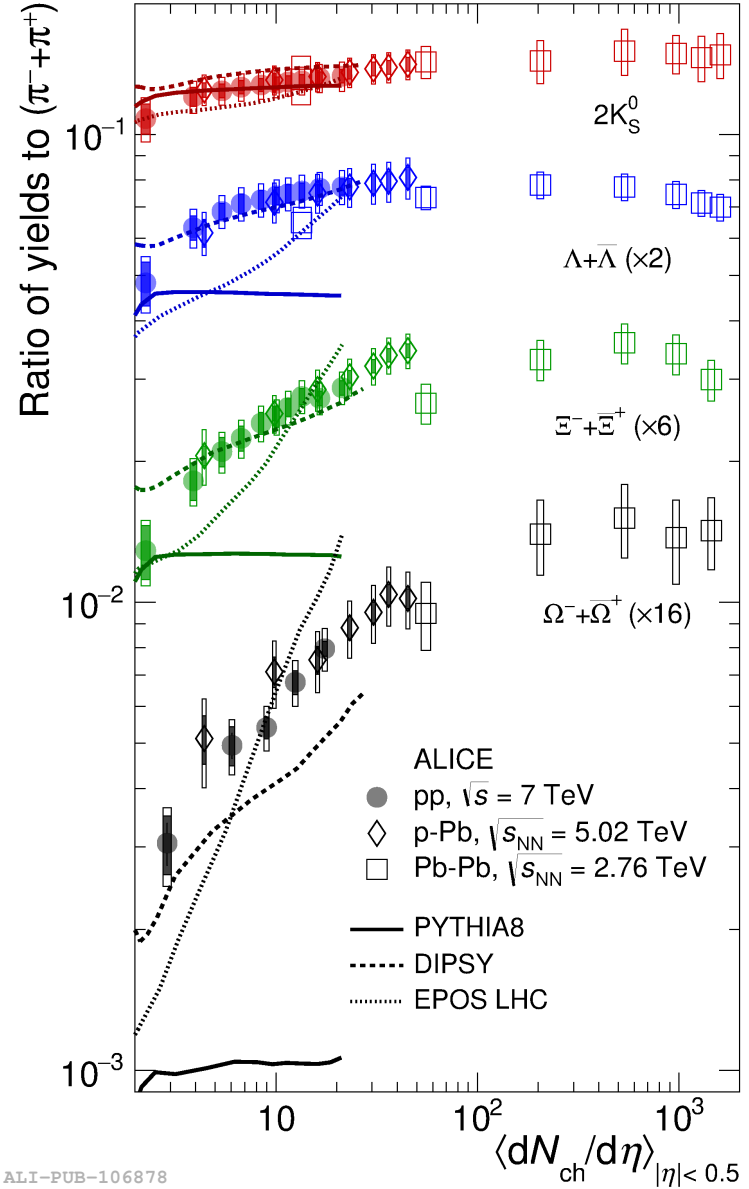


Figure 59: p_T -integrated yield ratios of strange and multi-strange hadrons to $(\pi^+ + \pi^-)$ as a function of $\langle dN_{ch}/d\eta_{lab} \rangle$ measured in the rapidity interval $|\eta| < 0.5$. The empty and dark-shaded boxes show the total systematic uncertainty and the contribution uncorrelated across multiplicity bins, respectively. The values are compared to calculations from MC models and to results obtained in Pb–Pb and p–Pb collisions at the LHC.

1373 **References**

- 1374 [1] **Particle Data Group** Collaboration, K. Olive *et al.*, “Review of Particle Physics,”
1375 *Chin. Phys. C* **38** (2014) 090001.
- 1376 [2] K. R. Ahmed Tounsi, “Strangeness Enhancement and Canonical Suppression,” *High*
1377 *Energy Physis A* **681** (2001) 119–123.
- 1378 [3] “TE-EPC-LPC LHC units,”.
1379 <http://te-epc-lpc.web.cern.ch/te-epc-lpc/machines/lhc/general.stm>.
- 1380 [4] **ALICE** Collaboration, K. e. a. Aamodt, “Alignment of the ALICE Inner Tracking
1381 System with cosmic-ray tracks,” *JINST* **5** (2010) P03003.
- 1382 [5] **ALICE** Collaboration, J. Adam *et al.*, “Multiplicity dependence of pion, kaon,
1383 proton and lambda production in p–Pb collisions at $\sqrt{s_{NN}} = 5.02$ TeV,” *Phys. Lett.*
1384 **B728** (2014) 25–38, [arXiv:1307.6796 \[nucl-ex\]](https://arxiv.org/abs/1307.6796).
- 1385 [6] **ALICE** Collaboration, J. Adam *et al.*, “Production of $K^*(892)^0$ and $\phi(1020)$ in
1386 p–Pb collisions at $\sqrt{s_{NN}} = 5.02$ TeV,” *Eur. Phys. J.* **C76** (2016) 245,
1387 [arXiv:1601.7868 \[nucl-ex\]](https://arxiv.org/abs/1601.7868).
- 1388 [7] **ALICE** Collaboration, J. Adam *et al.*, “Multi-strange baryon production in p–Pb
1389 collisions at $\sqrt{s_{NN}} = 5.02$ TeV,” *Phys. Lett.* **B758** (2016) 389–401,
1390 [arXiv:1512.07227 \[nucl-ex\]](https://arxiv.org/abs/1512.07227).
- 1391 [8] **ALICE** Collaboration, B. Abelev *et al.*, “Production of $\Sigma(1385)^{\pm}$ and $\Xi(1530)^0$ in
1392 proton-proton collisions at $\sqrt{s} = 7$ TeV,” *Eur. Phys. J.* **C75** (2015) 1,
1393 [arXiv:1406.3206 \[nucl-ex\]](https://arxiv.org/abs/1406.3206).
- 1394 [9] **ALICE** Collaboration, J. Adam *et al.*, “ D -meson production in p–Pb collisions at
1395 $\sqrt{s_{NN}} = 5.02$ TeV and in pp collisions at $\sqrt{s} = 7$ TeV,” *Phys. Rev. C* **94** (2016)
1396 054908, [arXiv:1605.07569 \[nucl-ex\]](https://arxiv.org/abs/1605.07569).
- 1397 [10] **ALICE** Collaboration, B. Abelev *et al.*, “Inclusive J/ψ production in pp collisions
1398 at $\sqrt{s} = 2.76$ TeV,” *Phys. Lett.* **B718** (2012) 295–306, [arXiv:1203.3641 \[hep-ex\]](https://arxiv.org/abs/1203.3641).
- 1399 [11] **ALICE** Collaboration, J. Adam *et al.*, “Rapidity and transverse-momentum
1400 dependence of the inclusive J/ψ nuclear modification factor in p–Pb collisions at
1401 $\sqrt{s_{NN}} = 5.02$ TeV,” *JHEP* **06** (2015) 55, [arXiv:1503.07179 \[nucl-ex\]](https://arxiv.org/abs/1503.07179).
- 1402 [12] **ALICE** Collaboration, J. Adam *et al.*, “Measurement of pion, kaon and proton
1403 production in proton-proton collisions at $\sqrt{s} = 7$ TeV,” *Eur. Phys. J.* **C75** (2015)
1404 226, [arXiv:1504.00024 \[nucl-ex\]](https://arxiv.org/abs/1504.00024).

- 1405 [13] F. Halzen and A. Martin, “Quarks and Leptons: an introductory course in modern
 1406 particle physics,” *By John Wiley and Sons* (1984) .
- 1407 [14] T. K. Nayak, “Heavy Ions: Results from the Large Hadron Collider,” *Pramana* **79**
 1408 (2012) 719–735.
- 1409 [15] S. Wheaton, J. Cleymans, and M. Hauer, “THERMUS: A Thermal model package
 1410 for ROOT,” *Comput. Phys. Commun.* **180** (2009) 84–106, [arXiv:hep-ph/0407174](#)
 1411 [hep-ph].
- 1412 [16] S. O. T. P. K. W. H.J. Drescher, M. Hladik, “Parton-Based Gribov-Regge Theory,”
 1413 *Phys. Rept.* **350** (2001) 93–289, [hep-ph/0007198](#).
- 1414 [17] T. P. M. B. K. M. K. Werner, Iu. Karpenko, “Event-by-event simulation of the
 1415 three-dimensional hydrodynamic evolution from flux tube initial conditions in
 1416 ultrarelativistic heavy ion collisions,” *Phys. Rev.* **C82** (2010) 044904.
- 1417 [18] I. K. T. P. K. Werner, B. Guiot, “Analyzing radial flow features in p-Pb and p-p
 1418 collisions at several TeV by studying identified-particle production with the event
 1419 generator EPOS3,” *Phys. Rev.* **C89** (2014) 064903.
- 1420 [19] K. Werner., “Analyzing radial flow features in p-Pb and p-p collisions at several TeV
 1421 by studying identified-particle production with the event generator EPOS3,” *Phys.
 1422 Rev. Lett.* **98** (2007) 152301.
- 1423 [20] S. B. et al., “Microscopic Models for Ultrarelativistic Heavy Ion Collisions,” *Prog.
 1424 Part. Nucl. Phys.* **41** (1998) 255.
- 1425 [21] M. B. et al., “Relativistic Hadron-Hadron Collisions in the Ultra-Relativistic
 1426 Quantum Molecular Dynamics Model,” *J. Phys.* **G25** (1999) 1859–1896.
- 1427 [22] M. Gell-Mann and Y. Ne’eman, “The Eightfold Way,” *By W.A. Benjamin* (1964) .
- 1428 [23] J. Rafelski and B. Mller, “Strangeness Production in the Quark-Gluon Plasma,”
 1429 *Phys. Rev. Lett* **48** (1982) 1066–1069.
- 1430 [24] **ALICE** Collaboration, B. Abelev *et al.*, “Multi-strange baryon production at
 1431 mid-rapidity in Pb–Pb collisions at $\sqrt{s_{\text{NN}}} = 2.76$ TeV,” *Phys. Lett.* **B728** (2014)
 1432 216–227, [arXiv:1307.5543](#) [nucl-ex].
- 1433 [25] P. Braun-Munziger, “Chemical equilibration and the Hadron-QGP phase
 1434 transition.”
- 1435 [26] **ALICE** Collaboration, B. Abelev *et al.*, “Performance of the ALICE Experiment at
 1436 the CERN LHC,” *Int. J. Mod. Phys.* **A29** (2014) 1430044, [arXiv:1402.4476](#)
 1437 [nucl-ex].

- 1438 [27] L. Evans and P. Bryant, “LHC Machine,” *JINST* **3** (2008) S08001.
- 1439 [28] “ALICE Technical Proposal,” *In CERN-LHCC-95-71* (1995) .
- 1440 [29] “ATLAS Technical Proposal,” *In CERN-LHCC-94-43* (1994) .
- 1441 [30] “CMS Technical Proposal,” *In CERN-LHCC-94-38* (1994) .
- 1442 [31] “LHCb Technical Proposal,” *In CERN-LHCC-98-004* (1998) .
- 1443 [32] “Technical Proposal for CERN LHCf Experiment,” *In CERN-LHCC-05-032* (2005) .
- 1444 [33] “Total Cross Section, Elastic Scattering and Diffraction Dissociation at the LHC,”
 1445 *In CERN-LHCC-99-007* (1999) .
- 1446 [34] **ALICE** Collaboration, K. Aamodt *et al.*, “The ALICE experiment at the CERN
 1447 LHC,” *JINST* **3** (2008) S08002.
- 1448 [35] **ALICE** Collaboration, L. B. et al, “Definition of the ALICE coordinate system and
 1449 basic rules for sub-detector components numbering,” *In Internal Note
 1450 ALICE-INT-2003-038* (2003) .
- 1451 [36] **ALICE** Collaboration, J. e. a. Alme, “The ALICE TPC, a large 3-dimensional
 1452 tracking device with fast readout for ultra-high multiplicity events,” *In Nuclear
 1453 Instruments and Method in Physics Research* **A622** (2010) 316–367.
- 1454 [37] “Technical Design Report on Forward Detectors: FMD, T0 and VZERO,” *In
 1455 CERN-LHCC-2004-025* (2004) .
- 1456 [38] R. Glauber, “Lectures in Theoretical Physics,” *By Interscience Publishers.* **1** (1959)
 1457 315.
- 1458 [39] A. S. K.C. Chung, C.S. Whang and G. Pech, “Transverse and forward energy
 1459 distributions in untra-relativistic heavy-ion collisions by an absorption model,”
 1460 *Physics Review* **C57** (1998) 847–856.
- 1461 [40] **ALICE** Collaboration, J. Adam *et al.*, “Centrality dependence of particle
 1462 production in p–Pb collisions at $\sqrt{s_{\text{NN}}}= 5.02 \text{ TeV}$,” *Phys. Rev.* **C91** (2015) 064905,
 1463 [arXiv:1412.6828 \[nucl-ex\]](https://arxiv.org/abs/1412.6828).
- 1464 [41] **ALICE** Collaboration, B. Abelev *et al.*, “Centrality determination of Pb–Pb
 1465 collisions at $\sqrt{s_{\text{NN}}}= 2.76 \text{ TeV}$ with ALICE,” *Phys. Rev.* **C88** (2013) ,
 1466 [arXiv:1303.0737 \[nucl-ex\]](https://arxiv.org/abs/1303.0737).
- 1467 [42] “ALICE Technical Design Report of the Trigger, Data Acquisition, High-Level
 1468 Trigger, Control system,” *In CERN-LHCC-2003-062.* (2003) .

- 1469 [43] “The Grid - Blueprint for a New Computing Infrastructure,” *By Morgan Kaufmann*
 1470 *Publishers.* (1999) .
- 1471 [44] e. a. Bagnasco. S, “AliEn: ALICE Environment on the GRID,” *In Jounal of Physics: Conference Series* **119** (2008) n.062012.
- 1473 [45] R. Brun and F. Rademakers, “ROOT - An object oriented data analysis framework,”
 1474 *In Nuclear Instrument and Methods in Physics Research Section A* **389** (1997)
 1475 81–86.
- 1476 [46] **ALICE** Collaboration, B. Abelev *et al.*, “Pseudorapidity Density of Charged
 1477 Particles in p–Pb Collisions at $\sqrt{s_{\text{NN}}}= 5.02$ TeV,” *Phys. Rev. Lett.* **110** (2013)
 1478 032301, [arXiv:1210.3615 \[nucl-ex\]](#).
- 1479 [47] **ALICE** Collaboration, K. Aamodt *et al.*, “Strange particle production in
 1480 proton-proton collisions at $\sqrt{s}= 0.9$ TeV with ALICE at the LHC,” *Eur. Phys. J.*
 1481 **C71** (2011) 1594, [arXiv:1012.3257 \[nucl-ex\]](#).
- 1482 [48] S. Roesler, R. Engel, , and J. Ranft, “The Monte Carlo Event Generator
 1483 DPMJET-III, Advanced Monte Carlo for Radiation Physics, Particle Transport
 1484 Simulation and Applications,” *Conference Proceedings, MC2000, Lisbon, Portugal,*
 1485 *October 23-26* (2000) 1033–1038, [hep-ph/0012252](#).
- 1486 [49] R. Brun, F. Carminati, and S. Giani, “GEANT detector description and simulation
 1487 tool,” *CERN-W5013* (1994) .
- 1488 [50] R. Barlow, “Systematic Errors: Facts and Fictions,” *Presented at Advanced
 1489 Statistical Techniques in HEP, Durham, March 2002* (2002) 333p,
 1490 [hep-ex/0207026v1](#).
- 1491 [51] **ALICE** Collaboration, B. Abelev *et al.*, “Centrality dependence of π , K and p
 1492 production in Pb–Pb collisions at $\sqrt{s_{\text{NN}}}= 2.76$ TeV,” *Phys. Rev.* **C88** (2013) ,
 1493 [arXiv:1301.4361 \[nucl-ex\]](#).
- 1494 [52] **STAR** Collaboration, B. I. Abelev *et al.*, “Hadronic resonance production in d–Au
 1495 collisions at $\sqrt{s_{\text{NN}}}= 200$ GeV measured at the BNL Relativistic Heavy-Ion Collider,”
 1496 *Phys. Rev.* **C78** (2008) 044906, [arXiv:0801.0450 \[nucl-ex\]](#).
- 1497 [53] A. Velásquez, “Mean p_{T} scaling with m/n_q at the LHC: Absence of (hydro) flow in
 1498 small systems?,” *Nucl. Phys.* **A943** (2015) 9–17, [arXiv:1506.00584 \[hep-ph\]](#).
- 1499 [54] **ALICE** Collaboration, B. Abelev *et al.*, “Multi-strange baryon production in pp
 1500 collisions at $\sqrt{s}= 7$ TeV with ALICE,” *Phys. Lett.* **B712** (2012) 309,
 1501 [arXiv:1204.0282 \[nucl-ex\]](#).

- 1502 [55] T. Sjöstrand, S. Mrenna, and P. Skands, “A brief introduction to PYTHIA 8.1,”
1503 *Comput. Phys. Comm.* **178** (2008) 852–867, arXiv:0710.3820 [hep-ph].

1504 **Acknowledgements**